

ADDITIVE MANUFACTURING AND IN SITU MECHANICAL AND MATERIAL  
CHARACTERIZATION OF METALLIC STRUCTURES AT MICRO/NANOSCALE

by

Seyed Soheil Daryadel



APPROVED BY SUPERVISORY COMMITTEE:

---

Dr. Majid Minary, Chair

---

Dr. Dong Qian

---

Dr. Rodrigo Bernal Montoya

---

Dr. Hongbing Lu

---

Dr. Moon J. Kim

Copyright © 2018

Syed Soheil Daryadel

All Rights Reserved

*To my mom and dad*

ADDITIVE MANUFACTURING AND IN SITU MECHANICAL AND MATERIAL  
CHARACTERIZATION OF METALLIC STRUCTURES AT MICRO/NANOSCALE

by

SEYED SOHEIL DARYADEL, BS, MS

DISSERTATION

Presented to the Faculty of  
The University of Texas at Dallas  
in Partial Fulfillment  
of the Requirements  
for the Degree of

DOCTOR OF PHILOSOPHY IN  
MECHANICAL ENGINEERING

THE UNIVERSITY OF TEXAS AT DALLAS

DECEMBER 2018

## ACKNOWLEDGMENTS

I would like to thank my academic advisor, Dr. Majid Minary, for his endless support, invaluable guidance, and for always giving me the vision about the big picture. Dr. Minary's advice, passion in exploring new fields, and insightful ideas were the powerful driving force for my research, and his hands-on advising style nurtured my interest in the field. I learned a lot from Majid and owe him for giving me this opportunity.

I was very fortunate to have Dr. Dong Qian, Dr. Hongbing Lu, Dr. Rodrigo Bernal, and Dr. Moon Kim on my graduate committee. Their valuable suggestions and advice strengthened this work significantly. In particular, I am indebted to Dr. Bernal for his encouragement, guidance, and willingness to discuss details of my work throughout the last years. Rodrigo was always open to me when I needed help both academically and personally. I would like to thank Dr. Qian for his invaluable constructive comments especially at the start of our project in our weekly meetings. Dr. Lu and Dr. Kim's comments at my proposal exam encouraged me to explore deeper into the mechanics of 3D printed structure and the effect of thermal annealing presented in the dissertation. In addition, I would like to thank individuals who supported my graduate studies at UT Dallas. My colleagues, Mahmoud, Ali, Salvador, Kevin, Zhe, Emran, and Chao were very helpful in my research. Mahmoud started me on many tools in the lab and helped me a lot with the printer setup. Salvador assisted for software programming, and Ali aided in the 3D printing experiments. I would like to thank my friends from other groups, Sadeq, Qingxiao, Luhua, for their invaluable assistance. I would also like to express my gratitude to Dr. Julia Bykova and Dr. Juan Pablo Oviedo for their assistance with TEM, Dr. Winston Layne, Dr. Roger Robbins, and the cleanroom staff at NSERL for the training of different tools, Ms. Cathie Ranta, Ms. Ashley Bradberry, and the staff

in the ME department for their constant help, and the ME machine shop staff. I would also like to acknowledge financial support during my graduate studies from the National Science Foundation CMMI and US Office of Naval Research.

My graduate studies would not have been possible without the endless support from my family. My parents put up with my absence for more than five years and I wish I could have been there when they needed me in every moment. I believe there are not enough words to thank them and I will always be indebted to them. My mother's endless love has always been a sustaining force for our family. I wish that her integrity, caring, and compassion are reflected in my personality. My father has taught me so much. He gave me the life that every child deserves and encouraged me throughout my lifetime. He worked so hard to send me to US for graduate studies, which means a world to me. Speaking of character building, I was fortunate to have the best brother that I could have asked for, Saman. He is a natural born leader who taught me unconditional love and support for family at so many occasions. Also, I am thankful to my beloved sister, Sahar, for her constant care and support. Her voice on the phone always motivated me during these years. Going away and being apart from family has made me realize that they are the most important people in my life, and I love them more than anything. I would like to thank them and I promise that I will work hard to make them proud.

Finally, I would like to thank the group of smart, fun and supportive friends that helped me get through the school life. I believe their friendship had so many positive touches on my life. There are no words that can justice how grateful I am to everything they have done for me. My friends, Roozbeh and Kaveh are among the best friends from far away that have always been there for me in every difficult moment. I would like to thank all my friends in US that gave me this feeling that

away from home, there is someone that cares about me. From Mississippi to Dallas, Fakhri, Zia, Sepideh, Pooya, Farbod, Farzin, Amir, Parichehr, Saloomeh, and so many other friends not only made me feel like home but supported me continuously. Additionally, I would like to thank friends and families: Borna, Nariman, Nastaran, Mohammad, Soroush, Ali, Shayan, Sepideh, Mohammad, Masoud, Anahita, Mahmoud, Mohammad, Amin, Saeed, Sina, Pooria, Nima, Mehran, Amer, Hooman, Reza, Mina, Morvarid, Sina, Sanaz, Tohid and many good friends that I might have forgotten to name will remain part of my life after graduation. My PhD studies at the UT Dallas have been a wonderful journey. I hope to be able to use everything that I learned toward creating a better future in a peaceful world.

October 2018

ADDITIVE MANUFACTURING AND IN SITU MECHANICAL AND MATERIAL  
CHARACTERIZATION OF METALLIC STRUCTURES AT MICRO/NANOSCALE

Seyed Soheil Daryadel, PhD  
The University of Texas at Dallas, 2018

Supervising Professor: Dr. Majid Minary

The progress in microscale additive manufacturing ( $\mu$ -AM) of metals requires engineering of the microstructure for various functional applications. *In situ* control over the microstructure during three-dimensional (3D) printing is critical to achieve metallic nanostructures with desired properties and eliminate the need for post-processing. In this dissertation, an ambient environment localized pulsed electrodeposition (L-PED) process for direct printing of 3D free-standing and layer-by-layer nanotwinned (nt) metals is introduced. 3D nt-Cu structures were additively manufactured using pulsed electrodeposition at the tip of an electrolyte containing nozzle. For the first time, the control of the microstructure of metals during 3D-printing is reported. In particular, It is shown that through variation of electrochemical process parameters the density and the orientation of the coherent twin boundaries (CTBs), as well as the grain size can be controlled. Nt-metals offer superior mechanical (high ductility and strength) and electrical properties (low electromigration) compared to their nanocrystalline (nc) counterparts. While these properties are advantageous for applications in nanoscale devices, the fabrication of nt-metals has been limited to 2D films or template-based 1D geometries.

The focused ion beam (FIB) and transmission electron microscopy (TEM) analysis showed that the printed metal was fully dense, mostly devoid of impurities and microstructural defects, and confirmed the formation of CTBs. Mechanical properties of the 3D printed nt-Cu were characterized by *in situ* SEM micro-compression experiments. The 3D printed nt-Cu exhibited average flow stress of 960 MPa, which is remarkable for a 3D printed material. The microstructure and mechanical properties of the nt-Cu was compared to nc-Cu printed using the same process under direct current (DC) voltage. The results show that such control over microstructure directly correlates with the mechanical properties of the printed metal. L-PED is introduced as an approach to enable direct deposition of nano-pillars and micro-pillars of metals and alloys. When combined with *in situ* nanomechanics instrumentation, this approach may enable high-throughput investigation of the process–microstructure–property relationship, in particular for nano-crystalline and nano-twinned metals.

The application for 3D printed electronics will be greatly extended when they can be used in extreme environments and especially at elevated temperatures. Therefore, the thermal stability and reliability of the additively manufactured nt-Cu interconnects is investigated. The results show clear correlation between the microstructure and the thermal stability of the printed metal. The microstructures with columnar shaped grains and high density of low-energy CTBs exhibited better thermal stability compared to the ones with high-angle random-oriented grain boundaries. Despite the evolution of microstructure and growth of the grains, printed materials with high density of TBs exhibited high strength of 522 MPa after annealing for 4 hours at 300 °C. Additionally, LED is extended to a larger scale process for patterning of high quality metallic patterns on flexible and nonconductive substrates. The printed metallic patterns are solid with no

porosity and impurities, and exhibit high electrical conductivity. Overall, the results indicate the feasibility of using LED 3D-printed high conductivity nt-metal features in a wide range of applications, particularly for the electronics and the next generation integrated circuits.

## TABLE OF CONTENTS

ACKNOWLEDGMENTS .....	v
ABSTRACT.....	viii
LIST OF FIGURES .....	xiii
LIST OF TABLES .....	xix
CHAPTER 1 INTRODUCTION.....	1
CHAPTER 2 LOCALIZED ELECTRODEPOSITION .....	7
2.1 FUNDAMENTALS AND PROCESS PARAMETERS.....	7
2.2 3-D PRINTER SETUP.....	15
CHAPTER 3 LOCALIZED PULSED ELECTRODEPOSITON PROCESS FOR 3D PRINTING OF NANOTWINNED METALLIC NANOSTRUCTURES.....	20
3.1 INTRODUCTION .....	20
3.2 MATERIALS AND METHODS .....	23
3.3 RESULTS AND DISCUSSION .....	26
3.4 CONCLUSION.....	42
CHAPTER 4 TOWARD CONTROL OF MICROSTRUCTURE IN MICROSCALE ADDITIVE MANUFACTURING OF COPPER USING LOCALIZED ELECTRODEPOSITION .....	44
4.1 INTRODUCTION .....	44
4.2 MATERIALS AND METHODS .....	49
4.3 RESULTS AND DISCUSSION .....	51
4.4 CONCLUSIONS.....	64
CHAPTER 5 THERMAL STABILITY OF NANOTWINNED COPPER IN INTERCONNECTS ADDITIVELY MANUFACTURED BY THE LOCALIZED PULSED ELECTRODEPOSITION .....	65
5.1 INTRODUCTION .....	65
5.2 MATERIALS AND METHODS .....	68
5.3 RESULTS AND DISCUSSION .....	70
5.4 CONCLUSION.....	79
CHAPTER 6 A MICROSCALE ADDITIVE MANUFACTURING APPROACH FOR IN SITU NANOMECHANICS .....	81
6.1 INTRODUCTION .....	81

6.2 MATERIALS AND METHODS .....	83
6.3 PROCESS DESCRIPTION .....	84
6.4 RESULTS AND DISCUSSION .....	90
6.5 CONCLUSIONS.....	97
CHAPTER 7 LARGE SCALE METAL 3D PRINTING USING LOCALIZED ELECTRODEPOSITION .....	99
7.1 INTRODUCTION .....	99
7.2 MATERIAL AND METHODS .....	100
7.3 RESULTS AND DISCUSSION .....	102
7.4 CONCLUSION.....	108
CHAPTER 8 CONCLUSIONS AND FUTURE WORK.....	110
8.1 OUTLOOK .....	111
REFERENCES .....	116
BIOGRAPHICAL SKETCH .....	122
CURRICULUM VITAE	

## LIST OF FIGURES

- Figure 1.1. Summary of small scale metal AM techniques. The methods are categorized into two main groups: the techniques based on transfer of pre-synthesized metals, and the ones that synthesize metals at the location of interest (in situ). (Reprinted from Ref <sup>2</sup> with the permission of John Wiley and Sons). .....2
- Figure 2.1. (Left) The schematic of LED printing setup and (Right) the close-up view of the nozzle and the electrolyte meniscus during deposition. The metal ions are deposited on the substrate by application of electrical potential using the potentiostat. The high precision 3-axis positioners are used for the positioning of the pipette and printing process. ....8
- Figure 2.2. (Left) Side optical view and (right) the geometry details of the meniscus (Reprinted from Ref<sup>30</sup>, with the permission of AIP Publishing).....10
- Figure 2.3. Dependence of wire diameter on pipette withdrawal speed compared to the FE (finite element) model (Reprinted from Ref <sup>31</sup> with the permission of AIP Publishing) .....13
- Figure 2.4. (Left) The schematic I-t (current-time) response for the galvanostatic mode, where the current between the electrodes is controlled, and the potential is a dependent variable as a function of time. (Right) Typical electric potential acquired during deposition of a micro-pillar in the galvanostatic mode while the RH was increasing. The system maintains the desired current during printing by varying the applied potential, and compensates for the changes of the ionic flux due to changes of RH. ....15
- Figure 2.5. Cyclic voltammetry obtained in situ at a scan rate of 100 mV/s. The peaks at ~ -0.25 V indicate the reduction of Cu<sup>2+</sup> to Cu. The deposition potential during 3D printing was set after the cathodic reduction potential.....16
- Figure 2.6. The homebuilt 3D printer setup inside a Faraday cage, including a vibration isolation system, motion control stages, a humidity chamber, a visualization system, a potentiostat, and controllers. The inset shows the close-up view of the print-head inside the chamber. ....17
- Figure 2.7. The SEM images of a fabricated glass nozzle with a diameter of 840 nm using pipette puller. ....18
- Figure 3.1. Sample preparation for microstructural characterization. (A) The SEM image of the wire. (B) The wire was embedded in Pt deposition, and (C) the cross-section was milled in order to enable FIB imaging. (D) - (F) The lift-out and FIB thinning procedure for TEM imaging. The wire was coated in a Pt protective layer, and transferred to a Cu TEM grid. The specimen was milled from both sides to reach 100 nm thickness for TEM imaging. 25

Figure 3.2. (A) - (C) In situ micro-compression experiment using a 10 $\mu\text{m}$ diameter flat punch tip. (D) A typical displacement history during micro-compression test. The rate of displacement was 2 nm/s. ....	26
Figure 3.3. The schematic close-up view of the nozzle and the electrolyte meniscus during L-PED 3D electrodeposition. Metal ions are reduced at the growth front under an applied pulsed electric potential between the anode and cathode. Through application of a pulsed voltage, nanotwinned metals can be printed in arbitrary 3D geometries. ....	27
Figure 3.4. 3D-printed Cu wires using (A) pulsed electrodeposition (PED), and (B) direct current electrodeposition (DC-ED). The insets are 3D schematics of the printed metal. (C) 3D-printed wires using the L-PED process with various angles with respect to the substrate, from $\sim 90^\circ$ to $\sim 40^\circ$ . For better presentation, the SEM images of individual angled wires are combined. (D) “UTD”-shaped array of 31 copper pillars, printed by the L-PED process. The diameter of the wires are in the range of 500 nm to 1000 nm depending on the nozzles diameter.....	29
Figure 3.5. SEM images of the layer-by-layer printed structure using the L-PED process. (A) 2-layer 10 $\mu\text{m}$ by 10 $\mu\text{m}$ hollow square, (B) 5 $\mu\text{m}$ 10-layer wall and (C) zoom-in view of the red box, printed with a micropipette of $\sim 800$ nm diameter. (D) 7-layer 30 $\mu\text{m}$ line deposition followed by a 3 $\mu\text{m}$ pillar deposition, and (E) 10-layer 30 $\mu\text{m}$ by 8 $\mu\text{m}$ cube deposition using a $\sim 5$ $\mu\text{m}$ diameter pipette. ....	31
Figure 3.6. EDS (A) map and (B) line analysis acquired from the PED and DC-ED deposited wires. (C) The spectra from the selected area (red squares) show pure Cu deposition free of impurities. ....	32
Figure 3.7. (Left) FIB ion channeling contrast image of a micro-pillar deposited using PED and DC-ED techniques. The first 4 $\mu\text{m}$ height of the pillar was deposited using pulsed voltage and the next 4 $\mu\text{m}$ was continued using DC voltage with an average current density of 0.011 A/cm <sup>2</sup> . (Right) Magnified view of the approximate boundary between the two methods (Reprinted from Ref <sup>54</sup> , with the permission of John Wiley and Sons).....	33
Figure 3.8. Microstructure of wires printed using (A)-(D) PED and (E)-(H) DC-ED. (A) The cross-section FIB ion channeling contrast image, and (B) TEM dark-field image of the wire printed by PED. (C) Zoomed-in image of the area enclosed in box in B shows a typical grain with (D) the corresponding diffraction pattern, which reveals the nanocrystalline nanotwinned (nc-nt) structure with columnar shaped grains. (E) The cross-section FIB ion channeling contrast image, and (F) and (G) TEM bright field images of the wire printed by DC-ED. (H) The diffraction pattern confirms nanocrystalline (nc) structure. ....	35
Figure 3.9. HRTEM image of typical coherent TB in the PED wire. The TBs are shown by the dashed line. Insets are FFT patterns of (i, ii) two mirrored sides of the TB, and (iii) the TB, respectively. ....	36

- Figure 3.10. Lattice structure characterization using high resolution TEM image of a twin boundary. (i) Total d-spacing of 20 fringes along the specified region, which indicates d-spacing of 2.09 Å. (ii) Total d-spacing of 19 fringes along the specified region, which indicates d-spacing of 2.11 Å. The measured d-spacings at two regions show (111) planes on both sides of the twin boundary. ....37
- Figure 3.11. (Left) SEM image of zoomed-in view of the layer-by-layer deposited structure and (right) The FIB image of the cross-section showing that each layer is deposited on the previous layer, with no noticeable interlayer. ....38
- Figure 3.12. Micro-compression stress and strain responses of 3D-printed Cu micro-pillars by (A) PED with nc-nt microstructure, and (B) DC-ED with nc microstructure. The inset in A is an SEM image of the micro-compression experiment. (C) Comparison of flow stress of each microstructure at 10% strain. (D) Strength of the 3D-printed micro-pillars compared with similar nanowires fabricated with different methods (green = ultrafine grain, black = single crystal, red = nanocrystalline, blue = nanocrystalline nanotwinned, and orange = single crystal nanotwinned). Note that the color code is for each specific microstructure. The shapes in the legend of the figure refer to the specific reference. ....40
- Figure 3.13. (A) In situ SEM nanoindentation on the L-PED printed layer-by-layer nt-Cu sample. (B) SEM image of an indentation footprint. (C) An AFM topography image of one of the indentation footprints. (D) Line-scan obtained from the indentation site, which shows pile-up in the indentation (Reprinted from <sup>54</sup>, with the permission of John Wiley and Sons).42
- Figure 3.14. (A) Load-indentation depth plot obtained from nanoindentation on the nanotwinned copper sample. (B) and (C) Graph show elastic modulus and hardness of the printed Cu, respectively (Reprinted from <sup>54</sup>,with the permission of John Wiley and Sons).....43
- Figure 4.1. (A) The schematic view of L-PED 3D printing process. Side-by-side comparison of (B) the L-PED printing process and (C) the bulk electrodeposition. (D) Pulsed current electrodeposition (PED) with an arbitrary duty cycle. SEM images of (E) an array of 3D-printed  $\mu$ -pillars for micro-compression experiment (printing time for each pillar  $\sim$ 12 min), (F) a 40-layer structure printed by layer-by-layer L-PED (printing time  $\sim$ 150 min), (G) a spiral pattern (printing time =  $\sim$ 15 min), and (H) a close-up view of a  $\mu$ -pillar for micro-compression and microstructure characterization.....48
- Figure 4.2. (A) The EDS spectra acquired from a printed  $\mu$ -pillar. No significant presence of impurities was observed in EDS data. (B) The experimental deposition rate for the printed  $\mu$ -pillars by the L-PED process vs. the average current density. The solid line is the deposition rate calculated from the Faradays law. The current efficiency of the L-PED process was calculated to be  $90 \pm 5\%$ . (C)-(H) The effect of the average current density (and deposition rate) on the microstructure of 3D-printed nanotwinned Cu  $\mu$ -pillars. The cross-section FIB ion channeling contrast image of  $\mu$ -pillars printed at different deposition rates reveal that increasing the deposition rate increases the density and alignment of the twin boundaries (TBs).....53

- Figure 4.3. (A) and (B) The effect of the peak current density on microstructure of 3D-printed nanotwinned Cu: The cross-section FIB ion channeling contrast image show that increasing the peak current density increased the twin density and decreased the grain size. (C) and (D) increasing the ON-time results in higher density of twin boundaries. (E) and (F) increasing the OFF-time decreases the twin density and increases the grain size.....56
- Figure 4.4. The Comparison of the obtained deposition rates of printed pillars by DC-ED process with the analytical growth rate calculated from the Faradays law. The obtained average current efficiency of DC-ED was calculated to be  $95 \pm 4 \%$ .....58
- Figure 4.5. (A)-(C) The effect of the current density and deposition rate on the microstructure of Cu printed by DC-ED process. The cross-section FIB ion channeling contrast images of selected pillars show that increasing deposition current density causes grain refinement. The grain sizes of the pillars are (A)  $307 \pm 47$  nm (B)  $174 \pm 52$  nm (C)  $121 \pm 18$  nm. (D) Average grain size vs. current density for the metal printed using the DC-ED process....59
- Figure 4.6. (A) In situ SEM micro-compression experiment on  $\mu$ -pillars printed using three different deposition rates (and average current densities). (B) SEM image of a compressed  $\mu$ -pillar. (C) Stress vs. strain responses of the  $\mu$ -pillars printed in three different deposition rates. (D) Comparison of the average flow stress of each microstructure. ....62
- Figure 4.7. Illustration of (A) process – microstructure and (B) microstructure – property relations in microscale 3D printing of Cu by localized pulsed electrodeposition (L-PED) process. ....63
- Figure 5.1. (A) Schematic view of the L-PED 3D printer setup. (B) A close-up view of 3D printed micro-pillar. (C) An array of printed micro-pillars interconnects. ....71
- Figure 5.2. SEM surface images of nt-Cu micro-pillars with high density of twins (A) as-deposited and after 4 hours annealing at (B) 150 °C (C) 300 °C (D) 450 °C and nt-Cu micropillars with low density of twins (E) as-deposited and after 4 hours annealing at (F) 150 °C (G) 300 °C (H) 450 °C. All scale bar are 3  $\mu$ m. ....73
- Figure 5.3. Cross-sectional FIB ion contrast images reveal the microstructure of nt-Cu micro-pillars with high density of twins (A) as-deposited and after 4-hour annealing at (B) 150 °C (C) 300 °C (D) 450 °C; and nt-Cu micropillars with low density of twins (E) as-deposited and after 4-hour annealing at (F) 150 °C (G) 300 °C (H) 450 °C. Scale bars are 2  $\mu$ m. ....77
- Figure 5.4. (A) In situ micro-compression experiments on an array of nt-Cu micro-pillars printed using the L-PED process. (B) The close-up SEM view of micro-pillar at beginning of the test. (C) SEM image of compressed micro-pillar. (D) True stress-Strain responses of the micro-pillars printed in two different deposition rates of 23 nm/s and 18 nm/s and annealed for 4 hours at 300 °C. (E) Comparison of the average flow stress of each micro-pillar at 5% strain. ....79

- Figure 6.1. Comparison of the L-PED AM process with the FIB milling and template-based electroplating approaches for fabrication of micro-scale pillars. AM enables fabrication of specimens in a single step at low-cost in room environment.....84
- Figure 6.2. (A) Schematic view of the L-PED 3D-printing setup. (B) The printing process of a micro-pillar using the L-PED process includes approach of the nozzle-tip to the substrate, formation of the meniscus (liquid bridge) between the tip and the conductive substrate as the confined electrodeposition bath, application of an electric potential between two electrodes and deposition of the metal ions at the growth front followed by controlled withdrawal motion of the nozzle. (C)-(D) Process parameters of the L-PED process can be adjusted, which enables control over the microstructure of the printed structures: (B) Pulsed electrodeposition (PED) results in nanocrystalline nanotwinned microstructure, while (C) DC electrodeposition (DC-ED) produces nanocrystalline microstructure. ....86
- Figure 6.3. (A) Dependence of the diameter of the printed pillar ( $D_P$ ) on the diameter of the nozzle tip ( $D_N$ ). Micro-pillars with diameter in the range of 0.5- to 0.9-time of the diameter of the nozzle can be printed. (B) – (C) Cu micro-pillars printed using the L-PED process with different diameters of 0.73  $\mu\text{m}$  and 5.25  $\mu\text{m}$  by different nozzles.....87
- Figure 6.4. (A) An SEM image of an array of directly printed Cu micro-pillars using the L-PED process with a diameter distribution of  $4.6 \pm 0.08 \mu\text{m}$ . The micro-pillars were printed with  $T_{on}$  of 20 ms,  $T_{off}$  of 2 s and the peak current density of  $3.74 \pm 0.17 \text{ A/cm}^2$  at a deposition rate of 12 nm/s. The printing of each micro-pillar took about ~16 minutes. (B) The micro-pillar was sectioned using FIB to reveal its internal structure. The deposited material is fully dense with no apparent porosity. The ion-channeling contrast image reveals the microstructure of the printed metal including the grain size and shape and existence of the twin boundaries. One of the columnar-shaped grains is delineated by dashed line. (C) Dark-field TEM image of the pillar printed by the L-PED process shows a typical grain with the corresponding diffraction pattern (inset), which reveals the nanocrystalline nanotwinned (nc-nt) structure. (D) HRTEM (high resolution TEM) image of a typical twin boundary shown by the dashed line. (E) Histogram of twin thickness distribution in the grains with peak at ~17 nm.....91
- Figure 6.5. (A)-(B) Photographs of the nanoindenter and the substrate containing the 3D printed micro-pillars *in situ* SEM. (C) Micro-compression experiment *in situ* SEM on individual micro-pillars from an array of 3D-printed pillars using a flat punch tip. (D) A typical stress-strain response of nc-nt Cu (nanocrystalline-nanotwinned copper) micro-pillar printed using the L-PED process. (E) The average flow stress of the pillars at strain of 5%. (F)-(G) SEM images of the micro-pillar pre- and post-compression, respectively. ....93
- Figure 6.6. (A) Comparison of the strength of nanotwinned copper L-PED micro-pillars (red symbols) and other reported nanotwinned materials in the form of electrodeposited or sputtered bulk solids and films, or nanopillars fabricated using FIB milling or template patterning<sup>39, 40, 42, 55, 60, 65, 114-117</sup>. (B) Comparison of compression strength in L-PED nc-nt Cu micro-pillars and similar pillars fabricated by the template-based electrodeposition and

FIB milling with near equivalent nanocrystalline microstructure and twin orientations. <sup>55, 60</sup> .....	95
Figure 6.7. (A) The in situ SEM setup for characterization of electrical properties of the 3D-printed micro-pillars. (B)-(C) SEM images of the procedure for measurement of the electrical resistivity of a pillar with diameter of ~700 nm. (D) A typical I-V response on the top and bottom of a single 3D-printed Cu micro-pillar. (E) The average calculated resistivity of the Cu micro-pillar.....	97
Figure 7.1. (A) The schematic of the LED setup for large scale printing. (B) Large scale LED metal 3D printer setup.....	101
Figure 7.2. Images of several Cu patterns printed on (A) and (B) gold-coated glass slides, (C) (D) conductive PLA, and (E) and (F) PET film using large scale LED printing process. ....	103
Figure 7.3. (A) A 200-layer copper line printed on a gold-coated glass slide using the LED process. (B) Profile of the printed structure (red line) obtained using the profilometer, and (C) the zoomed-in profile.....	105
Figure 7.4. (A)–(C) SEM images of the printed Cu pattern and different magnifications. (D) Energy-dispersive X-ray spectroscopy (EDS) analysis of the deposited Cu. The spectra shows pure Cu deposition free of impurities. ....	106
Figure 7.5. (A) The schematic of the process for printing patterns on a non-conductive substrate including thin layer deposition of the metal of interest as the cathode, printing the pattern, and etching of the thin layer. (B) and (C) The Cu patterns on a non-conductive glass slide after etching the conductive thin layer from the substrate. ....	107
Figure 7.6. (A) Resistivity of the printed Cu line. (B) A RFID tag printed on a glass slide connected to a capacitance and a LED light. (C) By approaching the RFID reader, the LED connected to the printed tag lights up. ....	108
Figure 8.1. Printed pure Ni (A) micro-pillar with diameter of 8.8 $\mu\text{m}$ and (B) 40-layer circular pattern using the LED process. (C) and (D) Printing Cu/Ni alloy lines using different potentials. Higher potential results in increased volume deposition and inclusion of more Ni in the printed structures.....	113
Figure 8.2. SEM images of (A) 3D printed layer-by-layer Alumina-Cu composite and (B) micro-pillar SiC-Cu composite using micro-scale LED process. SEM micrographs of (C) Alumina-Cu composite line (inset) printed by the large scale LED and (D) Alumina-Cu composite electroplated in bulk with agitation. The result show better inclusion of particles at the bulk level with agitation.....	115

## LIST OF TABLES

Table 2.1. Comparison of deposition rate and current for printing wires at two different RH. ...	11
Table 3.1. Process parameters for fabrication of micro-pillars using PED and DC-ED processes. .....	30
Table 3.2. The dimension, deposition rate, and current efficiency of the wires electrodeposited using PED and DC-ED processes. ....	33
Table 4.1. The process parameters of the $\mu$ -pillars printed using the L-PED process.....	54
Table 4.2. The process parameters of the $\mu$ -pillars printed using DC-ED technique. ....	58
Table 5.1. The process parameters of micro-pillars printed using the L-PED process.....	73
Table 7.1. Elemental analysis of the printed Cu obtained from EDS spectra.....	105

# CHAPTER 1

## INTRODUCTION

The trend in downscaling of metallic structures for different applications, such as electronic devices, microelectromechanical systems (MEMS), optics, and sensors leads to development of various micro/nano scale fabrication techniques.<sup>1, 2</sup> For instance, nanowires due to their unique electron transport properties and significant potential applications have recently attracted abundant attention as a noble candidate for incorporation into the three-dimensional (3D) integrated circuits (ICs) and nanoscale electronics. However, the key issue is to make structures with precise shape and positioning.

To date, the most commonly used micro/nano scale fabrication methods are the subtractive manufacturing techniques, such as lithography and FIB-milling. The FIB-fabricated structures have been investigated extensively in recent years.<sup>3</sup> Studies show that besides the time consuming process of sample preparation, the material properties of the manufactured samples may be affected as the FIB introduces damage into the surface of the structure.<sup>4-7</sup> Also the lithography methods are fundamentally two-dimensional (2D) and are not suitable for 3D structures.

Extensive work has been conducted to manufacture free-standing metallic structures in pre-designed templates in order to accurately control the size and shape.<sup>8-10</sup> Although this method is efficient for rapid fabrication of large number of nanowires, it is not able to create complex 3D structures, and requires additional steps for fabrication of the template and its removal at the end of the process.<sup>11</sup>

The design limitations, time consuming and multiple processing steps, and high cost of traditional fabrication process resulted in a broad attention for fabricating complex microstructures

via additive manufacturing (AM). Recently, AM of metallic structures at small scale have been widely explored.<sup>1, 12-25</sup> The summary of these AM methods are presented in Figure 1.1. In this chapter, some of these novel methods are reviewed as following.

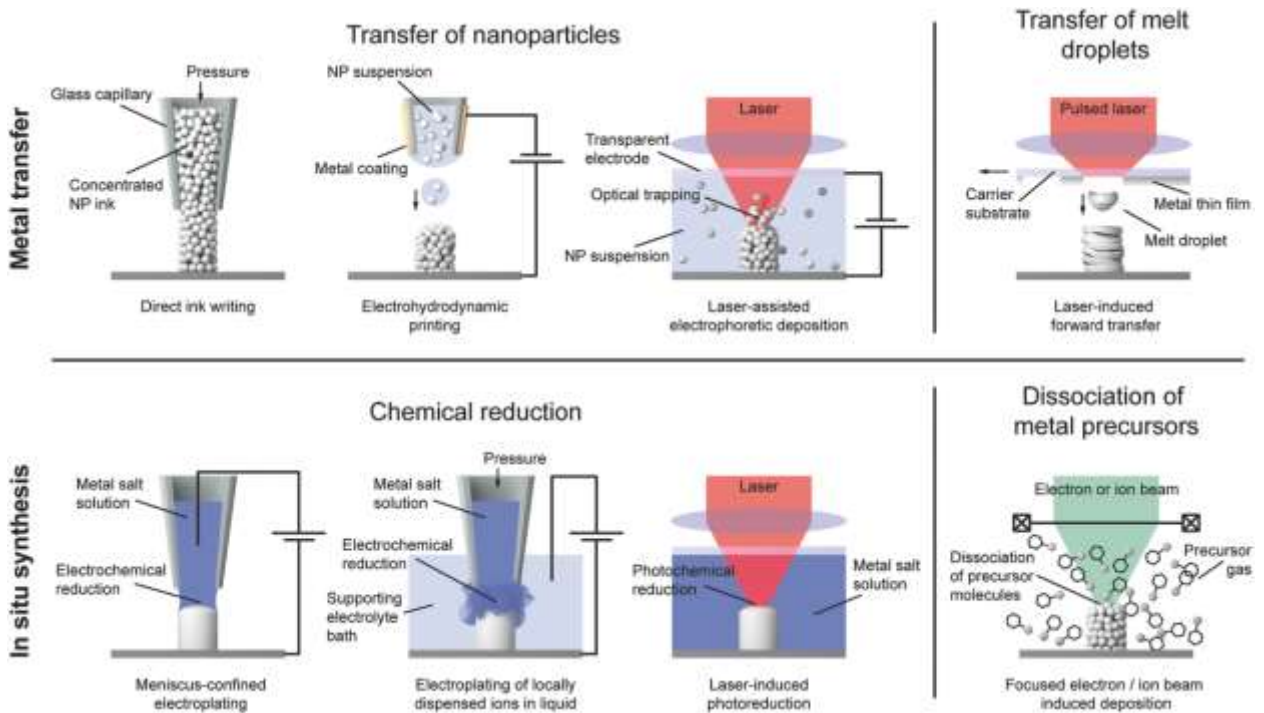


Figure 1.1. Summary of small scale metal AM techniques. The methods are categorized into two main groups: the techniques based on transfer of pre-synthesized metals, and the ones that synthesize metals at the location of interest (in situ). (Reprinted from Ref <sup>2</sup> with the permission of John Wiley and Sons).

The microscale metal AM techniques can be classified into two main groups: metal transfer and in situ synthesis techniques.<sup>2</sup> In the first class, the metallic material is synthesized before the AM process, and subsequently transferred to the location of interest. Direct ink writing (DIW) is a metal transfer technique based on ink-deposition of concentrated metal nanoparticles.<sup>26</sup> In this method, a shear-thinning ink filament with a rigid core and liquid shell is extruded from the nozzle by applying pressure. Interestingly, the liquid shell enables the individual layers to fuse. Combining DIW with in situ laser annealing system enables printing of free-standing structures

on thermally sensitive substrates.<sup>27</sup> The filament thickness depends on the nozzle diameter, pressure, and motion speed. Silver wires with diameters of 600 nm were fabricated with a 1  $\mu\text{m}$  nozzle.<sup>27</sup>

Another metal transfer method is the electrohydrodynamic Printing (e-jet), which is based on electrohydrodynamic extrusion of an ink jet or ink droplets under an applied electric field.<sup>18</sup> After evaporation of the solvent during ejection or on the substrate, the stack of the particles results in 3D structures. There are jetting and dripping ejection modes in this technique, which results from the various field strength, nozzle size, flow rate, and viscosity of the ink. However there are challenges with the solvent evaporation and reproducible printing using jetting mode.<sup>2</sup> Applying a constant electric field, single droplets exit at a given frequency in the dripping mode. The size of the deposit is defined by the droplet diameter. The smallest deposit achieved with this method was 35 nm in width gold nanopillar using a 600 nm nozzle.<sup>19</sup>

Laser-assisted electrophoresis deposition is another metal AM method in the first class.<sup>20</sup> This technique is based on the combination of local electrophoresis deposition and laser trapping. In a liquid cell containing a colloidal solution of metal nanoparticles and two conductive substrates, the nanoparticles is optically trapped and positioned on the location of interest by a laser spot. By application of an electrical voltage between the two-faced substrates, the nanoparticles are deposited onto the surface, and translation of the liquid cell results in fabrication of 3D microstructures. The smallest reported feature size for this method is a 500 nm diameter pillar.<sup>20</sup>

Laser-induced forward transfer (LIFT) is a direct printing technique that relies on metal transfer of melt droplets.<sup>21</sup> A laser pulse is focused on a transparent substrate as a carrier, coated by a thin layer of the print material (donor), and induces local thermal heating to melt the metal

film and evaporate the carrier. This process results in high local pressure at the carrier-metal interface that drives the jetting of the print material into a substrate placed under the carrier. The melt droplets cool and solidify once they reach the substrate. The minimal lateral dimensions of reported structures are several micrometers.<sup>22</sup>

The second class of AM techniques relies on the synthesis of the metal at the location of interest through the process. Focused electron/ion beam induced deposition (FIBID and FEBID) are well-studied techniques in the second class, which are based on the beam-induced dissociation of precursor molecules.<sup>25</sup> The beam interacts with the substrate and the adsorbed precursor molecules, which are supplied in the gas phase, and the precursor dissociates into final deposition. Also the existing volatile fragments are desorbed preferably. The minimum feature size of FEBID/FIBID depends on the beam diameter, and is in the range of tens of nanometers.

Laser-induced photoreduction is also an important AM technique, which utilizes localized photochemical reduction of a photosensitive metal salt solution in order to fabricate 3D structures.<sup>24</sup> Using a pulsed femtosecond laser at the focal spot, the metal ions are deposited upon a two-photon absorption processes, and initiate the nucleation and growth of metallic crystallites in solution or on a nearby substrate, reducing to their zero-valence state.<sup>2</sup>

AM methods based on localized electrochemical deposition have been introduced to obtain conducting polymer and metal micro and nanostructures.<sup>1, 12, 14, 15, 28-31</sup> In this technique a glass capillary with a few micron to sub-micron tip is filled with the electrolyte of a metal of interest. A liquid capillary formed between the tip of the pipette and the conductive substrate completes the electronic-ionic circuit. Upon application an appropriate electric potential, metal ions reduce and get deposited on the substrate. The pipette is steered precisely in 3D using precision nano-

positioners, which results in formation of desired 3D objects from a CAD file. Hirt et al. recently introduced similar method using a hollow AFM (atomic force microscope) cantilevers in solution in order to enhance the geometric freedom of localized electrodeposition method.<sup>15</sup> More detailed description of the method is presented in Chapter 2.

Although different techniques enable 3D printing of true 3D structures of metals, none of these techniques can be applied without expert knowledge, and researchers are still focused on improving and optimization of these processes. Therefore, microscale 3D metallic structures are still predominantly fabricated by traditional methods. However, establishing a micro metal AM technique will enable the fabrication of more complex geometries and material architectures in future. In this dissertation, a novel AM process for metallic structures based on the localized electrochemical deposition is presented. The current chapter is a brief introduction to the existing AM methods and their limitation. Chapter 2 describes the principle and mechanisms behind the LED process, and provides details about the setup. In Chapter 3, I introduce the ambient-environment localized pulsed electrodeposition (L-PED) process for direct printing of three-dimensional (3D) nanotwinned Copper (nt-Cu) nanostructures. The microstructure and mechanical properties of the nc-nt (nanocrystalline-nanotwinned) Cu was studied and compared to nc-Cu printed using the same process under direct current (DC) voltage. Chapter 4 presents in situ control over the microstructure during 3D printing of metals using different process parameters. In chapter 5, thermal stability and mechanical properties of 3D printed micro/nano-scale nt-metallic interconnects at different temperature is investigated. Chapter 6 introduces the LED approach combined with in situ instrumentation as a high-throughput low-cost process for investigation of the process – microstructure – property of metals and alloys. Chapter 7 presents the LED process

as a large scale 3D printing method of metals. The summary and proposed future works are presented in chapter 8.

## CHAPTER 2

### LOCALIZED ELECTRODEPOSITION

#### 2.1 Fundamentals and process parameters

There has been a recent increase of interest in electrodeposition methods, due to the new trending technologies for fabrication of integrated circuits and deposition of multilayer structures.<sup>32</sup> Likewise, 3D printing techniques based on localized electrochemical deposition have been introduced to fabricate metallic structures at micro and nanoscales.<sup>1, 12, 14, 15, 28-31</sup> In this technique, the area of deposition can be limited by the size of the water meniscus formed between the nozzle tip and the substrate. This liquid bridge can be used as a localized electrochemical cell for electrodeposition of metals.

The localized electrodeposition (LED) process is schematically shown in Figure 2.1. A nozzle with a few microns to sub-micron tip, filled with the electrolyte of the metal of interest, functions as the printing tool bit. The electrolyte meniscus (liquid bridge) at the nozzle tip, which is formed when the nozzle approaches to the substrate, functions as a confined electrodeposition bath. A two-electrode configuration was employed for the LED process, consisting of a working electrode (the substrate surface area enclosed by the meniscus between the micropipette and the substrate) and a counter electrode (a 250  $\mu\text{m}$  diameter metal wire that is several cm in length and is inserted within the micropipette).

The metal ions are reduced at the growth front within the meniscus area on the cathode by application of an appropriate electric potential between the two electrodes. The precise and controlled motion of the relative position of the nozzle and the substrate results in printing of

desired 3D pure metallic objects. The reduction of metal ions in an aqueous solution is represented by:

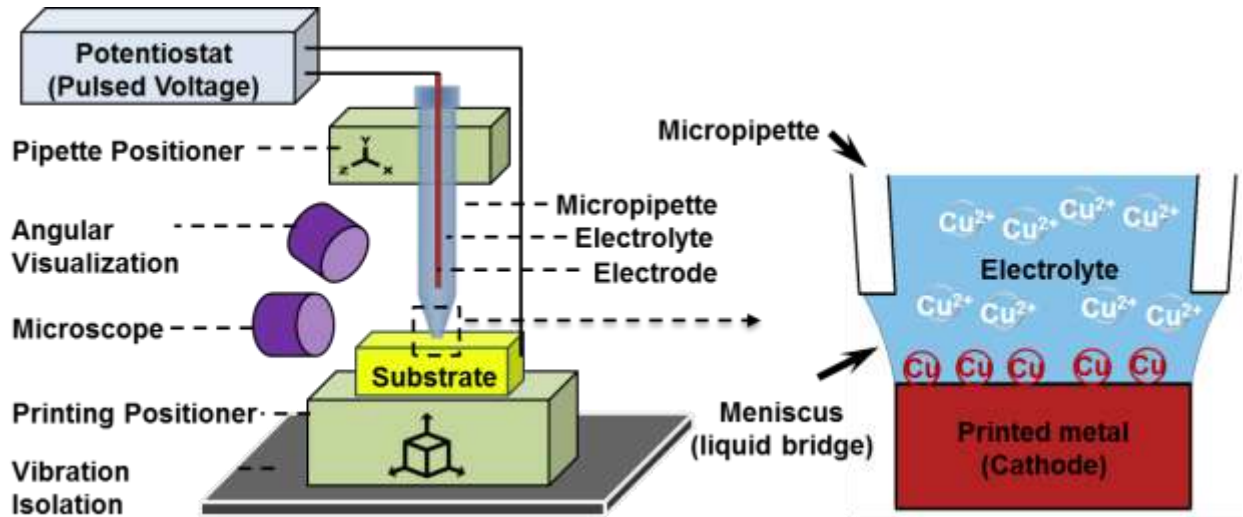


Figure 2.1. (Left) The schematic of LED printing setup and (Right) the close-up view of the nozzle and the electrolyte meniscus during deposition. The metal ions are deposited on the substrate by application of electrical potential using the potentiostat. The high precision 3-axis positioners are used for the positioning of the pipette and printing process.

### 2.1.1 Meniscus stability

A stable meniscus is required during the deposition process in order to obtain steady, continuous, and uniform printing. The wetting conditions between the micropipette and the wire growth front governs the stability of the meniscus. Synchronizing the deposition rate of the metal and the motion velocity of the positioning stages will stabilize the meniscus.<sup>1</sup> Additionally, the shape of the meniscus depends on the nozzle diameter, properties of the solution, the interfaces, and the withdrawal speed of the micropipette and the deposition rate of the wire. The profile of the

meniscus can be projected by solving the Laplace capillary differential equation for the equilibrium shape of the meniscus surface (Figure 2.2).<sup>33-35</sup>

$$z(r) = R \sin \alpha_0 \left( \cosh^{-1} \frac{r_0}{R \sin \alpha_0} - \cosh^{-1} \frac{r}{R \sin \alpha_0} \right) \quad (2)$$

where  $R$  is the radius of the wire, and  $r_0$  is the radius of the pipette tip;  $\varphi_0$  represents growth angle, and  $\alpha_0$  is equal to  $90^\circ - \varphi_0$ .

The value of  $\varphi_0$  depends on the surface energy of the electrolyte, deposited wire, and the surrounding environment.<sup>36</sup> The value of  $\varphi_0$  for air-copper-water system is  $12^\circ$ .<sup>1</sup> Therefore, the meniscus height in a stable condition is always lower than 28% of the pipette diameter.<sup>30, 31</sup> By increasing the deposition rate ( $v_N$ ) and stretching the meniscus, the height can be increased from zero up to the maximum meniscus height ( $H_{\max}$ ), whereas the deposited wire diameter is reduced from the pipette diameter ( $D_0$ ) to the value of  $D_{\min} = 0.5D_0$ . This region is where the meniscus is stable, and a continuous wire can be deposited. Increase in  $v_N$  shifts the meniscus height to the unstable region, which results in breakage of the liquid meniscus.

### 2.1.2 The multiphysics involved in the process

LED is a multi-physics process in which electrodeposition, fluid dynamics and mass and heat transfer physics are simultaneously involved. Within the electrolyte, the ionic flux is governed by multiple processes: diffusion, migration, and convection. This electrochemical processes can be described by the Nernst-Planck equation:

$$N_i = -D_i \nabla c_i - z_i u_i F c_i \nabla \phi_i + c_i u \quad (3)$$

in which  $N_i$  is the transport vector,  $D_i$  is the ionic species diffusivity,  $c_i$  is the concentration,  $z_i$  is the ionic species electronic charge,  $u_i$  is the charged species mobility,  $F$  is the Faraday constant, and  $\phi_l$  is electric potential difference in the electrolyte.

The charge transfer current or local current density ( $i_{ct}$ ) on the electrode surface can be described by the Butler-Volmer expression:

$$i_{ct} = i_0 \left\{ C_R \exp\left(\frac{\alpha_a F \eta}{RT}\right) - C_0 \exp\left(\frac{-\alpha_c F \eta}{RT}\right) \right\} \quad (4)$$

in which  $i_0$  is the exchange current density,  $C_R$  is the dimensionless concentration of the reduced species,  $C_0$  is dimensionless concentration of the oxidized species,  $\alpha_a$  and  $\alpha_c$  are charge-transfer coefficients for the anode and cathode, respectively, and  $\eta$  is the over-potential. The first and second terms in equation (4) represent the anodic and cathodic components of the local current density.

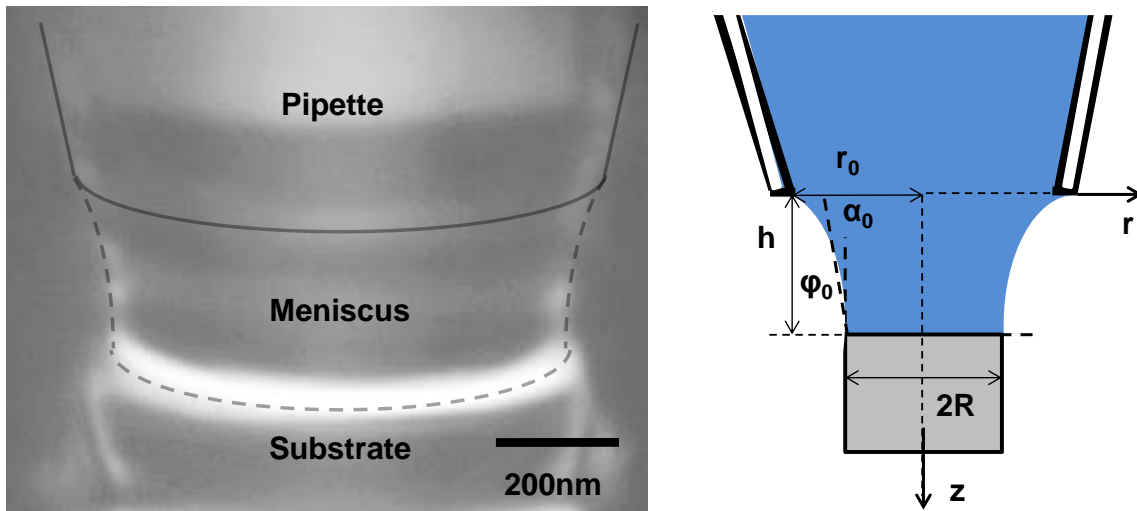


Figure 2.2. (Left) Side optical view and (right) the geometry details of the meniscus (Reprinted from Ref <sup>30</sup>, with the permission of AIP Publishing).

### 2.1.3 Effects of the environment relative humidity

Evaporation of water from the surface of meniscus has major contribution on the LED process. Therefore, the relative humidity (RH) of environment is one of the most important parameters that needed to be controlled during deposition. Evaporation can boost the deposition rate of the wire by increasing a convective flux within the electrolyte meniscus.<sup>30</sup> The experimentally measured values for wire deposition rate and deposition ionic current for two different values of relative humidity are compared in Table 2.1. The determination of RH value for stable deposition of uniform metallic structures depends on different parameters including: the electrolyte type, concentration, size of nozzle, radius of the wire, and temperature and pressure of the environment. Based on the multiphysics simulation, the RH in the range of 60 to 75 was chosen for the printing process.<sup>30</sup>

Table 2.1. Comparison of deposition rate and current for printing wires at two different RH.

<b>Relative humidity (%)</b>	<b>Deposition rate (nm/s)</b>	<b>Current (nA)</b>
60	100	1.1
75	80	0.7

### 2.1.4 Deposition rate

The nozzle speed affects the LED process by changing the diameter of the deposited wire. The change in the area of deposition alters the amount of ions deposited on the growth front and influences the concentration of ions within the meniscus. Additionally, it changes the evaporation of the water on the meniscus surface by changing its profile. The wire diameter vs. deposition rate for the pipette with the nozzle diameter of 730 nm are shown in Figure 2.3. By increasing the

deposition rate and stretching the meniscus, the diameter of deposited wire significantly decreases. Results showed that by changing the deposition rate at different printing process from 100 nm/s to 210 nm/s, the wire diameter gradually decreases from 650 nm to 460 nm. Increasing the deposition rate higher than 270 nm/s (point b), the meniscus becomes instable and breaks, and for slower rate than 100 nm/s (point a), the micropipette gets clogged. The clogging happens due to the small height of the meniscus when the deposition reaches the nozzle tip. The wire deposition rate ( $v_N$ ) can be expressed as:<sup>37</sup>

$$v_N = \frac{4iM}{nF\rho\pi D^2} \quad (5)$$

where  $M$  is the molar mass and  $\rho$  is the density of copper.  $i$  is the deposition current,  $n$  is the number of electrons per ions, and  $D$  is the wire diameter.

### 2.1.5 Growth current

In the electrodeposition process, the growth current is one of the critical parameters. Two modes of potentiostatic and galvanostatic can be employed to reduce the metal ions in this process. In the potentiostatic mode, the potential between the electrodes is controlled, while the current is measured as a dependent variable, while in the galvanostatic mode, the current between the electrodes is held constant using a current source, and the potential is measured as a function of time. In general, a three-electrode electrochemical cell is preferable in this process, because without a reference electrode the potentiostatic deposition can be problematic over time when the potential drop ( $iR$ -drop) through the electrolyte is high, and when the counter electrode is polarized due to application of high current density<sup>38</sup>. Currently, there is a limitation in adding a reference electrode in L-PED setup while using a nozzle with a small diameter. Therefore, the galvanostatic

mode is desirable in the L-PED process as no feedback from the reference electrode (in the three-electrode systems) is required during the process, which makes the cell system for galvanostat much simpler than the potentiostat. Schematic of an I-t (current vs. time) response for pulsed current in galvanostatic mode is depicted in Figure 2.4.

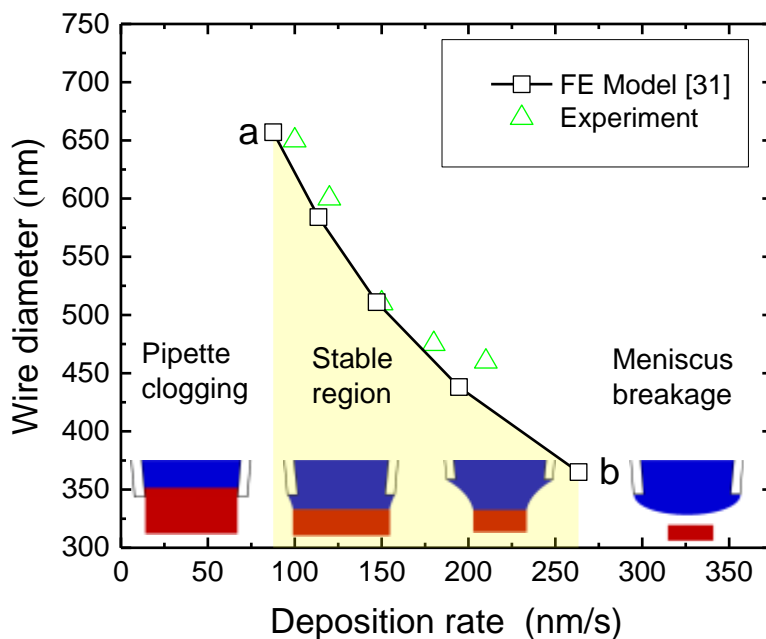


Figure 2.3. Dependence of wire diameter on pipette withdrawal speed compared to the FE (finite element) model (Reprinted from Ref <sup>31</sup>, with the permission of AIP Publishing).

In printing with nozzles of less than 1  $\mu\text{m}$  diameter, the  $iR$ -drop in the electrolyte is insignificant during the process ( $\sim\text{mV}$  range). Therefore, the potentiostatic mode with two-electrode cell system can be used in this process with nozzles of less than 1  $\mu\text{m}$  diameter, while keeping the relative humidity (RH) of the environment constant. This is because having a very small area of the working electrode (nozzle tip) results in very small current (nA range), regardless of the high resistance of the electrolyte due to the small tip size of the nozzle (resistance in the  $\text{M}\Omega$

range). Additionally, the counter electrode (or anode) does not get polarized due to a low current density resulting from the large surface area of anode (the surface area of the wire inside the pipette) compared to the working electrode (on the order of the area of the tip of the nozzle).

The evaporation rate is one of the key factors in the L-PED process<sup>30</sup>. During printing in the potentiostatic mode, the RH of the environment needs to be kept constant, because altering it results in change of ionic flux toward the cathode and change of the concentration of the ions at the cathode surface, and consequently change of the growth rate of the metal. However, in the galvanostatic mode, by maintaining the RH in a range (45-85%), one can 3D-print with a constant deposition rate throughout the process. During printing, the system varies the applied potential, which compensates for the change of ionic flux due to variation in the evaporation rate, and keeps the current and growth rate steady during printing (Figure 2.4). Therefore, the process is less dependent on the RH of the environment and evaporation of the electrolyte in the galvanostatic mode.

### 2.1.6 Cyclic voltammetry

In order to choose an appropriate printing potential in the potentiostatic mode, the deposition process was examined through *in situ* cyclic voltammetry (CV) at the tip of the nozzle (Figure 2.5). The process voltage was chosen after the cathodic reduction potential  $\sim 0.25\text{V}$  and before the hydrogen evolution potential. Formation of hydrogen bubbles at high potential can interrupt uniform deposition process. Figure 2.5 shows two cyclic voltammograms measured in the localized electrodeposition (LED) system with the nozzle filled with the solution of  $\text{CuSO}_4$  (100 mM) and  $\text{H}_2\text{SO}_4$  (1 M). The initial and switching voltages were  $-0.6\text{ V}$  and  $0.4\text{ V}$ , respectively, and the scan rate of the voltage was  $100\text{ mV/s}$ . The peaks at  $\sim -0.25\text{ V}$  show the reduction of  $\text{Cu}^{2+}$

to Cu in the two cycles. The deposition voltage was chosen after the obtained cathodic reduction potential and before the hydrogen evolution potential. After the hydrogen evolution potential, hydrogen bubbles are formed due to hydrogen evolution, and can disturb the deposition process.

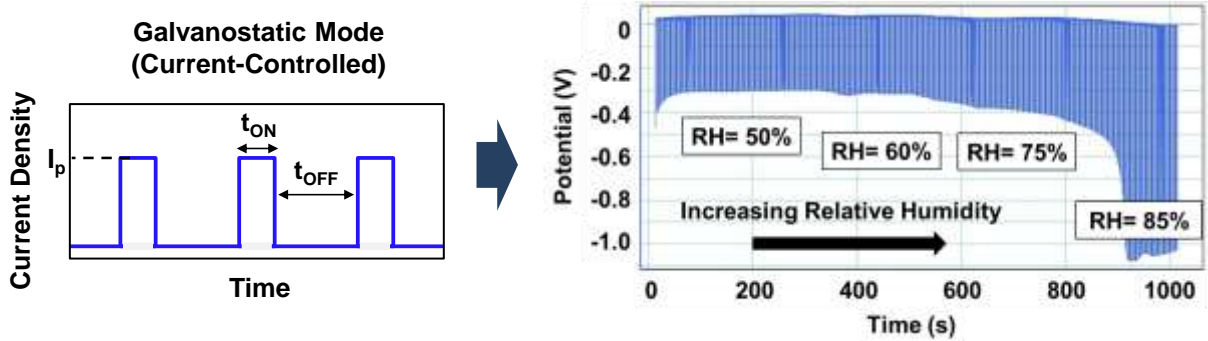


Figure 2.4. (Left) The schematic I-t (current-time) response for the galvanostatic mode, where the current between the electrodes is controlled, and the potential is a dependent variable as a function of time. (Right) Typical electric potential acquired during deposition of a micro-pillar in the galvanostatic mode while the RH was increasing. The system maintains the desired current during printing by varying the applied potential, and compensates for the changes of the ionic flux due to changes of RH.

## 2.2 3-D Printer Setup

Three-dimensional (3D) Cu micro/nano-structures were fabricated using a home-built computer-controlled setup (Figure 2.6). The system consists of different components and subsystems including a Faraday cage, a vibration isolation system, motion control, current measurement, humidity control, and visualization subsystems. The in-house made Faraday cage, composed of aluminum bars and copper mesh, shields the system from electrical fields. The cage distributes the charge around the cage's exterior. The system is mounted on an optical breadboard (Model M-IG-22-2, Newport, Inc.) with excellent rigidity and damping, and is placed on an active vibration control system (Model TS-150, Herzan, Inc.). The active vibration control system, which

delivers sub-hertz vibration isolation in all six degrees-of-freedom using advanced piezoelectric sensors, showed significant improvement in electrodeposition growth.

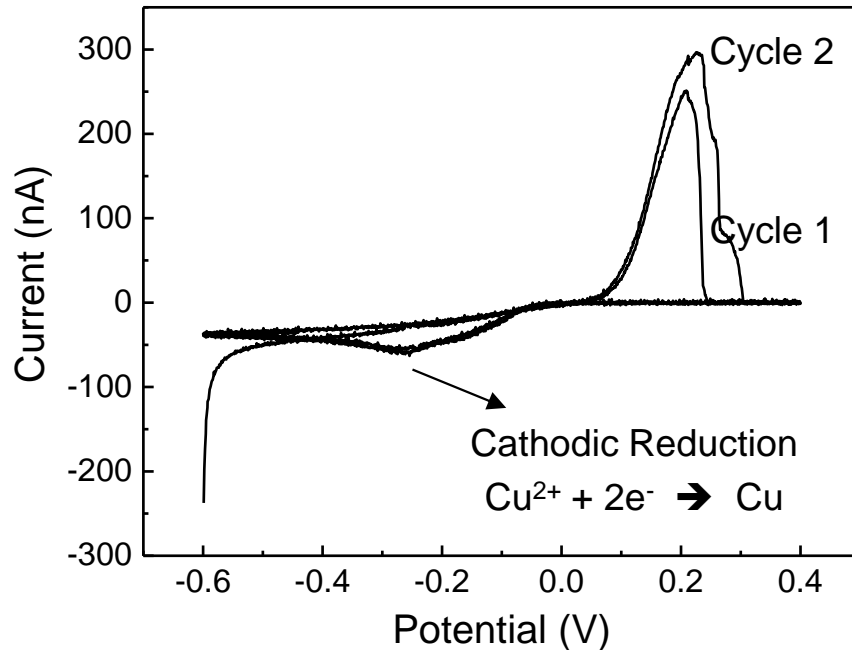


Figure 2.5. Cyclic voltammety obtained in situ at a scan rate of 100 mV/s. The peaks at  $\sim -0.25$  V indicate the reduction of  $\text{Cu}^{2+}$  to Cu. The deposition potential during 3D printing was set after the cathodic reduction potential.

A three-axis linear translation stage handled the coarse motion control of the nozzle to approach to the substrate and form the meniscus. The XYZ coarse stage (Model 9067-XYZ-PPP, New Focus, Inc.) consists of three combined linear translation stages configured with piezo linear actuators (Model 8302 Picomotor, New Focus, Inc.). The actuators can be either adjusted manually or driven by an open-loop intelligent motion controller/driver (Model 8742, New Focus, Inc.). The stage provides smooth and accurate positioning with minimum incremental motion of less than 30 nm and a travel range of 25.4 mm. Additionally, a piezo-based three-axis nano-positioning linear stage (Model NPXYZ100SG-D, Newport, Inc.) with a fine resolution of 4 nm and a universal

controller (Model XPS-Q6, Newport, Inc.), connected to a computer was utilized to control the positioning and velocity of the substrate during the printing process by a LABVIEW program.

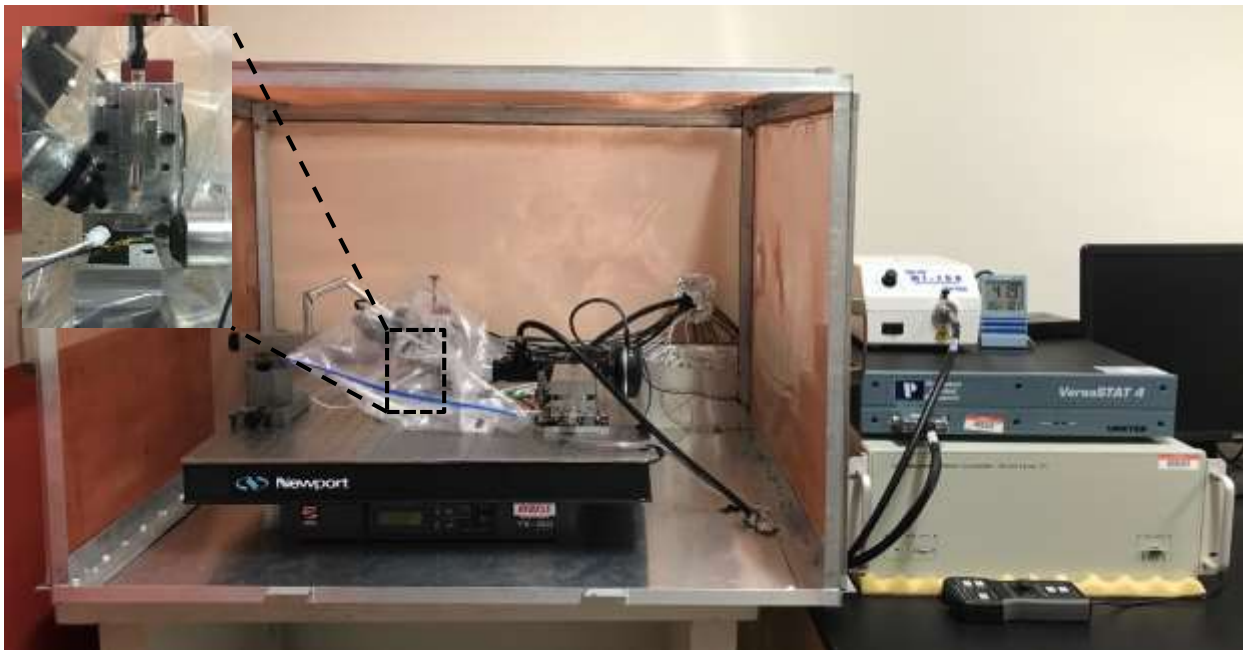


Figure 2.6. The homebuilt 3D printer setup inside a Faraday cage, including a vibration isolation system, motion control stages, a humidity chamber, a visualization system, a potentiostat, and controllers. The inset shows the close-up view of the print-head inside the chamber.

As the working tool, glass micropipettes with micron to sub-micron diameter dispensing nozzles were fabricated using a pipette puller (Model P-97, Sutter Instrument) (Figure 2.7). The pipettes are filled with electrolyte of metal of interest. For instance, in printing Cu structures, the nozzle was filled with a solution of  $\text{CuSO}_4$  (100 mM) and  $\text{H}_2\text{SO}_4$  (1 M). A gold-coated silicon substrate and a copper wire served as the working electrode and counter electrode in the cell, respectively. An electrical potential is needed to be applied between two electrodes in the system to reduce the metal ions in the electrolyte and deposit them on the substrate. A potentiostat/galvanostat (VersaSTAT 4, Princeton Applied Research) was employed to apply the

appropriate electrical potential between the two electrodes and to control the electrodeposition process.

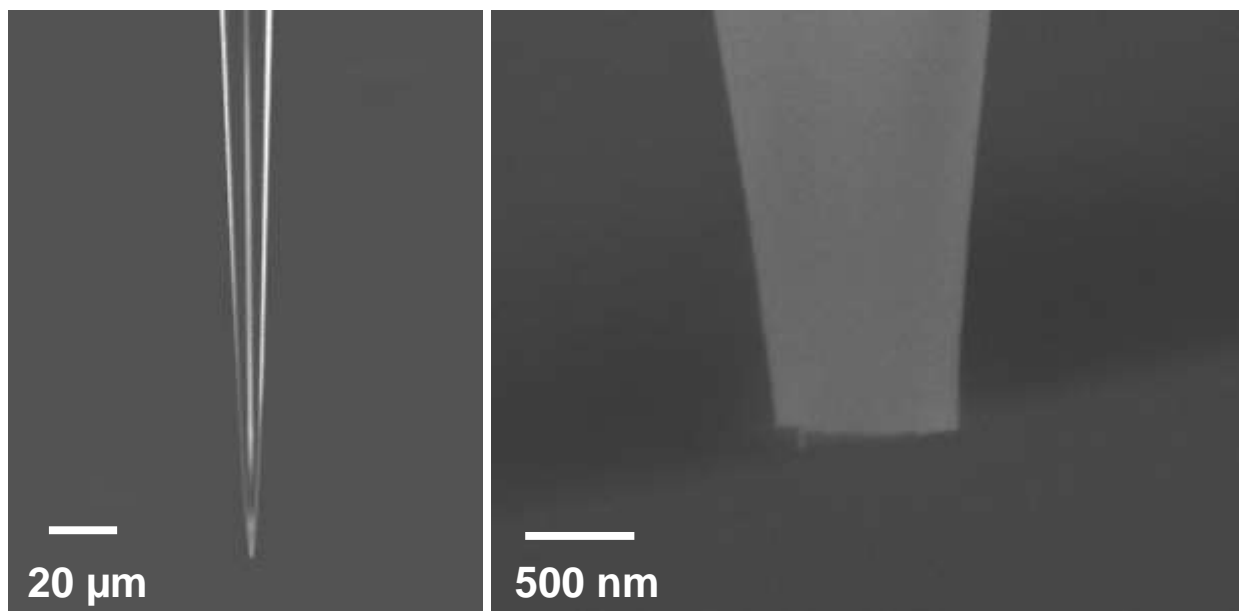


Figure 2.7. The SEM images of a fabricated glass nozzle with a diameter of 840 nm using pipette puller.

The evaporation rate of electrolyte in meniscus plays a critical role in meniscus-confined electrodeposition. Hence, a flexible transparent Ziploc bag was used to enclose the electrodeposition environment and avoid exposing all the electronics to the humidity. The humidity was obtained using an ultrasonic humidifier and controlled by a remote hygrometer. A handheld digital microscope (Model AM4115ZTL Edge, Dino-Lite, Inc.) was used for top angular observation of the substrate surface and controlling the coarse motion of the pipette. A magnification range of 10X to 140X was achieved with large working distance using this microscope. The printing process was controlled in situ by using a house-made microscope consisting of long working distance optical objective lens (Model 100X Plan Apo SL Infinity Corrected Objective, Mitutoyo), a CCD camera (Model XM-10, Olympus), an in-line tube

assembly (Model InfiniTube standard w/ in-line assembly, Infinity), and a fiber optic illuminator (Model M-150, Dolan-Jenner). A XYZ stage (Model M-562-XYZ ULTRAlign Precision XYZ Linear Stage, Newport, Inc.) that included three micrometers with resolution of 1  $\mu\text{m}$  was used for positioning of the microscope.

## CHAPTER 3

# LOCALIZED PULSED ELECTRODEPOSITON PROCESS FOR 3D PRINTING OF NANOTWINNED METALLIC NANOSTRUCTURES

### 3.1 Introduction

The capability of direct printing of three-dimensional (3D) nanoscale metallic structures with controlled microstructure is useful for applications in nanoelectronics, 3D integrated circuits (ICs) and wire bonds, micro/nano electromechanical systems (MEMS/NEMS), plasmonics, metamaterials, and sensors.<sup>1, 2, 30, 31</sup> Additionally, such capability will be useful for fundamental studies on process-microstructure-property relationships of metals, since desired geometries such as micro-pillars for micro-compression experiments can be directly printed, instead of subtractive fabrication using focused ion beam (FIB) milling, which are costly and may introduce damage into the metal. Current laser-based 3D printing processes for metals are not suitable for micro/nanoscale applications, given the intrinsic size of the metal powder particles in the range of 10-100 microns.<sup>17</sup> Processes based on 3D extrusion of metal particles immersed in organic binders do not offer much control over microstructure, and require post-processing to eliminate the organic phase to obtain high quality pure metal.<sup>18</sup> Since the microstructure of a metal determines its properties, controlling it in the printed metal part is critical, and has been the focus of major efforts in the field of additive manufacturing (AM). To date, there is no established method for controlling the microstructure of 3D printed metals, in particular at the micro/nanoscale.

---

\*Reproduced with permission from Soheil Daryadel, Ali Behroozfar, S. Reza Morsali, Salvador Moreno, Mahmoud Baniasadi, Julia Bykova, Rodrigo A. Bernal, and Majid Minary-Jolandan, Localized Pulsed Electrodeposition Process for Three-Dimensional Printing of Nanotwinned Metallic Nanostructures, *Nano Letters* 2018 18 (1), 208-214, Copyright (2018) American Chemical Society

Nanotwinned (nt) metals offer several unique advantages for nanoscale applications. They have a unique microstructure with grains that contain a high density of layered nanoscale twins divided by coherent twin boundaries (TBs). These metals often show higher strength and ductility compared to their nanocrystalline (nc) counterpart, since TBs can effectively block dislocation motion.<sup>19-23, 39-45</sup> They also exhibit more resistance to electromigration<sup>24</sup>, which is a common problem for metals at the nanoscale. Nt-metals in film and bulk forms are obtained using physical and chemical processes including pulsed electrodeposition (PED), plastic deformation, recrystallization, phase transformation, and sputter deposition.<sup>19, 23, 46</sup> However, no process for 3D printing (or AM) of nt-metals has been introduced so far. Given their unique properties, it is desirable to establish an AM process for nt-metals.

AM enables flexible, efficient, and high-resolution patterning of 3D structures. In particular, 3D printing of copper microstructures have been explored over the last several years for applications that require localized fabrication, such as interconnects for electronics, high-frequency coil antennas for microwave transmission, and probe-based techniques.<sup>1, 12-16</sup> While some of these novel AM techniques have made major advances for fabricating complex 3D microstructures, material and mechanical characteristics of the printed structures are still a matter of research.<sup>47</sup>

In this chapter, the localized pulsed electrodeposition (L-PED) process for direct printing of 3D free-standing nanotwinned Cu (nt-Cu) nanostructures is demonstrated. 3D nt-Cu structures were manufactured using the L-PED process at the tip of an electrolyte containing nozzle. The FIB and transmission electron microscopy (TEM) analysis confirmed formation of coherent TBs in the 3D printed Cu. A unique advantage of the L-PED process is that it enables direct 3D printing of

micro-pillars (often fabricated using FIB milling) for characterization. The mechanical properties of the directly 3D-printed nt-Cu micro-pillars was studied using *in situ* SEM micro-compression experiments. The microstructure and mechanical properties of the nt-Cu were compared to nc-Cu printed using the same method under direct current (DC) voltage.

### 3.1.1 Nanotwin formation in PED

In the DC process, a constant voltage is applied during the printing process, which results in a constant rate deposition. However, in the PED process, the potential is repeatedly alternated between ON and OFF with the time intervals of  $t_{on}$  and  $t_{off}$ , respectively. PED is a technique for electrodeposition of metals.<sup>39</sup> In this technique, a very high current density (on the order of A/cm<sup>2</sup>) and subsequently high deposition rate and high density of nucleation sites are achieved during the short period of ON-time. Although the exact mechanism of twin formation in PED is still a matter of debate,<sup>41, 44, 48</sup> it is generally believed that stress relaxation during the  $t_{off}$  results in formation of twins.<sup>25, 26</sup>

Previous studies have shown the effect of stress generation and relaxation on the formation process of nanoscale twins.<sup>49</sup> Direct in situ experimental investigation of stress evolution was performed by precise measurement of the deflection of a flexible cathode during deposition process.<sup>50</sup> While DC deposition have revealed compression-tension-compression transition, the stress evolution in PED exhibited significantly different behavior. In PED, there was periodic increase in tensile stress and stress relaxation during the ON time and OFF time, respectively. Interestingly, the twin spacing was predicted using the measured average stress, which was in agreement with the observed twin size in TEM.<sup>50</sup>

The formation process and growth of nanoscale twins have been proposed in more details using in situ SEM morphology analysis combined with MD simulation.<sup>51</sup> It was found that due to the high level of stress during the ON-time the twin nuclei originate at triple junctions of GBs (grain boundaries), and during the OFF-time they are extended along the lateral (111) direction. The consecutive nucleation and extension results in growth of nt-Cu structure, layer by layer.

Also, the interruption in current results in desorption of impurities and inhibitors from the growing deposit, and replenishes the metal ions in the diffusion layer. In the PED of Cu, this phenomena stimulate grain growth rather than the formation of new grains; and an increase in the OFF-time increases the grain size.<sup>52</sup> The OFF-time also enables recovering the consumed ions during deposition, and provides higher concentration of ions on the cathode, and facilitates the passage of the ions through the charged double layer.<sup>53</sup> It should be noted that during the “on” cycle ( $t_{on}$ ), the concentration of ions will gradually decrease due to the ion consumption. In this dissertation, all structures were printed in the potentiostatic mode (constant voltage). Therefore, the current density and deposition rate would decrease during  $t_{on}$ . However, this change is negligible due to the short period time of the “on” cycle (~20 ms).

## **3.2 Materials and methods**

### **3.2.1 Materials**

Three-dimensional (3D) Cu micro/nano-structures were fabricated using a home-built computer-controlled setup. The nozzle was filled with a solution of CuSO<sub>4</sub> (100 mM) and H<sub>2</sub>SO<sub>4</sub> (1 M). A gold-coated silicon substrate and a copper wire served as the working electrode and

counter electrode in the cell, respectively. Environmental humidity was controlled by a remote hygrometer at a constant relative humidity of ~60% within an enclosure around the setup.

### **3.2.2 Microstructural characterization**

Microstructural characterization of the 3D-printed micro-pillars was conducted in as-deposited condition. The cross-section microstructure of the material was studied using high-resolution focused ion beam (FIB) imaging (FEI Nova Nanolab 200). Due to small size of the pillars and destructive nature of this technique, the FIB sample preparation is not trivial. For this reason, platinum was deposited around the wire to enable the high-resolution imaging (Figure 3.1B). Cross-section of the sample was milled at a final acceleration voltage of 30 keV and current of 10 pA, and imaging was performed using the same parameters. The ion channeling contrast images were used for estimation of the grain size and observation of the twins.

Transmission electron microscopy (JEM 2100F Imaging TEM) was utilized to observe more detailed microstructure of the electrodeposited specimens. The TEM specimens were prepared by conventional FIB lift-out procedure (Figure 3.1D-F). Similar to FIB sample preparation, coating the specimens in a thick layer of Pt prior to the lift-out is required to protect them against the ion damage. The wire and the substrate lamellae were lift out and transferred onto a Cu TEM grid using a nanomanipulator (Omni probe 400). The specimens were thinned down to ~100 nm by using FIB using parameters of 5 keV and 46 pA.

### **3.2.3 Micro-compression experiment**

The uniaxial micro-compression experiments were carried out on the printed micro-pillars *in situ* SEM using a nanoindentation system (NanoFlip, Nanomechanics). The samples diameter

was  $\sim 709 \pm 13$  nm, and had the length-to-diameter aspect ratio of  $\sim 3:1$  to minimize the effects of buckling and other artifacts.<sup>3</sup> A conductive 10  $\mu\text{m}$  diameter flat punch was used as the compression anvil. The conductive tip does not get charged by the electron beam, which makes it more suitable for in situ SEM experiments. All experiments were run under displacement control mode at a constant displacement rate of 2 nm/s in order to achieve the constant strain rate of  $1 \times 10^{-3} \text{ s}^{-1}$  ( $\dot{\epsilon} = \dot{L}/L$ ). Five samples were tested for each deposition type. The stress-strain response was calculated based on the obtained load- displacement, and the geometry of each specimen.

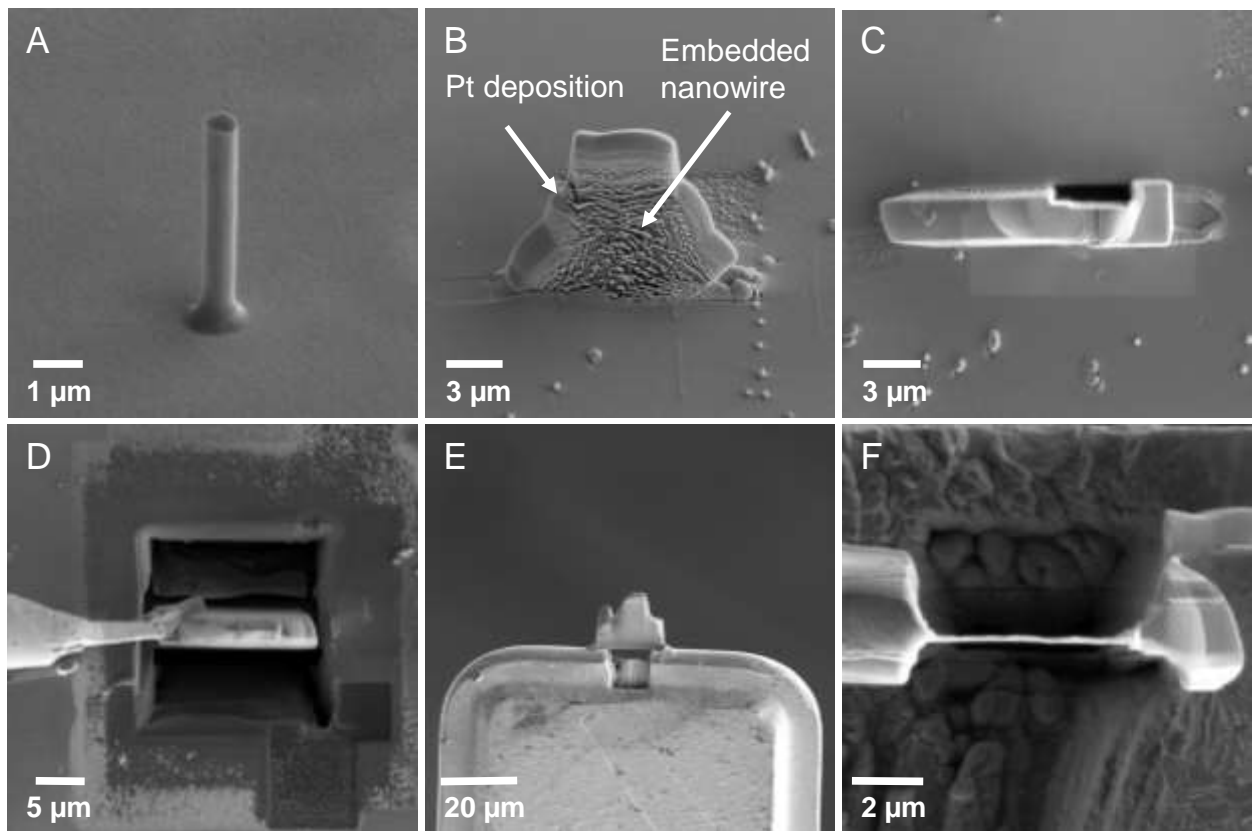


Figure 3.1. Sample preparation for microstructural characterization. (A) The SEM image of the wire. (B) The wire was embedded in Pt deposition, and (C) the cross-section was milled in order to enable FIB imaging. (D) - (F) The lift-out and FIB thinning procedure for TEM imaging. The wire was coated in a Pt protective layer, and transferred to a Cu TEM grid. The specimen was milled from both sides to reach 100 nm thickness for TEM imaging.

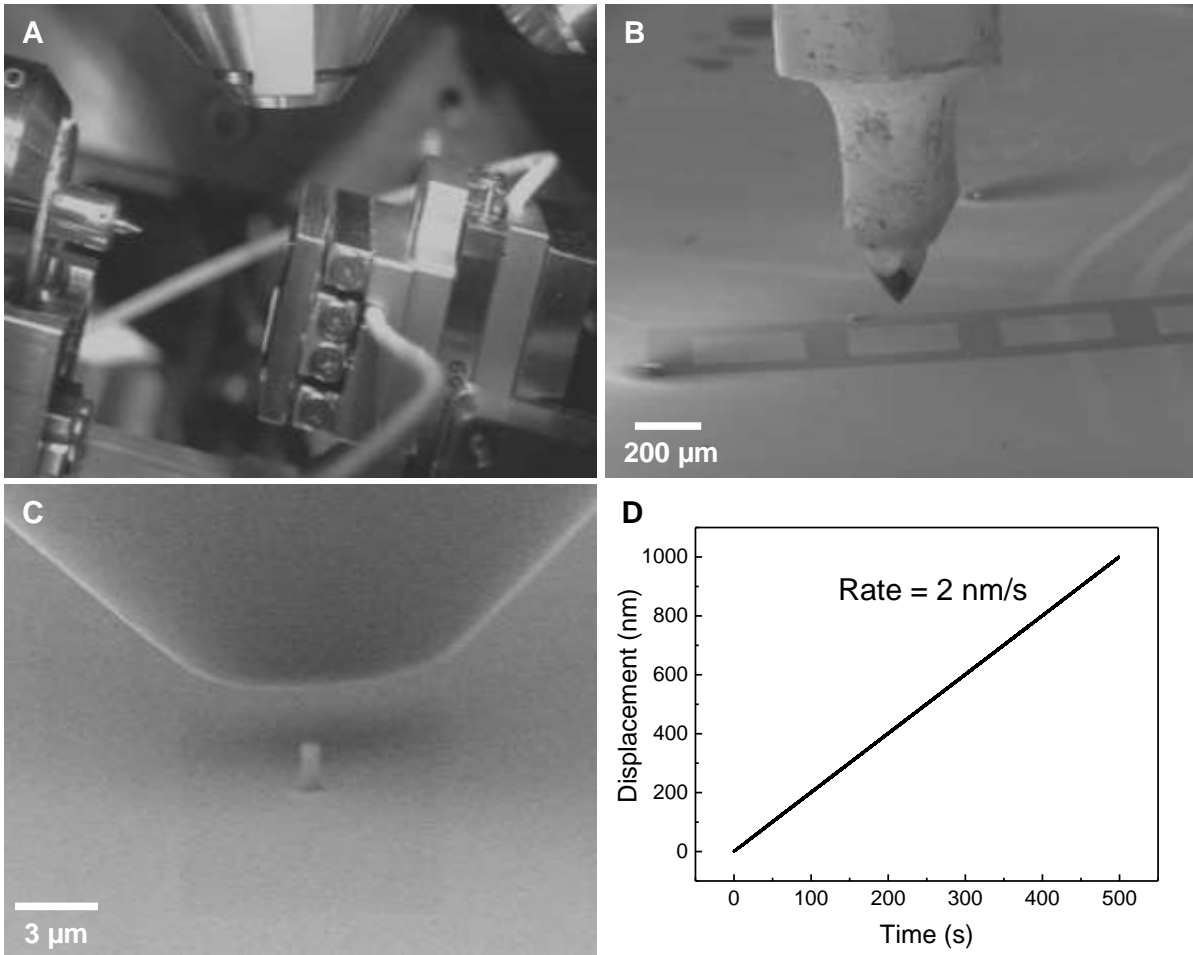


Figure 3.2. (A) - (C) In situ micro-compression experiment using a 10  $\mu\text{m}$  diameter flat punch tip. (D) A typical displacement history during micro-compression test. The rate of displacement was 2 nm/s.

### 3.3 Results and discussion

#### 3.3.1 Additive manufacturing of nanotwinned nanostructures

The L-PED printed structure is schematically shown in Figure 3.3. A detailed description of the setup is provided in Chapter 2. In the L-PED process, the metal ions are reduced at the growth front within the meniscus area on the cathode by application of a pulsed electric potential between counter electrode and the substrate (working electrode). The unique advantage of the L-PED process is the possibility of the control over the spatial microstructure of the printed metal in 3D

geometries. This is because the applied voltage can be controlled during the 3D printing process, for example direct current electrodeposition (DC-ED) or PED with arbitrary duty cycles can be applied (Fig. 3.4A, B top panel). More specifically, it is demonstrated that through the application of a pulsed voltage, nt-metals can be 3D-printed. Additionally, the process does not require any post-processing, since the printed material is pure metal without any additives or binders.

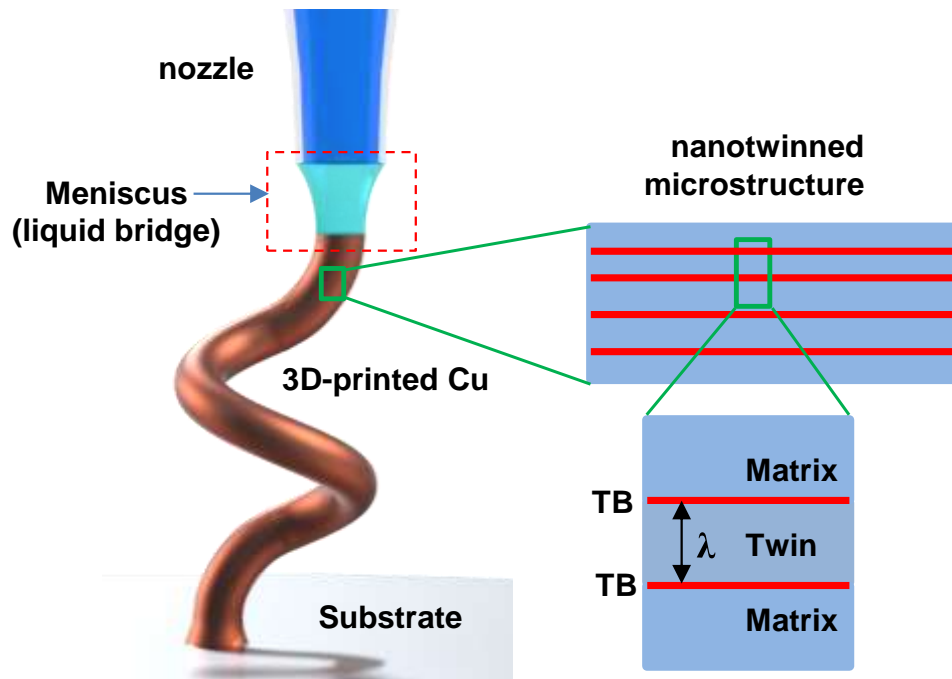


Figure 3.3. The schematic close-up view of the nozzle and the electrolyte meniscus during L-PED 3D electrodeposition. Metal ions are reduced at the growth front under an applied pulsed electric potential between the anode and cathode. Through application of a pulsed voltage, nanotwinned metals can be printed in arbitrary 3D geometries.

The process is capable of printing various geometries such as straight wires, angled wires, and helical wires (Figure 3.4A-C). Figure 3.4C shows wires 3D-printed continuously by the L-PED process with various angles from  $90^\circ$  to  $40^\circ$  next to each other. Using a flat end micropipette as nozzle, there is a limiting angle for the meniscus during printing. However, for smaller angles, the pipette tip can be modified using the FIB to enable low angle and lateral printing.<sup>1</sup> Since metal ions reduction occurs only during the  $t_{on}$  in L-PED, the deposition rate in PED is much lower than

DC-ED. For Cu structures in this work, the printing rate was  $\sim 250$  nm/s and  $\sim 15$  nm/s for DC-ED and PED, respectively.

It's noteworthy that in both techniques, the deposition rate can be enhanced by adjusting the deposition parameters, such as the applied voltage, electrolyte concentration, relative humidity, on-time, and off-time. However, there are some limitation for each parameter. For instance, increasing the ion concentration in micropipettes with smaller diameter will cause clogging of the tip due to high evaporation rate. Also there is a limit for the applied voltage to avoid the hydrogen evolution in electrolyte. Such limitations also exist in the deposition rate of nt-films, and is inherent to electrochemical deposition process. Figure 3.4D shows an arrays of 31 Copper micro-pillars that form the word "UTD", printed by the L-PED process. The deposition time for each micro-pillar was  $\sim 200$  s (total time of  $\sim 103$  minutes). Micro-pillars had a diameter distribution of  $890 \pm 70$  nm. it was found that all printed structures were mechanically stable over time, and their bonding to the substrate was strong.

For microstructural and mechanical characterization, Cu pillars of  $\sim 710 \pm 17$  nm in diameter were 3D-printed using the L-PED process. A unique advantage of the direct 3D printing of micro-pillars is avoiding the FIB-induced damages to the material surface. In order to choose an appropriate printing potential, the deposition process was examined through *in situ* cyclic voltammetry (CV) at the tip of the nozzle. The DC-ED wires with diameter of  $708 \pm 8$  were obtained at a potential of  $-0.4$  V and an average current density of  $\sim 0.64$  A/cm<sup>2</sup>, while the PED wires were deposited at  $t_{on}$  voltage of  $-0.4$  V and a peak current density of  $\sim 3.32$  A/cm<sup>2</sup>. For PED,  $t_{on} = 20$  ms, and  $t_{off} = 2$ s were used, with an average current density of  $\sim 0.03$  A/cm<sup>2</sup>. The detailed process parameters are given in Table 3.1.

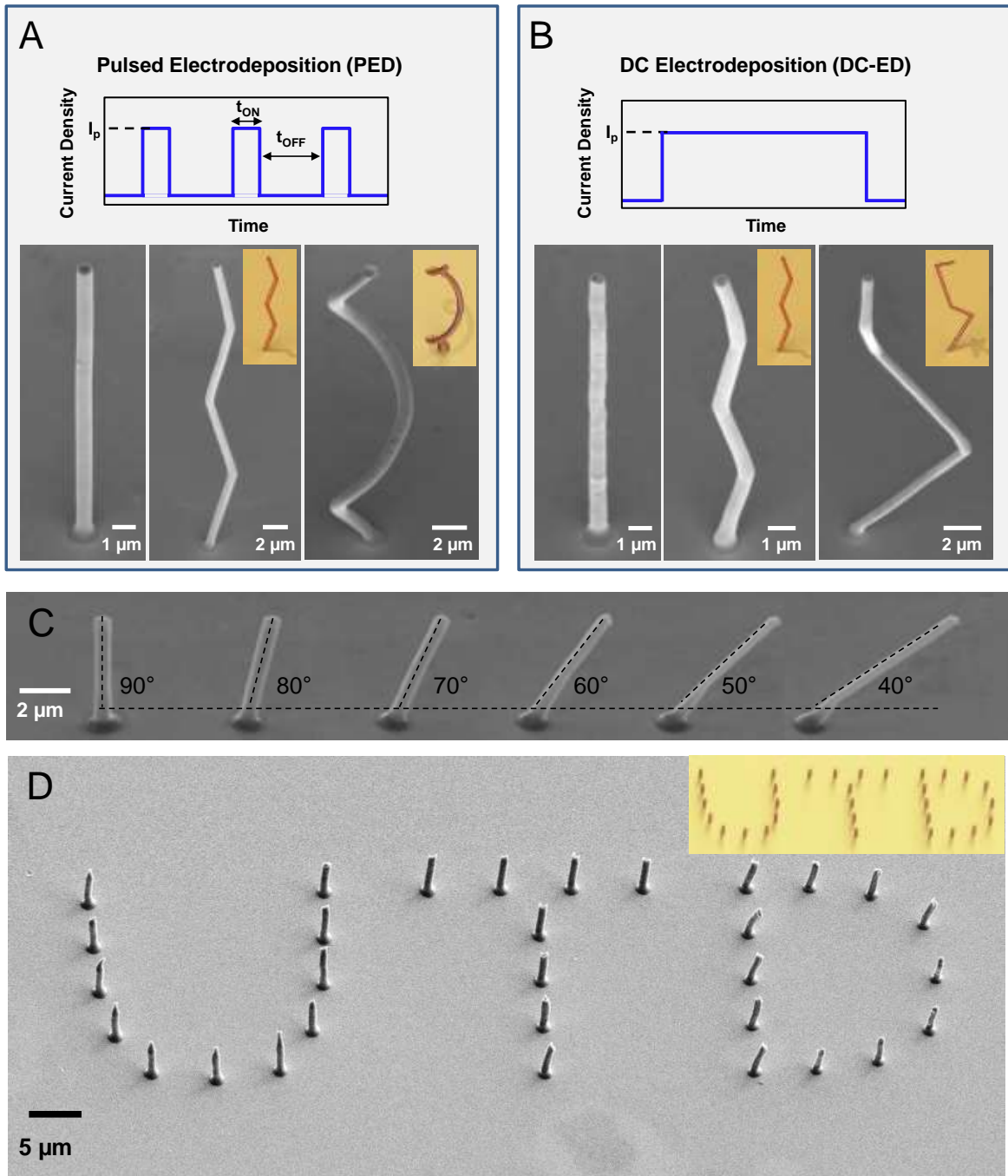


Figure 3.4. 3D-printed Cu wires using (A) pulsed electrodeposition (PED), and (B) direct current electrodeposition (DC-ED). The insets are 3D schematics of the printed metal. (C) 3D-printed wires using the L-PED process with various angles with respect to the substrate, from  $\sim 90^\circ$  to  $\sim 40^\circ$ . For better presentation, the SEM images of individual angled wires are combined. (D) “UTD”-shaped array of 31 copper pillars, printed by the L-PED process. The diameter of the wires are in the range of 500 nm to 1000 nm depending on the nozzles diameter.

Table 3.1. Process parameters for fabrication of micro-pillars using PED and DC-ED processes.

Electrodeposition mode	ON/OFF voltage (V)	ON/OFF time (s)	Duty cycle	Peak current density (A/cm <sup>2</sup> )	Average current density (A/cm <sup>2</sup> )	Deposition rate (nm/s)	Diameter (nm)
PED	-0.4/0	0.02/2	1/100	3.23	0.03	15	710 ± 17
DC-ED	-0.4/-	-	-	-	0.64	250	708 ± 8

Additionally, a pattern of deposited material can be printed on the substrate by moving the nozzle on the surface along a defined path. Repeating the pattern results in a 3D layer-by-layer structure. Layer-by-layer printed Cu structures and patterns are presented in Figures 3.5. The structure in Figure 3.5A is a 2-layer 10 μm by 10 μm hollow square directly written from a CAD model, and Figure 3.5B is a 5 μm 10-layer wall printed by layer-by-layer process. These structures are deposited using -0.4 V ON-voltage, 20 ms ON-time, and 0.04 A/cm<sup>2</sup> average current density. Figure 3.5D and E are printed using the same parameters with a larger pipette with ~5 μm diameter.

### 3.3.2 Microstructural characterization

Energy dispersive X-ray spectroscopy (EDS) analysis of PED and DC-ED wires are presented in Figure 3.6. The acquired spectra from the selected area showed that the printed materials are largely free of impurities (Figure 3.6C). The results revealed high purity Cu in the deposited structures with no significant presence of oxygen (< 0.8 wt. %). Given the room environment process, after printing small amount of oxygen may be present on the surface of both the substrate and micro-pillars. Since Cu has tendency to quickly oxidize at room environment, if the intended application demands no oxygen on the surface of the printed Cu, it must be printed in a controlled environment and quickly passivated. The Gold (Au), Chromium (Cr), and Silicon (Si) in the spectra originate from the substrate surface. It is noted that sulfur (S) would appear at ~2.3

keV. No peak was observed at this energy level and a small peak that appeared at > 2.4 keV was assigned to gold.

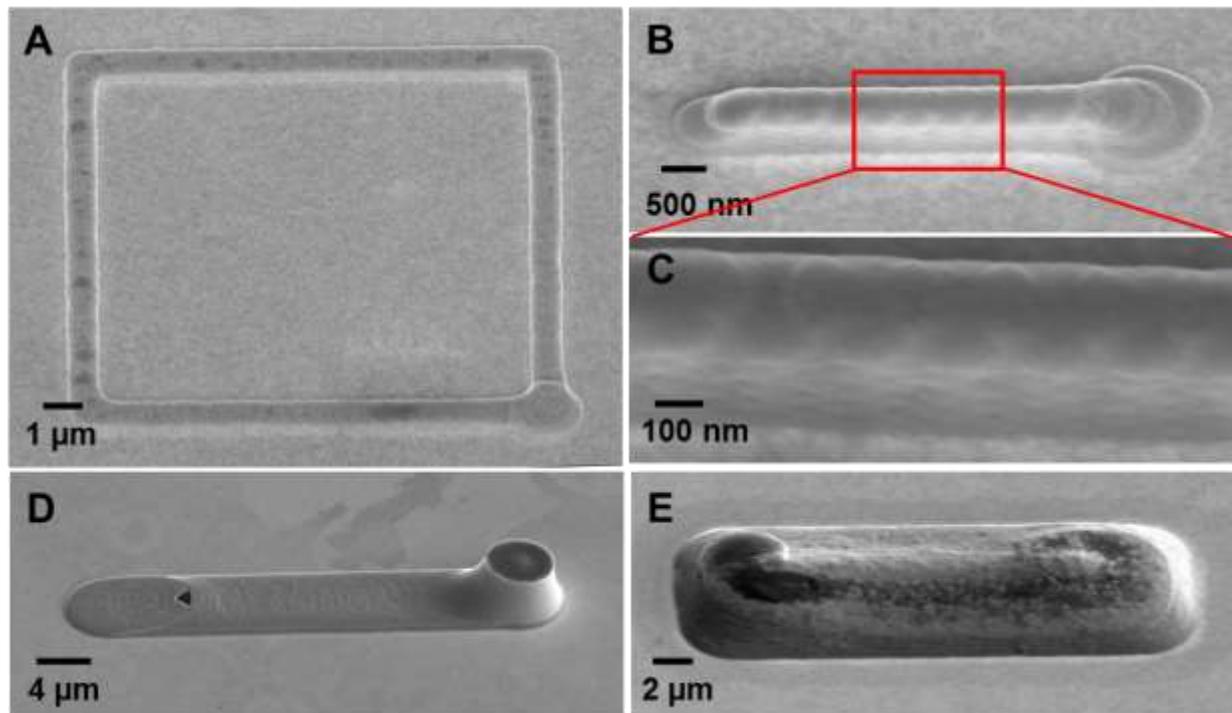


Figure 3.5. SEM images of the layer-by-layer printed structure using the L-PED process. (A) 2-layer 10  $\mu\text{m}$  by 10  $\mu\text{m}$  hollow square, (B) 5  $\mu\text{m}$  10-layer wall and (C) zoom-in view of the red box, printed with a micropipette of  $\sim 800$  nm diameter. (D) 7-layer 30  $\mu\text{m}$  line deposition followed by a 3  $\mu\text{m}$  pillar deposition, and (E) 10-layer 30  $\mu\text{m}$  by 8  $\mu\text{m}$  cube deposition using a  $\sim 5$   $\mu\text{m}$  diameter pipette.

It is desirable that an electrodeposition processes to be carried out with high current efficiency (CE). To calculate the CE of the process, the actual deposition rate of 10 different wires printed by PED and DC-ED processes were compared to the analytically calculated growth rate of the wires, defined by the Faraday's law ( $v = \frac{4iM}{nF\rho\pi D^2}$ ), where  $i$  is the deposition current,  $M$  is the molar mass,  $n$  is the number of electrons per ions,  $F$  is the Faraday constant,  $\rho$  is the mass density, and  $D$  is the wire diameter (Table 3.2).<sup>1</sup> The average CE of the Cu deposition was calculated to be  $93 \pm 3 \%$ .

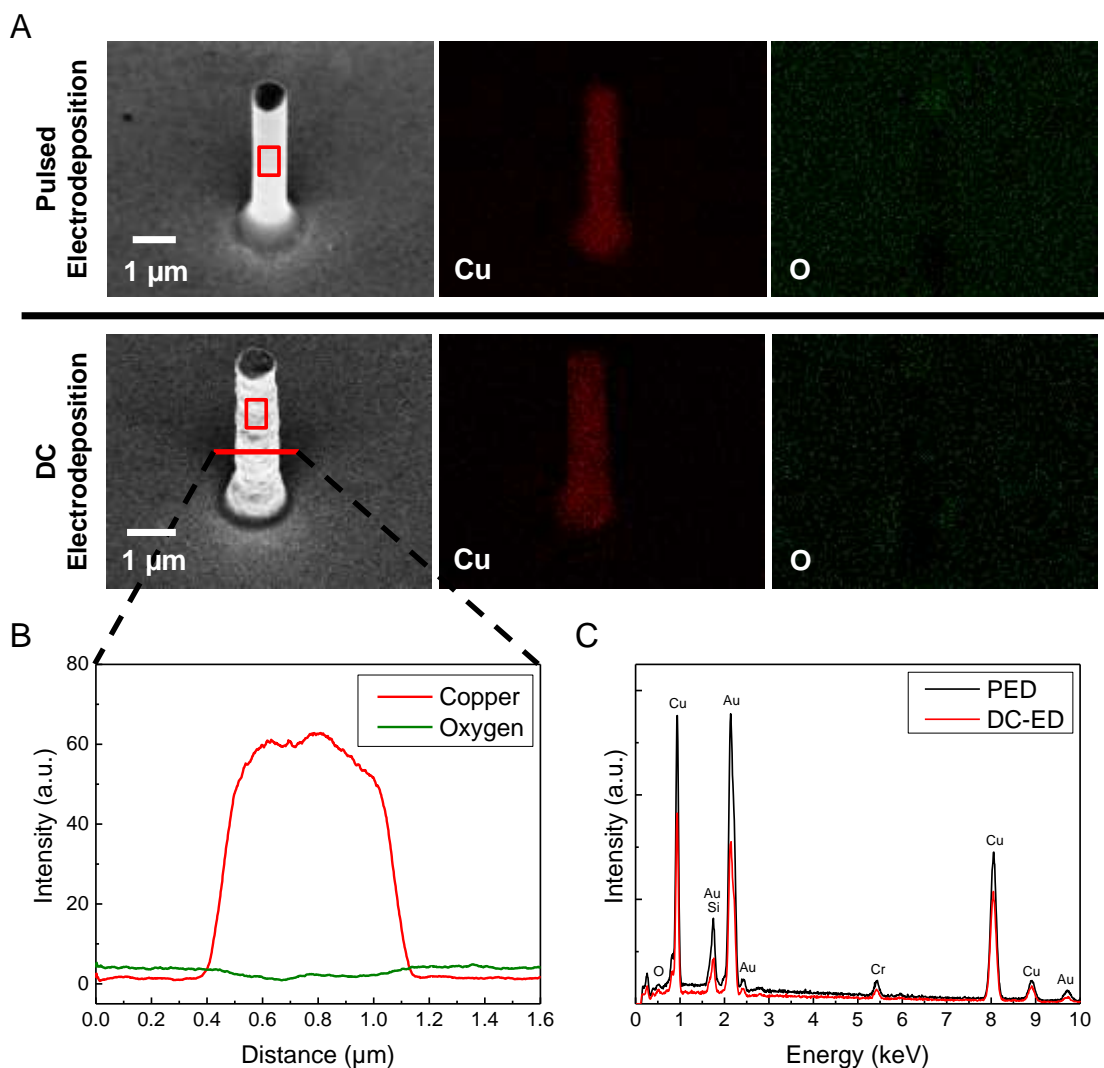


Figure 3.6. EDS (A) map and (B) line analysis acquired from the PED and DC-ED deposited wires. (C) The spectra from the selected area (red squares) show pure Cu deposition free of impurities.

Figure 3.7 shows FIB ion contrast channel image of a micro-pillar continuously printed using L-PED and DC-ED at deposition rate of 5 nm/s. The first 4 μm height of the pillar was deposited using pulsed voltage and the next 4 μm was continued using DC voltage. The average current density was kept constant ( $0.011 \text{ A/cm}^2$ ) for both methods during deposition. Two distinct regions with different microstructures can be found in the ion contrast image of the cross-section. Results revealed that the microstructure of the printed Cu pillar is changed due to introduction of

the off-time. Larger grain sizes were observed for the DC-ED section, and the channeling contrast in the PED region confirmed the existence of nanotwins within the grains.

Table 3.2. The dimension, deposition rate, and current efficiency of the wires electrodeposited using PED and DC-ED processes.

Electrodeposition Mode	Diameter (nm)	Height (nm)	Deposition Rate (nm/s)	Theoretical Deposition Rate (nm/s)	Current Efficiency (%)
PED	722	2172	15	16.79	89.33
PED	713	2276	15	16.01	93.67
PED	731	2100	15	16.89	88.80
PED	695	2070	15	16.03	93.58
PED	690	2160	15	16.31	91.96
DC-ED	704	2054	250	262.56	95.22
DC-ED	705	2122	250	263.95	94.72
DC-ED	700	2128	250	279.25	89.52
DC-ED	714	2114	250	255.48	97.85
DC-ED	720	2186	250	261.73	95.52

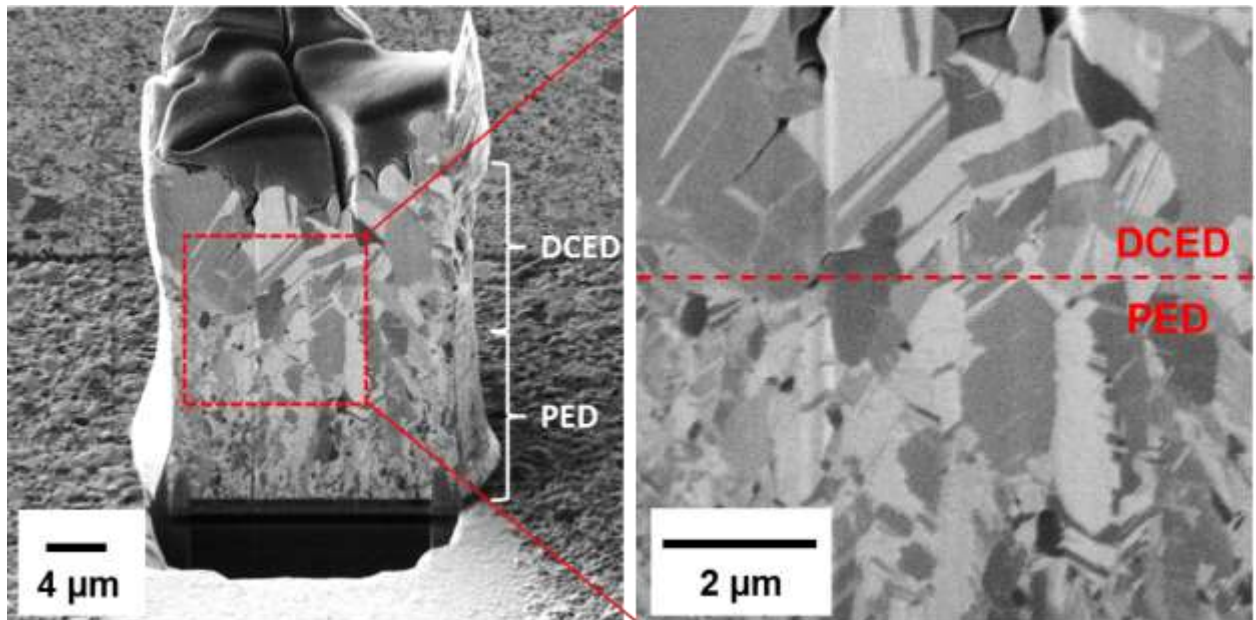


Figure 3.7. (Left) FIB ion channeling contrast image of a micro-pillar deposited using PED and DC-ED techniques. The first 4  $\mu\text{m}$  height of the pillar was deposited using pulsed voltage and the next 4  $\mu\text{m}$  was continued using DC voltage with an average current density of 0.011  $\text{A}/\text{cm}^2$ . (Right) Magnified view of the approximate boundary between the two methods (Reprinted from Ref <sup>54</sup>, with the permission of John Wiley and Sons).

Figures 3.8A and E show the cross-sectional FIB ion channeling contrast images of the wires printed using PED and DC-ED processes, respectively. Both wires are nanocrystalline, however the channeling contrast in the PED samples revealed the existence of nanotwins within most of the grains. Noticeably, introduction of the OFF-time during the PED changed the microstructure of the printed metal. The PED deposited wires exhibited nanocrystalline nanotwinned (nc-nt) microstructure with columnar-shape grains with an average diameter of ~205 nm, separated into twin/matrix lamellar structures by the slanted TBs. In the base of the wire, there is a transition region with small irregular shaped grains. The microstructure of this layer may be affected by the properties of the seed layer, as well as the pulsed vs. DC voltage applied during deposition. After the transition layer, nearly all the Cu grains exhibited columnar structure with TBs within them. On the other hand, the wires prepared by DC-ED were consisted of small irregular shaped grains uniformly distributed across the wire with an average grain size of ~180 nm.

TEM images validated the FIB observations. The dark field TEM image of the PED wire highlights few of the grains in a selected diffraction spot (Figure 3.8B), and reveals the columnar-grained structure consistent with the FIB observation. Most of the grains contain parallel TBs. The high magnification image of a single grain at the top right corner of the wire and the selected area electron diffraction (SAED) pattern (Figure 3.8C and D) confirmed the nt-structure. The difference between the microstructure of the wire printed by DC-ED and PED shows that the nanotwins are formed due to the occurrence of the OFF-time during the 3D printing process. It seems that the twins are propagated through the grains with an irregular spacing. A cross-section TEM image of the entire DC-ED wire is presented in Figure 3.8F. The wire consists of small grains with nanoscale

size, uniformly scattered along the length. The higher magnification bright field TEM image and the SAED pattern indicate the nc structure (Figure 3.8G and H).

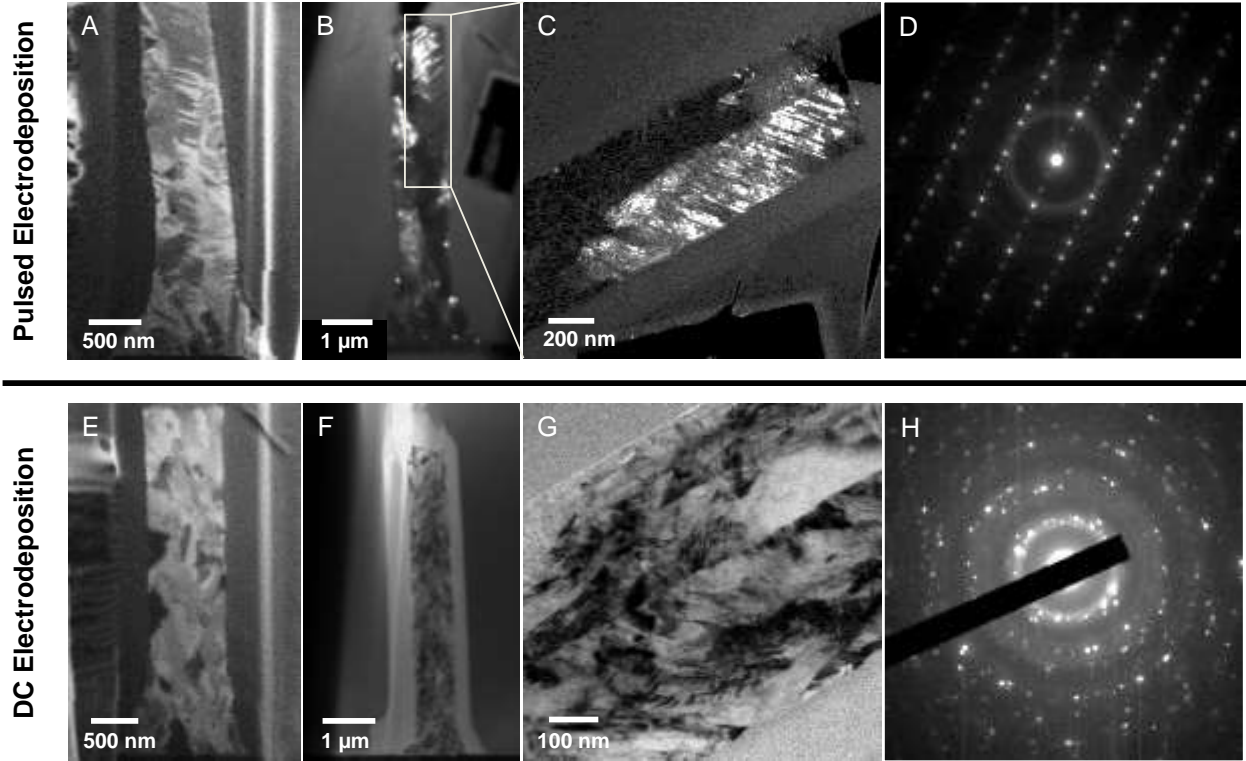


Figure 3.8. Microstructure of wires printed using (A)-(D) PED and (E)-(H) DC-ED. (A) The cross-section FIB ion channeling contrast image, and (B) TEM dark-field image of the wire printed by PED. (C) Zoomed-in image of the area enclosed in box in B shows a typical grain with (D) the corresponding diffraction pattern, which reveals the nanocrystalline nanotwinned (nc-nt) structure with columnar shaped grains. (E) The cross-section FIB ion channeling contrast image, and (F) and (G) TEM bright field images of the wire printed by DC-ED. (H) The diffraction pattern confirms nanocrystalline (nc) structure.

Figure 3.9 presents a high resolution TEM (HRTEM) image of two TBs (shown by the dashed lines) along [110] orientation, in the PED printed wires. The fast Fourier transformation (FFT) of the selected areas are shown in the insets. The FFT of TB (iii) is consistent with the double-spot pattern of twinning. The patterns on the two sides of the TB (i, ii) show mirror

symmetry. According to the FFT, TBs are formed in (111) plane. The texture of the printed wire is similar to the previous bulk electrodeposited films <sup>48</sup>.

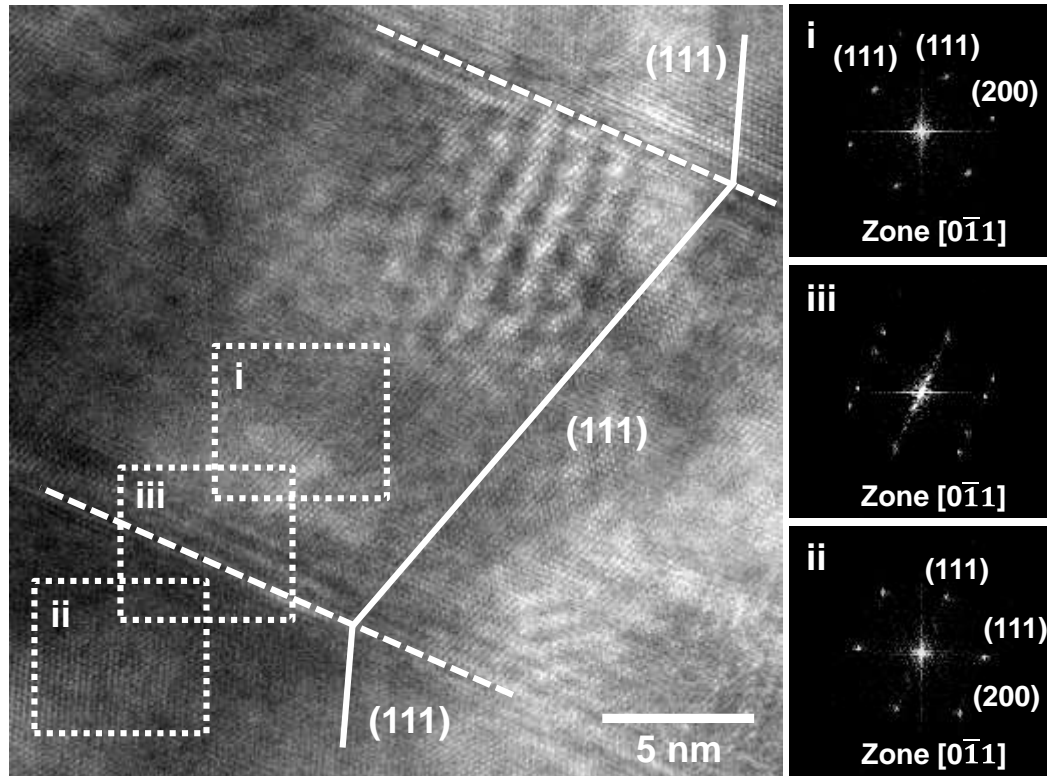


Figure 3.9. HRTEM image of typical coherent TB in the PED wire. The TBs are shown by the dashed line. Insets are FFT patterns of (i, ii) two mirrored sides of the TB, and (iii) the TB, respectively.

In addition, Figure 3.10 shows a high resolution TEM (HRTEM) image of another twin boundary (TB) in the printed nanotwinned (nt) wire. The d-spacing of the lattice structure on both sides of the TB was characterized through analysis of fast Fourier transform (FFT) of the HRTEM image by DigitalMicrograph® software. According to the results, d-spacing at regions (i) and (ii) was 2.09 Å and 2.11 Å, respectively, which confirmed (111) planes parallel to the twins, as expected.

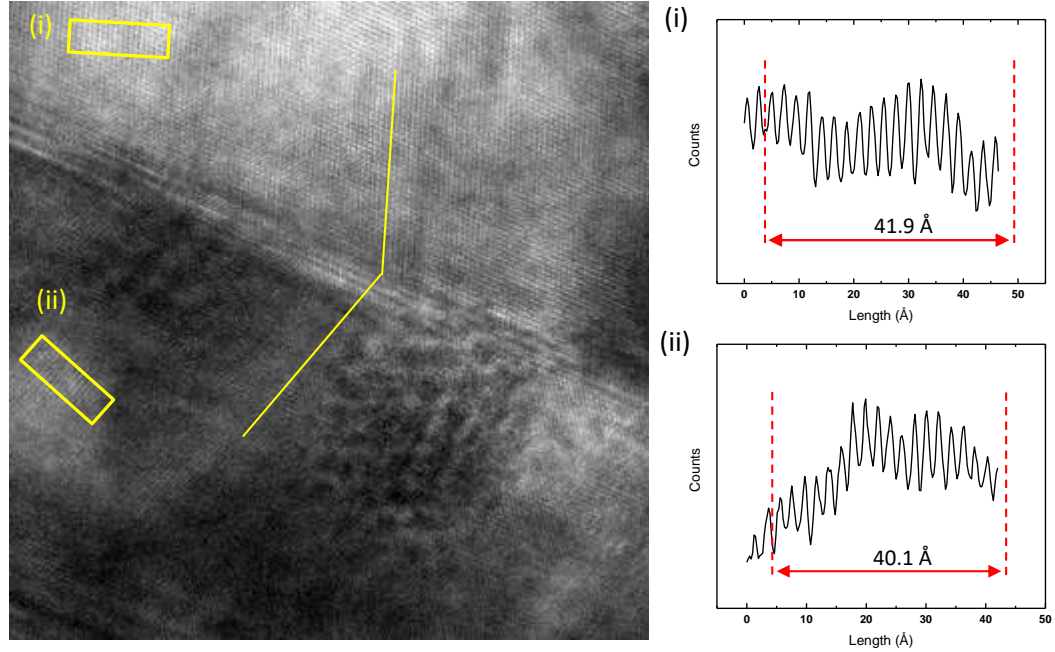


Figure 3.10. Lattice structure characterization using high resolution TEM image of a twin boundary. (i) Total d-spacing of 20 fringes along the specified region, which indicates d-spacing of 2.09 Å. (ii) Total d-spacing of 19 fringes along the specified region, which indicates d-spacing of 2.11 Å. The measured d-spacings at two regions show (111) planes on both sides of the twin boundary.

Figure 3.11B shows the FIB ion channeling contrast image of the cross-section of layer-by-layer printed structure presented in Figure 3.5E. As expected the microstructure contains aligned twins within the grains. Interestingly, there is no noticeable interlayer in the twinned layer-by-layer deposited structure. Although the grains were deposited in multiple steps (with time interval of 5 minutes between each steps as the nozzle returned to the same location) no discontinuity was observed within the grain. In each layer the grains mostly continued growing, and no new grains were formed for each layer. The absence of inter-layer interface can be important to enhance the mechanical and electrical properties of the 3D printed structures.

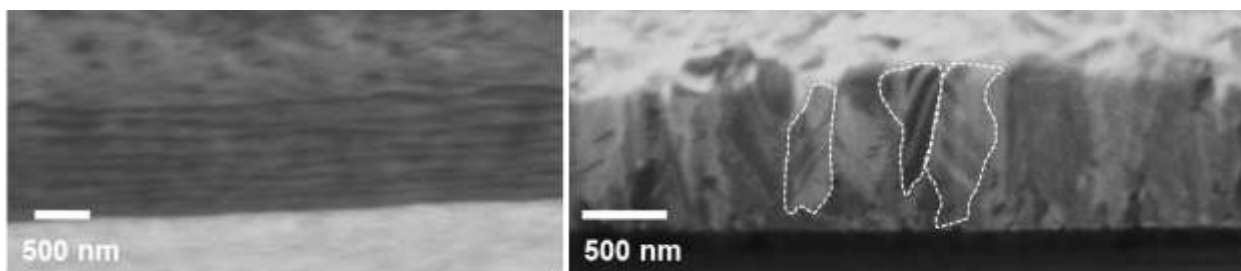


Figure 3.11. (Left) SEM image of zoomed-in view of the layer-by-layer deposited structure and (right) The FIB image of the cross-section showing that each layer is deposited on the previous layer, with no noticeable interlayer.

### 3.3.3 Mechanical characterization

Micro-compression experiments were performed on micro-pillars with two different internal microstructures described in Figure 3.8. The experiments were performed *in situ* SEM as described in Figure 3.2. Five samples were tested for each microstructure. The dimension, deposition rate, and current efficiency of each micro-pillar is presented in Table 3.2. Figure 3.12A and B show true stress-strain responses of the PED and DC-ED micro-pillars, respectively. The true stress-strain was calculated with the assumption of constant volume of the material during deformation. Both DC and pulse electrodeposited micro-pillars exhibited near-perfect elastoplastic behavior, with a smooth flow stress. This behavior is consistent with previous studies<sup>55, 56</sup>. No hardening was observed in the stress-strain responses of both microstructure types, while the PED material showed a slight decrease in flow stress by increasing strain.

The flow stress at 10% strain is shown in Figure 3.12C. The flow stress at 10% strain was chosen because of an unclear yield point in such small samples. Results showed a significant difference between the flow stresses of DC-ED vs. PED micro-pillars. The flow stress of the PED micro-pillars ranged from 932 MPa to 988 MPa, with an average of  $962 \pm 26$  MPa. The flow stress of the DC-ED micro-pillars ranged from 598 MPa to 699 MPa, with an average of  $656 \pm 46$  MPa.

The results indicate a significant influence of the introduction of PED on the mechanical response. Nt-PED Cu showed ~47% higher flow stress compared to the Cu deposited by DC-ED process. The mechanical properties reinforce the FIB and TEM results that revealed the existence of TBs in the PED wires, and validate the advantageous effect of the addition of the TBs in the grains of the material.

Generally, the mechanical behavior of nc and nt-nc pillars in compression is thought to be similar. In both cases, dislocations first originate at the grain boundary triple junctions due to the higher stress concentration.<sup>57</sup> In the nc pillars (DC-ED), the partial dislocations are only blocked by the grain boundaries, which leaves the entire grains with the stacking faults. But in the nt-nc pillars (PED), TBs similarly block the intersecting slip planes, and the dislocations can only propagate parallel to TBs. Therefore, the dislocations form pile-ups at the boundaries, and the strength of the specimen increases with decreasing the twin thickness, following the Hall-Petch relation (which has been reported that for nt-Cu with the twin thickness of larger than 15 nm, strength and twin thickness exhibit inverse relationship<sup>40</sup>). This mechanism results in a much lower density of stacking faults within the grains of nt-nc samples, and enhances the strength of the Cu pillars<sup>57</sup>. This indicates the favorable influence of insertion of the TBs within the grains in PED.

Figure 3.12D shows comparison of the strength of the 3D-printed Cu micro-pillars to the Cu micro/nanopillars fabricated by different methods reported in the literature.<sup>55, 58-60</sup> As expected, the ultrafine grained (ufg) Cu specimens (mean grain size larger than 1  $\mu\text{m}$ ) exhibited the smallest strength. The strength of pure nc specimens is increased by more than a factor of two compared to ufg samples. Interestingly, both nc and nc-nt micro-pillars printed by L-PED process showed

higher strength in comparison with similar pillars fabricated with electrodeposition in the pre-designed template.<sup>55</sup>

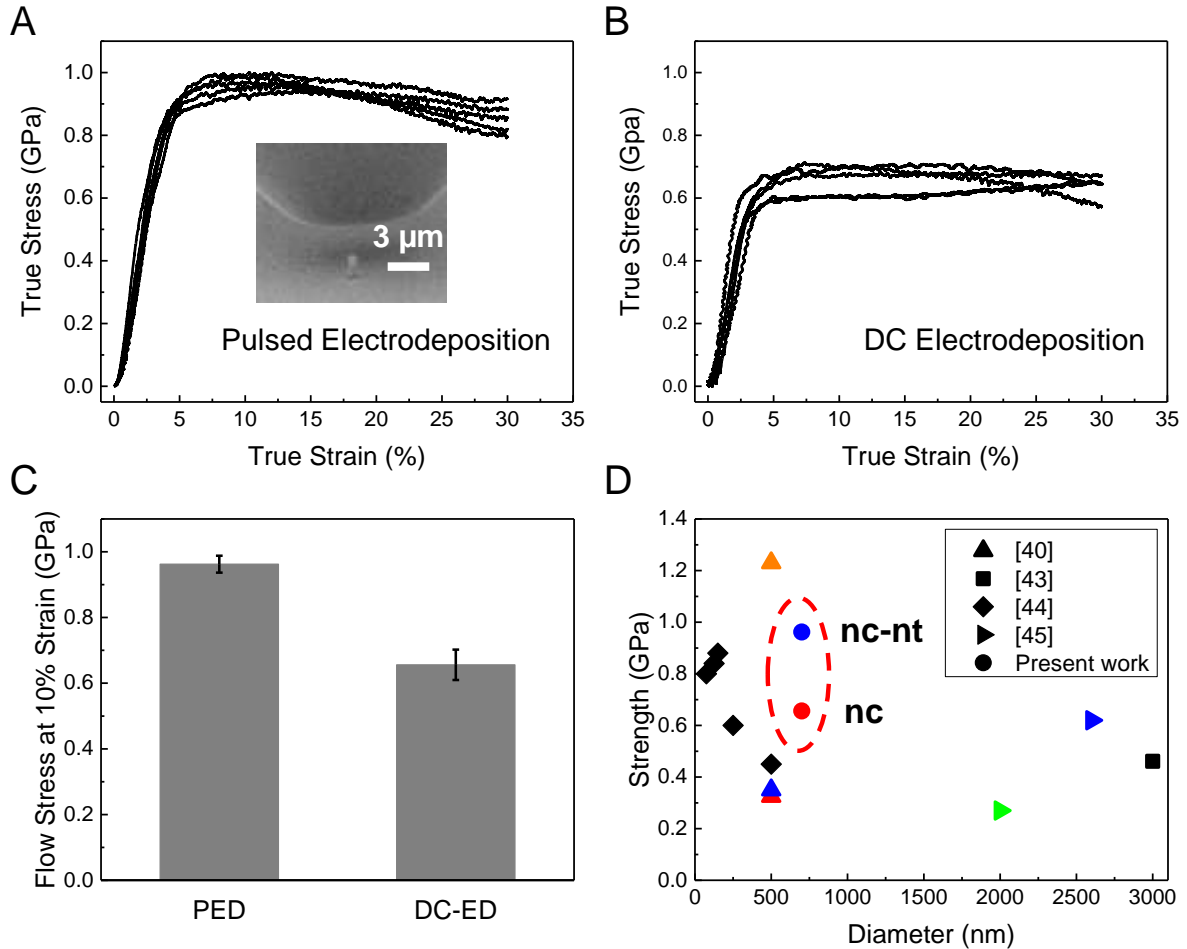


Figure 3.12. Micro-compression stress and strain responses of 3D-printed Cu micro-pillars by (A) PED with nc-nt microstructure, and (B) DC-ED with nc microstructure. The inset in A is an SEM image of the micro-compression experiment. (C) Comparison of flow stress of each microstructure at 10% strain. (D) Strength of the 3D-printed micro-pillars compared with similar nanowires fabricated with different methods (green = ultrafine grain, black = single crystal, red = nanocrystalline, blue = nanocrystalline nanotwinned, and orange = single crystal nanotwinned). Note that the color code is for each specific microstructure. The shapes in the legend of the figure refer to the specific reference.

The presence of grain boundary triple junctions is expected to make both nc and nc-nt nanopillars weaker than the single crystalline (sc) ones,<sup>57</sup> but the current 3D printed nc-nt materials showed higher yield strength compared to the sc nanopillars. In the sc specimens, the surface

defects can serve as effective stress concentrators, and it is where the first partial dislocation nucleates.<sup>57</sup> Hence, the strength of sc specimens are highly sensitive to the surface condition, and this may explain the lower strength of the sc nanopillars compared to the 3D printed nc-nt ones. Experimental and molecular dynamics (MD) simulation results have revealed a Hall-Petch type relation between the strength and the twin thickness in the nanowire.<sup>44</sup> The tensile behavior of sc-Cu nanopillars with different diameters and twin spacing revealed that the TBs alone marginally enhance the plasticity of samples, and the combination of TBs and grain boundaries is more important to obtain nanopillars with high ductility.<sup>42</sup>

The mechanical characterization was performed on the layer-by-layer nanotwinned Cu structure using in situ SEM nanoindentation system (Figure 3.13A). Figure 3.14A presents a typical load vs. indentation depth response obtained from the nanotwinned copper sample. The calculated ratio of the final indentation depth to the maximum indentation depth ( $h_f/h_{max} = 0.92$ ) showed the existence of pile-up.<sup>61</sup> The AFM topography image of the indentation footprints and the line-scan confirmed the pile-up (Figure 3.13C and D). Once pile-up happens, the actual contact area between the indenter tip and the sample is larger than the predicted value by the Oliver-Phar method,<sup>62</sup> and the hardness and the modulus are overestimated. Hence, the true contact area were measured using the AFM images of indentation footprints in order to calculate the true hardness and modulus. The average elastic modulus of  $128.2 \pm 10.9$  GPa was achieved for the samples (Figure 3.14B). The elastic modulus for bulk Cu is  $\sim 117$  GPa. Also, the average calculated hardness of the samples was  $2.0 \pm 0.19$  GPa, which is in good agreement with the previous stated values on nt-Cu (Figure 3.14C).<sup>63-66</sup>

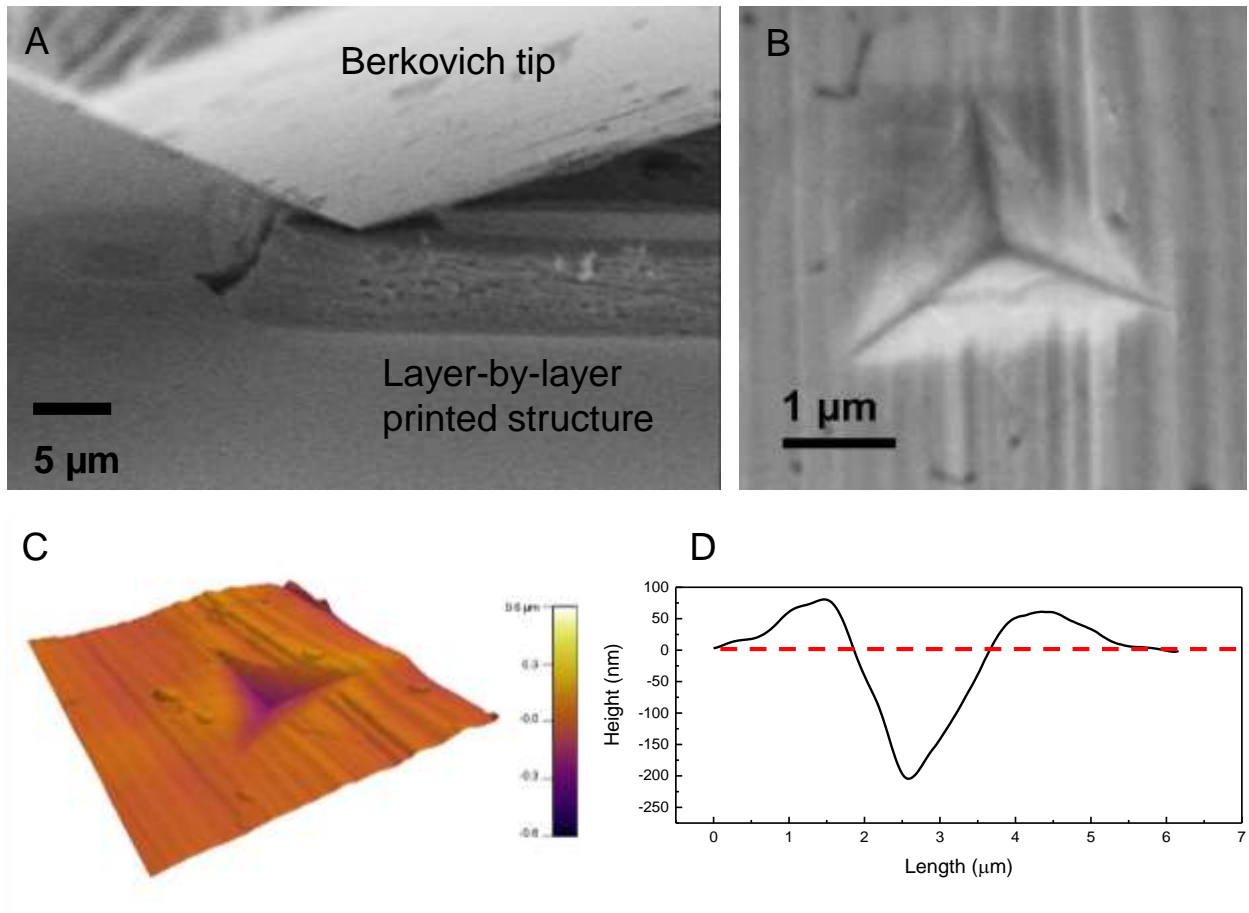


Figure 3.13. (A) In situ SEM nanoindentation on the L-PED printed layer-by-layer nt-Cu sample. (B) SEM image of an indentation footprint. (C) An AFM topography image of one of the indentation footprints. (D) Line-scan obtained from the indentation site, which shows pile-up in the indentation (Reprinted from Ref <sup>54</sup>, with the permission of John Wiley and Sons).

### 3.4 Conclusion

In conclusion, 3D printing of freestanding nt-Cu wires and micro-pillars using an ambient environment solution-based process based L-PED was demonstrated. The results showed that high quality Cu can be printed in 3D geometries with nanocrystalline-nanotwinned microstructure (nc-nt). The printed nc-nt Cu exhibited a remarkable yield strength of over 960 MPa, which is 47% larger than the yield strength of nc-Cu printed using the same process, under DC electrodeposition. The demonstrated process can be extended to include control over density of twins and their

orientation, and the grains size and orientation by adjusting deposition parameters in both DC-ED and PED techniques.

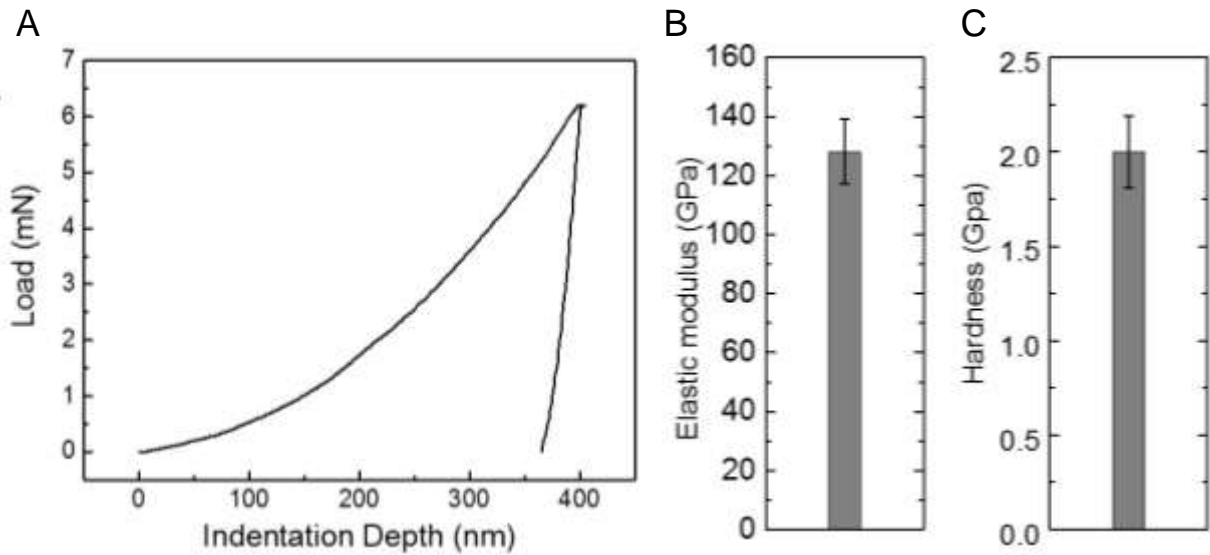


Figure 3.14. (A) Load-indentation depth plot obtained from nanoindentation on the nanotwinned copper sample. (B) and (C) Graph show elastic modulus and hardness of the printed Cu, respectively (Reprinted from Ref <sup>54</sup>, with the permission of John Wiley and Sons).

Also, the size of printed structures can be controlled by adjusting parameters such as the aperture diameter of the micropipette nozzle and the withdrawal speed of the nozzle.<sup>31</sup> For a given nozzle diameter, increasing the withdrawal speed of the nozzle will result in finer diameter wires, since the meniscus bridge is stretchable within a stable range. On the other hand, the withdrawal speed/deposition rate of the wire depends on the applied potential, electrolyte concentration, and environmental humidity. Based on the multi-physics model and experimental observation, wires can be printed in the range of 0.5 to 0.9 times of the nozzle diameter. This capability will be attractive for various applications in nanotechnology, in particular for 3D electronics and sensors. Additionally, this method may be extended to other materials and alloys that can be electrodeposited.

## CHAPTER 4

### TOWARD CONTROL OF MICROSTRUCTURE IN MICROSCALE ADDITIVE MANUFACTURING OF COPPER USING LOCALIZED ELECTRODEPOSITION

#### 4.1 Introduction

The control of microstructure in 3D-printed metals is one of the most formidable challenges facing microscale additive manufacturing ( $\mu$ -AM) of these materials.<sup>47</sup> The main focus of  $\mu$ -AM processes for metals has been on achieving small scale structures with complex geometries.<sup>1, 17, 67</sup> However, for functional applications (such as electronics, sensors, photonic, among others) with desirable properties, it is necessary to gain control over of the microstructure, and hence mechanical and electrical properties. The mechanical properties (such as yield stress, flow stress and strength) of metals and alloys are predominantly determined by their microstructure including the grain size, dislocation density and dislocation mobility, and the solid solution content. Electrical properties are often affected by impurities, pores and defects in the material. Currently, there is very limited information on the control of microstructure in  $\mu$ -AM of metals.

Several distinct physical and chemical  $\mu$ -AM processes for metals are currently available. They include direct ink writing (DIW), electrohydrodynamic printing (EHD), local electrophoretic deposition, laser-induced forward transfer (LIFT), meniscus-confined electroplating, electroplating of locally dispensed ions in liquid, laser-induced photoreduction, and traditional focused electron/ion beam induced deposition processes. Principle of operation, achievable geometry and feature size, speed of printing, compatible materials, and possible applications of

---

\*Reproduced with permission from Soheil Daryadel, Ali Behroozfar, and Majid Minary-Jolandan, Toward Control of Microstructure in Microscale Additive Manufacturing of Copper Using Localized Electrodeposition, Advanced Engineering Materials, in press. Copyright (2018) Wiley

these processes have been discussed in a recent review article.<sup>47</sup> DIW and EHD often require post-processing to remove the organic matrix from the printed composite. Heat treatment, often as high as 400-500 °C decomposes the polymer matrix, and results in densification and grain growth of the metallic phase. Pronounced porosity can also result from the heat treatment. Removal of the polymer matrix may enhance the electrical conductivity of the material, however, the grain growth during annealing is not desirable for mechanical properties. The microstructure in LIFT and reduction based approaches is often crystalline, and the microstructure can be potentially controlled through process parameters *in situ*.

The localized pulsed electrodeposition (L-PED) is an electrochemical-based microscale additive manufacturing process ( $\mu$ -AM) for metals and alloys.<sup>54, 68</sup> In this process, electrodeposition is confined to a small zone at the tip of a nozzle filled with the metal's liquid electrolyte (Figure 4.1A). When the nozzle approaches to the substrate, a meniscus (liquid bridge) is formed between the tip of the nozzle and the conductive substrate. This electrolyte meniscus functions as a confined electrochemical bath (Figure 4.1B). When a pulsed electric potential is applied (Figure 4.1D) between an electrode inserted from the back of the nozzle (the counter electrode, or anode) and the substrate (the working electrode, or cathode), the metal ions are deposited at the growth front within the meniscus area on the cathode surface.<sup>69, 70</sup>

In the L-PED process, the applied potential/current is interchanged repeatedly between ON and OFF with the time periods of  $T_{ON}$  and  $T_{OFF}$ , respectively (Figure 4.1D). Therefore, during short time interval of ON potential, a very high current density and subsequently high deposition rate is achieved, while in the OFF-time the consumed ions are recovered, and higher concentration of ions is provided on the cathode surface for the subsequent ON-time. In pulsed electrodeposition

(PED) the ON-time is often on the order of milliseconds, and the OFF-time is on the order of seconds. High purity metallic structures can be printed in desired 3D geometries through precise and controlled motion of the relative position of the nozzle and the substrate. L-PED is capable of printing different geometries such as free-standing wires, micro-pillars ( $\mu$ -pillars), and layer-by-layer structures (Figure 4.1E-H).<sup>54, 68</sup>

The L-PED process can be used to produce unique microstructures that are not obtainable by conventional direct current electrodeposition (DC-ED). The meniscus-confined DC electrodeposition was demonstrated in 2010 for 3D printing of microscale copper (Cu) wire bonds.<sup>1</sup> The metal printed by DC-ED is nanocrystalline.<sup>14</sup> Recently, we reported that by application of pulsed current/voltage, high purity and void-free nanotwinned Cu can 3D-printed without any additives.<sup>54, 68</sup> Nanotwinned metals are ultrafine-grained or fine-grained metals with grains that contain a high density of layered nanoscale twins divided by coherent twin boundaries (TBs). Nanotwinned metals have an unprecedented combination of ultrahigh strength, high ductility, and high electrical conductivity,<sup>39, 40</sup> and are hence attractive for applications requiring high electrical conductivity and high strength and ductility such as in flexible electronics, sensors, solder bumps, interconnects and wire bonds.

Bulk PED has been extensively investigated in the literature.<sup>53, 71-74</sup> Generally, it is known that the microstructure of the deposited metal is dependent on the deposition parameters and conditions, such as stirring, bath additives, temperature, and the pH.<sup>75</sup> PED facilitates more control over the microstructure compared to the conventional DC method because of the inclusion of ON- and OFF-time. The mechanisms for control of the grain texture and twin densities are reported in the literature by changing the peak current density and duty cycle.<sup>71-74</sup> However, L-PED is

inherently distinct from the bulk PED. Figure 4.1B and C show the side-by-side comparison of the L-PED with the conventional bulk electrodeposition. In conventional (pulsed) electrodeposition, the anode and cathode are immersed into an electrolyte bath. Hence, the entire cathode surface is exposed to the electrolyte and pulsed current. In L-PED only the area under the meniscus (liquid bridge) is exposed to the electrolyte. Considering the small size of the cathode area (radius of smaller than 25  $\mu\text{m}$ ) in this process, we can assume the electrode in the system as an ultramicroelectrode (UME). In UMEs, as the dimension of the electrode is comparable to the thickness of the double layer.<sup>38</sup> The small size of the cathode electrode generates small overall passing currents, and consequently a very low ohmic drop, which allows using simple two-electrode cell instead of the conventional three-electrode.

The short pulses applied to the anode by the potentiostat during  $T_{ON}$  drives the ions and hence the electrolyte toward the cathode, which generates a convective flow in the narrow nozzle-tip and within the meniscus.<sup>69, 70</sup> High concentration of metal ions in the meniscus area during  $T_{ON}$  results in back diffusion away from the meniscus opposite to the convective flow direction. During  $T_{OFF}$ , ions flow back toward the meniscus to compensate for the depleted ions. Additionally, water evaporates very fast from the meniscus, since the surface area to volume ratio ( $A/V$ ) for small liquid meniscus is large. Fast evaporation of water from the meniscus increases the concentration of metal ions in the meniscus surface, which in turn results in additional convective flow toward the meniscus area. One important advantage of evaporation in L-PED process is that the mass transport to the electrode is high, even in the absence of regular convection process used in bulk PED, such as stirring. This phenomenon results in a different range of process parameters compared to the bulk PED. Another consequence of high evaporation rate from the meniscus

surface is higher ionic concentration at the meniscus edge, which causes non-uniform current density across the cathode surface. However, the controlled relative humidity and long OFF-time period in the L-PED process allows the meniscus to achieve uniform ionic distribution across the cathode surface.

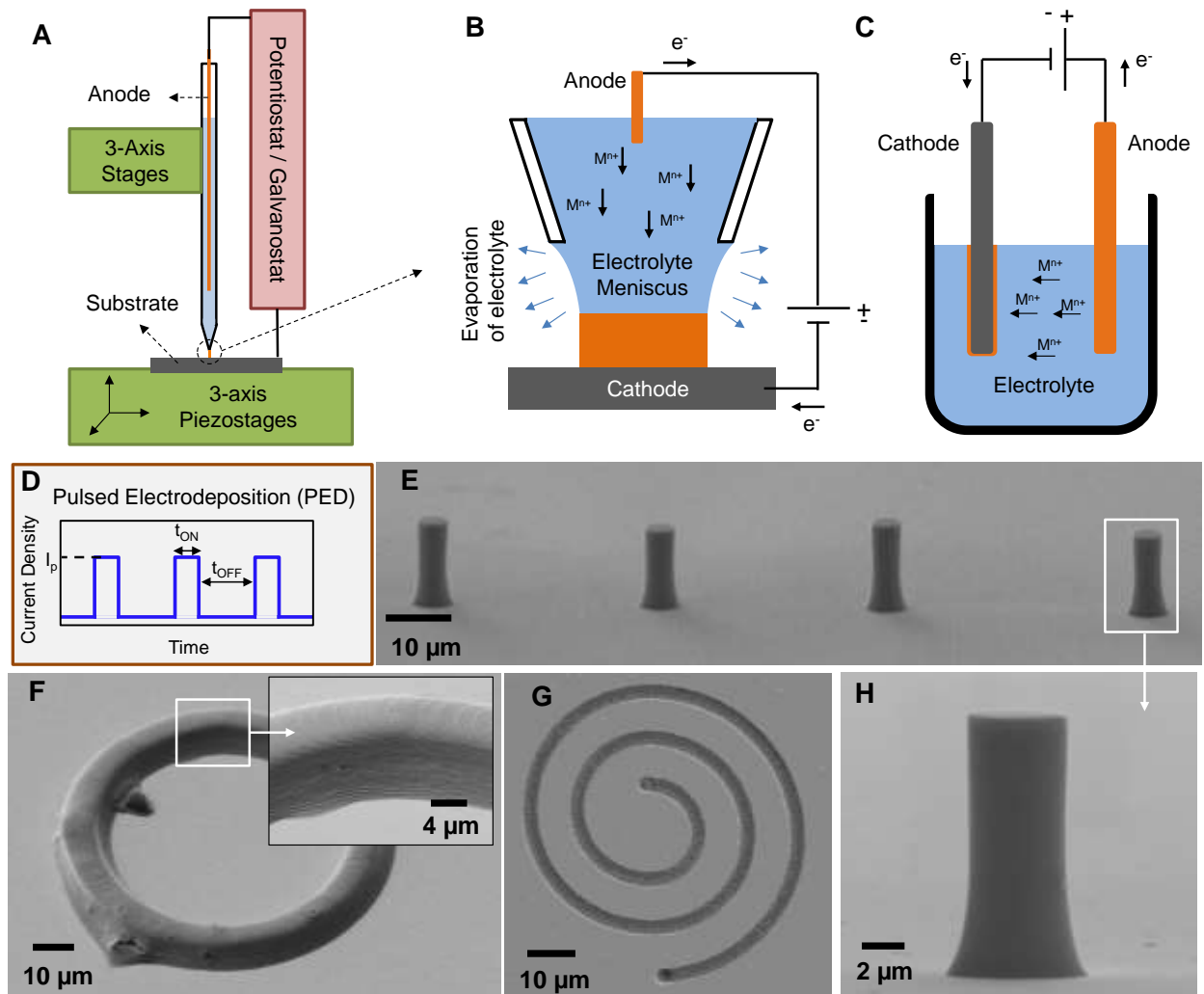


Figure 4.1. (A) The schematic view of L-PED 3D printing process. Side-by-side comparison of (B) the L-PED printing process and (C) the bulk electroplating. (D) Pulsed current electrodeposition (PED) with an arbitrary duty cycle. SEM images of (E) an array of 3D-printed  $\mu$ -pillars for micro-compression experiment (printing time for each pillar  $\sim 12$  min), (F) a 40-layer structure printed by layer-by-layer L-PED (printing time  $\sim 150$  min), (G) a spiral pattern (printing

time = ~15 min), and (H) a close-up view of a  $\mu$ -pillar for micro-compression and microstructure characterization.

Considering these differences between the bulk PED and L-PED, kinetics of electrodeposition, flow of electrolyte, concentration of ions, distribution of electric potential, and the current density, which ultimately determine the average deposition rate may be different between the electrodeposition in a confined nozzle vs. conventional electrodeposition in a bath. In this section, the effect of various process parameters on the microstructure and mechanical properties of the 3D printed metal using L-PED is characterized.

## 4.2 Materials and methods

For printing Cu  $\mu$ -pillars, glass micropipettes nozzle was filled with the electrolyte solution of CuSO<sub>4</sub> (100 mM) and H<sub>2</sub>SO<sub>4</sub> (1 M). Additionally, the cell consists of a conductive substrate (gold-coated silicon) as the working electrode, and a copper wire inserted from back of the nozzle as the counter electrode. During the process, the humidity around the nozzle was controlled by a remote hygrometer, and 3D printing was conducted at a constant relative humidity of ~65%.

It is noteworthy that there are differences in the chosen range of parameters in the L-PED process compared to the bulk PED. For instance, while there is no lower limit in the deposition rate in PED, due to the essential fact that in L-PED process the deposition rate should be synced with the steady speed of the nozzle.<sup>68</sup> Therefore, parameters should be chosen in a way that the slowest deposition rate meets the lower limit speed of the positioning stages. This limit in our experiment was 1 nm/s. Additionally, there is an upper limit for the applied peak current density to avoid clogging of the nozzle due to fast and dendritic deposition of material.

The microstructure of the 3D-printed micro-pillars were characterized using scanning electron microscopy (SEM), energy dispersive X-ray spectroscopy (EDS), and high-resolution focused ion beam (FIB). The overall geometry, diameter, and height of the micro-pillars were observed under SEM (Zeiss Supra 40) to examine if they were suitable for micro-compression experiment. Elemental analysis was performed using the same system equipped with an EDS system using 18 kV electron beam. To examine the grain size and twin boundary presence, the cross-section of the micro-pillars was observed using high-resolution focused ion beam (FIB) imaging (FEI Nova Nanolab 200). The cross-section of the micro-pillars was milled at a final acceleration voltage of 30 keV and current of 10 pA, followed by imaging using the same parameters.

Mechanical properties of the 3D-printed  $\mu$ -pillars were obtained using micro-compression experiments *in situ* SEM by a nanoindentation system (NanoFlip, Nanomechanics). Micro-pillars were compressed using a 50  $\mu\text{m}$  diameter flat punch conductive diamond as the compression anvil. Three samples were tested for each deposition parameter that was examined for mechanical properties. The diameter range of the micro-pillars was  $\sim 5.10 \pm 0.7 \mu\text{m}$ . To minimize the effects of buckling and the other artifacts, the length-to-diameter aspect ratio of the  $\mu$ -pillars was kept at  $\sim 2:1$ . For accurate micro-compression experiment, the top surface of the micro-pillars were milled with FIB to completely flatten their top surface, where the tip of the flat punch touches the printed metal. Fine milling was performed at an acceleration voltage of 30 keV and current of 10 pA. All experiments were run under displacement-control mode at a constant displacement rate in order to achieve the constant strain rate of  $1 \times 10^{-3} \text{ s}^{-1}$  ( $\dot{\epsilon} = \dot{L}/L$ ). The stress-strain response was calculated

based on the obtained load-displacement and geometry of each micro-pillar. Real-time deformation video and the mechanical data were recorded during the experiments.

### 4.3 Results and discussion

For this study, several tens of copper (Cu) micro-pillars ( $\mu$ -pillars) with a diameter of  $\sim 5$   $\mu\text{m}$  were directly 3D-printed using the L-PED process with different processing parameters. Similar  $\mu$ -pillars are often fabricated using the focused ion beam (FIB) milling from thin films of the material of interest. The L-PED process enables direct printing of the  $\mu$ -pillars, which facilitates characterization of both microstructural and mechanical properties. Details of the printing process is given in the materials and method section. Figure 4.1E shows a SEM image of an array of four  $\mu$ -pillars with diameter of  $\sim 5.2$   $\mu\text{m}$  printed for the *in situ* SEM micro-compression experiment. The  $\mu$ -pillars have uniform geometry throughout the length with a strong adhesion to the substrate, which is important for quantitative characterization of mechanical properties.

The energy dispersive X-ray spectroscopy (EDS) spectra acquired from a  $\mu$ -pillar (Figure 4.1H) is shown in Figure 4.2A. The EDS data show that the printed material is high purity Cu without significant presence of impurities. Although the printing process is carried out in room environment, only small amount of oxygen is present on the surface of the substrate and  $\mu$ -pillars. Note that the gold (Au), chromium (Cr), and silicon (Si) in the spectra originated from the substrate.

Three independent variables in PED include  $T_{ON}$ ,  $T_{OFF}$ , and the peak current density ( $I_P$ ), as shown in Figure 4.1D. The average current density ( $I_A$ ) in PED is defined as  $I_A = I_P \times \gamma$ , in which  $\gamma$  is the duty cycle,  $\gamma = T_{ON} / (T_{ON} + T_{OFF})$ . Often time, the average current density is used as the main process parameter in PED. Increasing the average current density results in increase in the

deposition rate. For growth of a  $\mu$ -pillar, it can be shown that the growth rate (which is equal to the withdrawal speed of the nozzle) is given by  $v = \frac{4iM}{nF\rho\pi D^2}$ , in which  $i$  is the applied current during deposition,  $M$  is the molar mass and  $\rho$  is the mass density of the deposited material,  $n$  is the number of electrons per ion involved in the deposition reaction,  $F$  is the Faraday constant, and  $D$  is the diameter of the  $\mu$ -pillar.<sup>1</sup> This relationship shows that the deposition rate is proportional to the average current density ( $\frac{4i}{\pi D^2}$ ).

Figure 4.2B shows the experimental deposition rate for the printed  $\mu$ -pillars by the L-PED process vs. the average current density. The data shows a linear trend between the deposition rate and the average current density. The solid line is the deposition rate calculated from the Faraday's law. The current efficiency (CE) of the L-PED process can be calculated as the ratio of the experimental deposition rate and the deposition rate calculated from the Faraday's law<sup>38</sup>. The obtained current efficiency of the L-PED process was calculated to be  $90 \pm 5\%$ , which implies minimum side reactions and “wasted” current in the process. The high CE also implies that the side reactions do not produce any significant impurities in the deposited metal, as also confirmed by the EDS data (Figure 4.2A).

The density of twins that are formed during the deposition process highly depends on the nucleation rate and the average deposition rate.<sup>40</sup> In the bulk PED, it has been shown that the systematic change of the average current density enables synthesizing nanotwinned Cu with different twin thickness.<sup>40</sup> The effect of average current density (hence the deposition rate) on the microstructure of the printed metal is examined by the L-PED process. Detailed deposition parameters for the  $\mu$ -pillars are presented in Table 4.1.

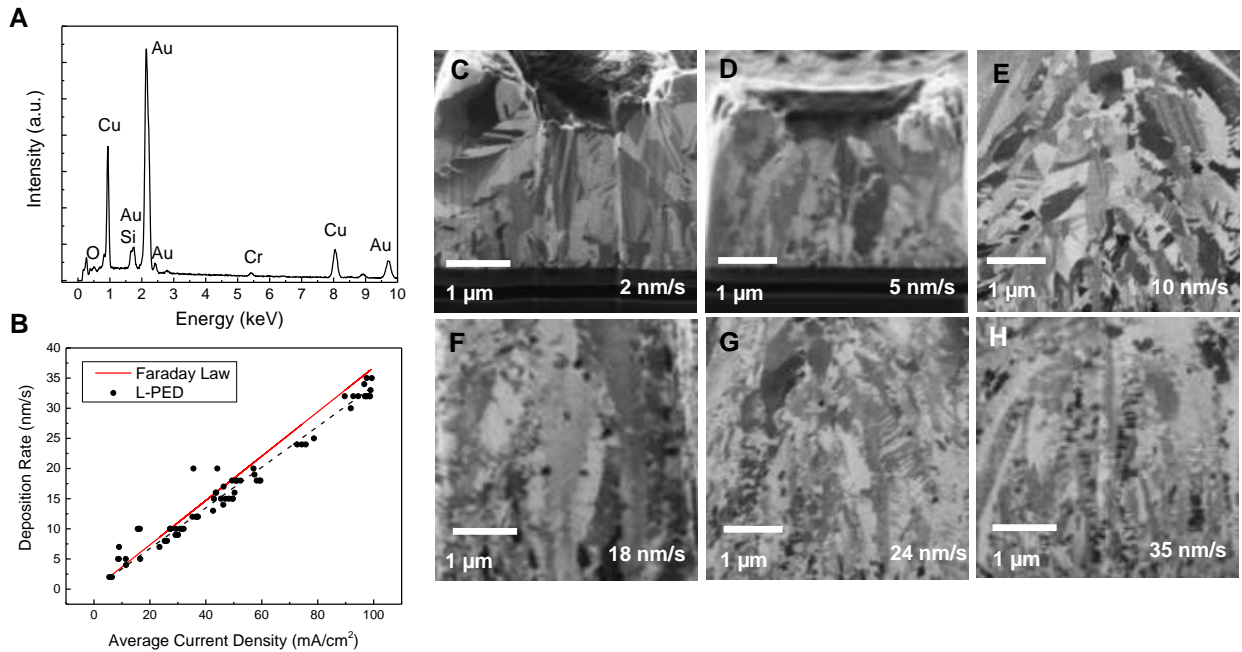


Figure 4.2. (A) The EDS spectra acquired from a printed  $\mu$ -pillar. No significant presence of impurities was observed in EDS data. (B) The experimental deposition rate for the printed  $\mu$ -pillars by the L-PED process vs. the average current density. The solid line is the deposition rate calculated from the Faradays law. The current efficiency of the L-PED process was calculated to be  $90 \pm 5\%$ . (C)-(H) The effect of the average current density (and deposition rate) on the microstructure of 3D-printed nanotwinned Cu  $\mu$ -pillars. The cross-section FIB ion channeling contrast image of  $\mu$ -pillars printed at different deposition rates reveal that increasing the deposition rate increases the density and alignment of the twin boundaries (TBs).

Figure 4.2C-H show the cross-section FIB ion channeling contrast images of six different  $\mu$ -pillars deposited at different average current densities, spanning from  $\sim 5 \text{ mA/cm}^2$  to  $\sim 100 \text{ mA/cm}^2$ . This range of average current density results in deposition rates spanning 2 nm/s to 35 nm/s. The results show that for this range of parameters, all the printed Cu  $\mu$ -pillars contain twin boundaries (TBs). By increasing the average current density and the average deposition rate, the density of the TBs increases, which results in refinement of the twin lamella thicknesses. Additionally, it is observed that for slower deposition rate, TBs are randomly ordinated within the

grains. As the deposition rate increases, the grains become more columnar and the TBs within the grains get more aligned perpendicular to the growth direction.

Table 4.1. The process parameters of the  $\mu$ -pillars printed using the L-PED process.

<b>Electrodeposition Mode</b>	<b>ON Time (s)</b>	<b>OFF Time (s)</b>	<b>Peak Current Density (A/cm<sup>2</sup>)</b>	<b>Average Current Density (mA/cm<sup>2</sup>)</b>	<b>Deposition Rate (nm/s)</b>	<b>Current Efficiency (%)</b>
L-PED	0.02	2	0.55	5.46	2	99
L-PED	0.02	4	2.28	11.37	5	94
L-PED	0.02	2	2.77	27.48	10	99
L-PED	0.02	4	6.98	34.73	12	94
L-PED	0.2	2	0.64	59.25	18	83
L-PED	0.02	2	7.34	72.68	24	90
L-PED	0.02	2	9.85	97.52	35	98

The average current density and accordingly the deposition rate in PED process can be engineered by adjusting different pulse parameters including the peak current density, ON-time, and OFF-time. The influence of each of the pulse parameters on the microstructure of the printed Cu is investigated (Figure 4.3). In electrodeposition process, after transfer and incorporation of the ions on the cathode surface, there are two competitive processes depending on the electrochemical parameters: building up of the existing crystals or growing new ones <sup>76</sup>. The increase in the peak current density favors the nucleation of new crystals rather than the building up the existing ones.  $\mu$ -pillars were deposited using pulsed currents with the same periodic  $T_{ON}/T_{OFF}$  ratio (20 ms/2 s) and different peak current densities. As can be observed in Figures 4.3A and B, increasing the peak current density from 2.77 A/cm<sup>2</sup> to 9.85 A/cm<sup>2</sup> (corresponding to the deposition rate of 10 nm/s and 35 nm/s, respectively) increased the twin density in the metal, and also decreased the grain size. The metal printed with smaller average current density exhibits randomly-shaped large grains

with few randomly-oriented TBs, while the metal printed with the higher peak current density shows smaller columnar-shaped grains with high density of aligned TBs.

The duty cycle is an important parameter in the L-PED process, which is a function of  $T_{ON}$  and  $T_{OFF}$ . In order to investigate the effect of the ON-time on the microstructure of the 3D-printed Cu,  $\mu$ -pillars were fabricated using approximately the same peak current density and OFF-time, with different ON-time. The deposition peak current density was kept at  $\sim 0.6 \text{ A/cm}^2$  and  $T_{OFF}$  was set to 2 s, while the  $T_{ON}$  was increased from 20 ms to 200 ms. Increase of the ON-time results in higher density of TBs, as can be observed in Figure 4.3C and D. This increase in the number of TBs is because of the increase in the average current density by nearly ten times ( $\sim 5.5 \text{ mA/cm}^2$  to  $\sim 59.2 \text{ mA/cm}^2$ ). Although there is no significant grain refinement, however, the grains are more aligned and with columnar shape. The columnar-shaped grains often tend to grow along the fast growth direction of the metal.<sup>44</sup>

One of the most important parameters in PED is the time interval between two pulses, or the OFF-time. Although no current is applied during the OFF-time, it is believed that this period is very active with respect to recrystallization of the deposited metal. It is believed that the TBs are formed during the growth interruption and stress relaxation during the OFF-time.<sup>49</sup> Figure 4.3E and F show two different  $\mu$ -pillars printed using approximately the same peak current density and ON-time, and different OFF-time duration. Increasing the OFF-time from 2 s to 4 s, decreased the average deposition rate from 24 nm/s to 12 nm/s, and the average current density from  $\sim 72.7 \text{ mA/cm}^2$  to  $\sim 34.7 \text{ mA/cm}^2$ . As a result, the density of the TBs in the printed metal decreased.

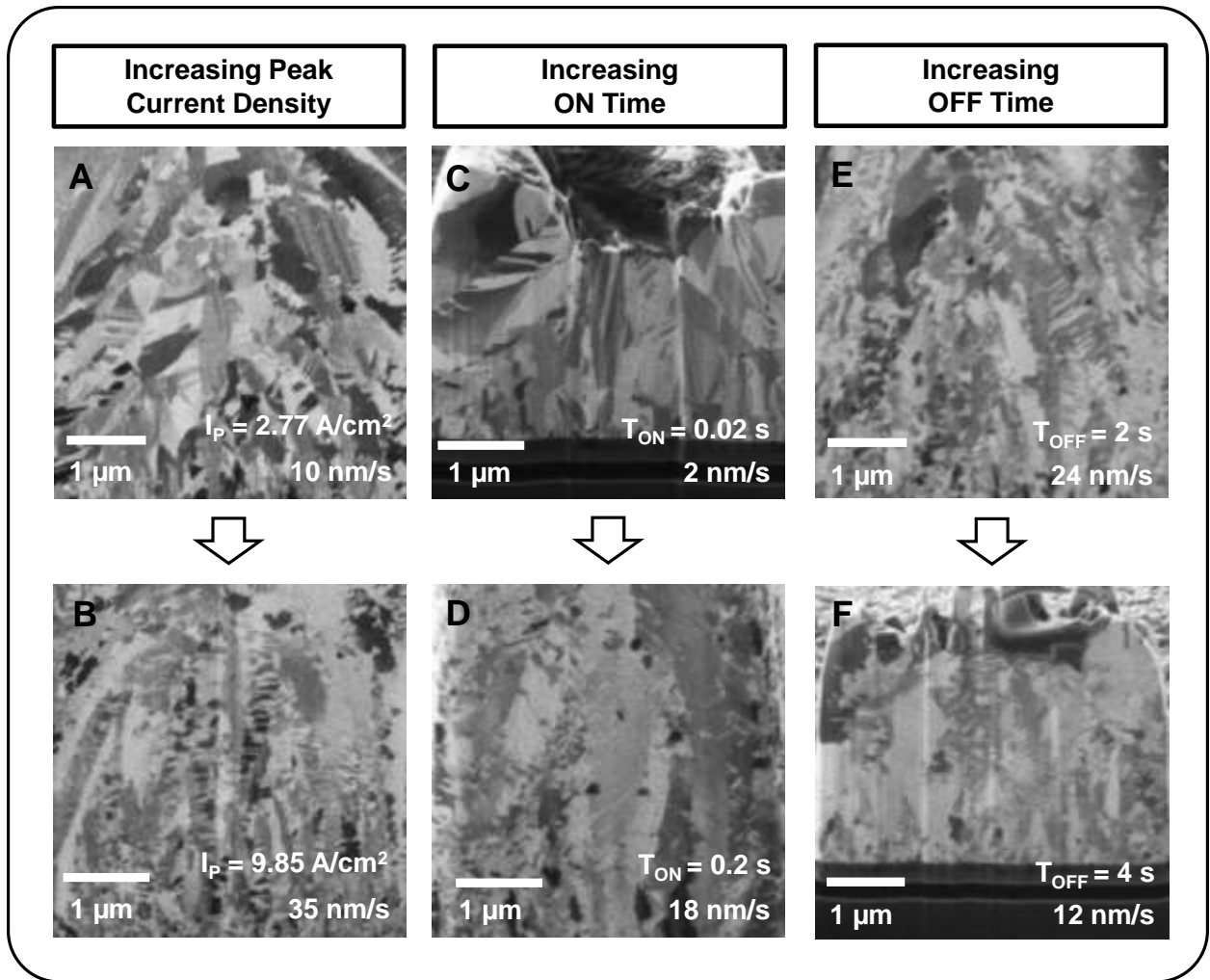


Figure 4.3. (A) and (B) The effect of the peak current density on microstructure of 3D-printed nanotwinned Cu: The cross-section FIB ion channeling contrast image show that increasing the peak current density increased the twin density and decreased the grain size. (C) and (D) increasing the ON-time results in higher density of twin boundaries. (E) and (F) increasing the OFF-time decreases the twin density and increases the grain size.

Additionally, the metal deposited using a longer  $T_{OFF}$  has significantly larger grains compared to the metal printed using shorter  $T_{OFF}$ . In the L-PED process, the current interruption causes desorption of impurities and inhibitors from the deposits and replenishment of the metal ions in the diffusion layer.<sup>52</sup> This phenomenon may produce opposite outcomes in terms of crystallization mechanism for different metals. For Cu deposition, increase in the OFF-time

stimulates grain growth rather than forming new grains, because in this system, the larger grains are thermodynamically more stable, and the system reaches the most stable state for longer  $T_{OFF}$ .<sup>52, 76</sup> As can be observed in the cross-section of the pillar in Figure 4.3F, increasing the  $T_{OFF}$  increased the grain size of the metal.

When  $T_{OFF} = 0$ , the process is essentially DC-ED. The effect of the processing parameters on the microstructure of the printed metal using DC-ED process is presented in Table 4.2. It is generally accepted that increasing the current density in electroplating of thin films promotes larger nucleation rate, which in turn results in grain refinement.<sup>77</sup> Based on the Faraday's equation,<sup>38</sup> the deposition rate of the metal in ED is proportional to the applied current density.  $\mu$ -pillars with the same nozzle diameter were deposited, by varying the applied current to obtain different current densities, and hence different deposition rates. Deposition rates from  $\sim 7$  nm/s to  $\sim 200$  nm/s for current density of  $\sim 20$  mA/cm<sup>2</sup> to  $\sim 550$  mA/cm<sup>2</sup> were obtained. The average CE (current efficiency) of the Cu deposition for the direct current electrodeposition (DC-ED,  $T_{OFF} = 0$ ) was calculated to be  $95 \pm 4$  % (Figure 4.4).

Applying a constant voltage (DC-ED) during the printing process results in a nanocrystalline microstructure with uniformly scattered grains.  $\mu$ -pillars with different parameters were printed using DC-ED to investigate the effect of the current density on the microstructure of the metal. It was observed that by changing the current density, the average grain size of the printed Cu can be controlled (Figure 4.5), which is in agreement with the bulk electrodeposition process.<sup>78</sup> Specifically, it was found that in the printing process, the larger current density results in reduction of the average grain size in the printed metal (Table 4.2 and Figure 4.5).

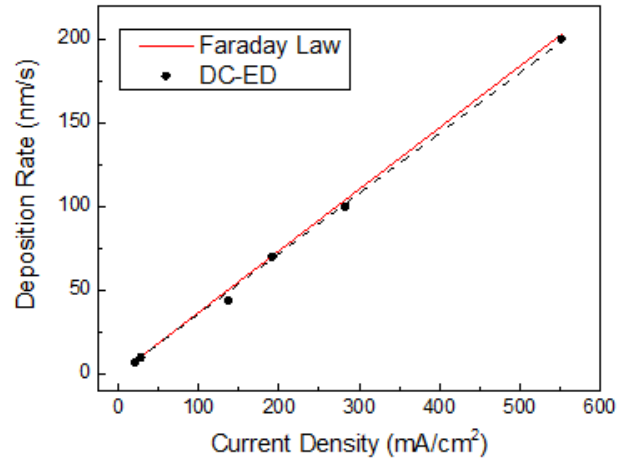


Figure 4.4. The Comparison of the obtained deposition rates of printed pillars by DC-ED process with the analytical growth rate calculated from the Faradays law. The obtained average current efficiency of DC-ED was calculated to be  $95 \pm 4 \%$ .

Table 4.2. The process parameters of the  $\mu$ -pillars printed using DC-ED technique.

Electrodeposition Mode	Current Density (mA/cm <sup>2</sup> )	Deposition Rate (nm/s)	Average Grain Size (nm)	Current Efficiency (%)
DC-ED	20	7	$307 \pm 47$	94
DC-ED	28	10	$263 \pm 53$	98
DC-ED	192	70	$174 \pm 52$	99
DC-ED	283	100	$121 \pm 18$	96
DC-ED	552	200	$114 \pm 14$	99

Figure 4.5A-C shows the cross-section FIB ion-channeling contrast images of selected  $\mu$ -pillars printed using current densities of 20 mA/cm<sup>2</sup>, 192 mA/cm<sup>2</sup>, and 283 mA/cm<sup>2</sup>, corresponding to deposition rates of 7 nm/s, 70 nm/s, and 100 nm/s. Clearly, the average grain size reduces by increasing the current density and deposition rate. The average grain size was estimated using intercept procedure by counting the number of grains in the FIB cross-section image

intercepted by sufficient number of straight lines widely separated. Quantitatively, the average grain size reduced from  $307 \pm 47$  nm to  $121 \pm 18$  nm for deposition rate of 7 nm/s to 100 nm/s.

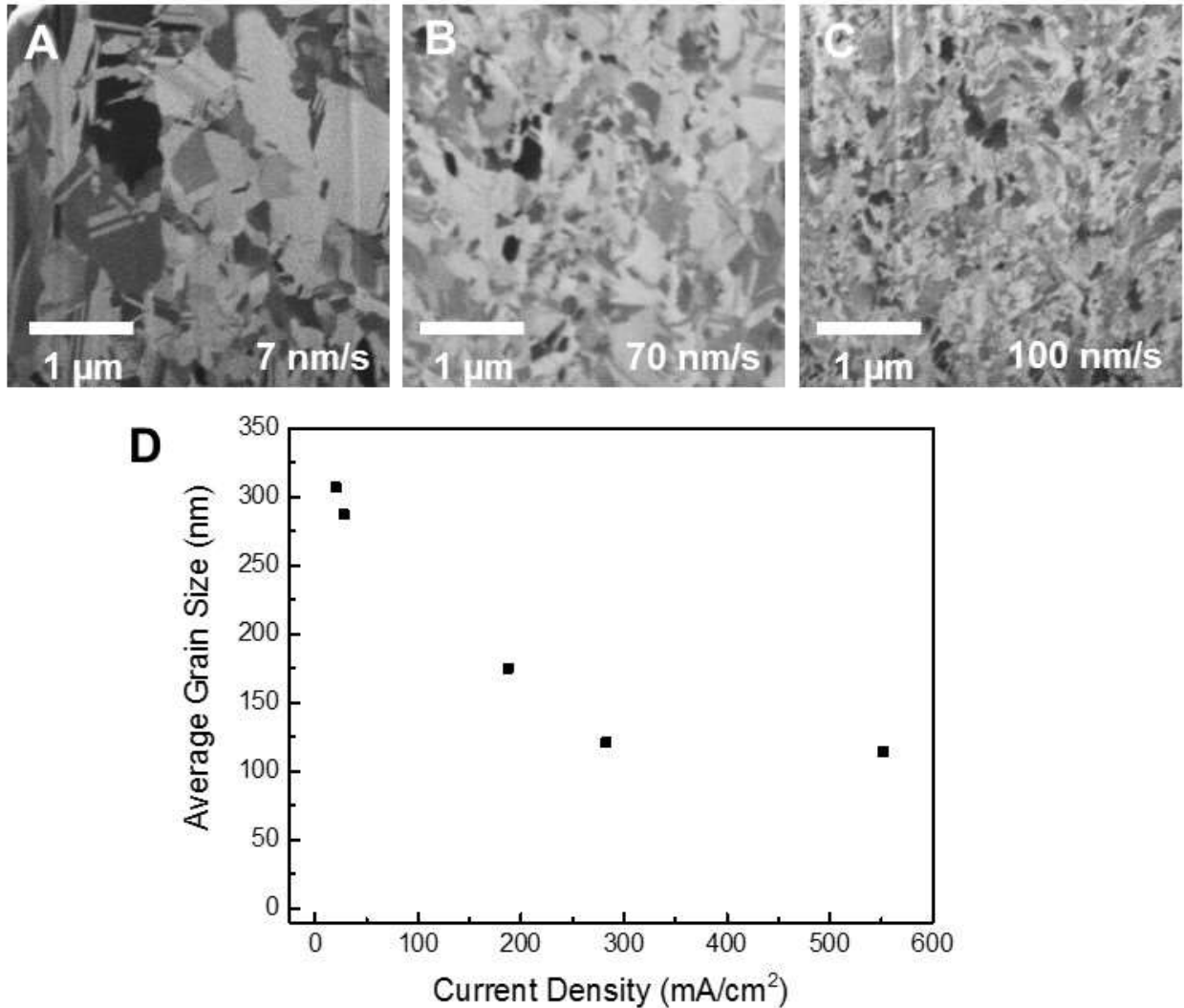


Figure 4.5. (A)-(C) The effect of the current density and deposition rate on the microstructure of Cu printed by DC-ED process. The cross-section FIB ion channeling contrast images of selected pillars show that increasing deposition current density causes grain refinement. The grain sizes of the pillars are (A)  $307 \pm 47$  nm (B)  $174 \pm 52$  nm (C)  $121 \pm 18$  nm. (D) Average grain size vs. current density for the metal printed using the DC-ED process.

The mechanical properties of selected nanotwinned Cu  $\mu$ -pillars were characterized using *in situ* SEM micro-compression experiments in order to investigate the microstructure-property

relationship of the printed copper by the L-PED process. The mechanical properties of the  $\mu$ -pillars printed at three different deposition rates of 10 nm/s, 18 nm/s, and 24 nm/s corresponding to average current densities of  $\sim 27.5$  mA/cm<sup>2</sup>,  $\sim 59.2$  mA/cm<sup>2</sup>, and  $\sim 72.7$  mA/cm<sup>2</sup>, respectively, were examined. Figure 4.6A shows an SEM image of the micro-compression experiment on an array of printed Cu  $\mu$ -pillars. A zoomed-in view of one the  $\mu$ -pillars after the compression experiment is shown in Figure 4.6B.

The compression stress-strain responses of the  $\mu$ -pillars are presented in Figure 4.6C. The true stress-strain was obtained by assuming a constant volume for the material during compression. Figure 4.6D is the comparison of the flow stress for the printed metal at different deposition rates and average current densities. Several observations can be made. First, variations in the stress-strain responses for the  $\mu$ -pillars printed with the same parameters are low. This indicates that the process is repeatable and the obtained microstructure is consistent. Second, a near-perfect elasto-plastic behavior with a smooth flow stress and no noticeable hardening was observed in compression stress-strain responses. There was a slight drop in the flow stress in the transition to the plastic region after the peak stress, which was attributed to the sudden initiation of the plastic deformation after dislocations pile-up against the TBs up to the point of maximum stress.<sup>57</sup> In nanotwinned Cu, the TBs effectively block the motion of dislocations similar to the grain boundaries, while they create more local sites for nucleation of dislocations. They also accommodate dislocation motion to elevate the ductility of the material.

Third, there was a clear difference between stress-strain responses of the  $\mu$ -pillars printed with different average current densities. The flow stress of the  $\mu$ -pillars deposited at 10 nm/s ranged from 616 MPa to 646 MPa with an average of  $630 \pm 15$  MPa. The flow stress of the  $\mu$ -

pillars deposited at 18 nm/s ranged from 765 MPa to 784 MPa with an average of  $773 \pm 9$  MPa. And the flow stress of the  $\mu$ -pillars deposited at 24 nm/s ranged from 885 MPa to 931 MPa with an average of  $909 \pm 23$  MPa. As shown in Figure 4.2, increasing the deposition rate in the L-PED process results in formation of grains with more aligned TBs and higher density of TBs. Densely packed printed nanotwinned Cu using the deposition rate of 24 nm/s and the average current density of  $\sim 72.7$  mA/cm<sup>2</sup> exhibited  $\sim 44\%$  higher flow stress compared to the Cu printed at the deposition rate of 10 nm/s and the average current density of  $\sim 27.5$  mA/cm<sup>2</sup>. Lastly, overall the strength of the printed metal was remarkable, considering that often time mechanical properties of the printed materials are inferior compared to their counterparts fabricated with other processing methods. A yield strength in the range of 600 MPa to over 900 MPa is several times of the bulk Cu. It is noted that the diameter of the  $\mu$ -pillars is large enough so that there is no size-effect in the obtained properties.

It is believed that dislocations are originated at the grain boundary triple junctions due to the stress concentration<sup>57</sup>. In the nanotwinned metal, the partial dislocations are not only blocked by the grain boundaries, but also TBs similarly block the intersecting slip planes. Dislocations are only allowed to propagate parallel to the TBs, and they pile up at the boundaries. The strength of the specimen increases by higher density of TBs following the Hall-Petch relation.<sup>40</sup> Additionally, for a metal with columnar-shaped grains, the plane orientation of the TBs with respect to the load direction significantly affects the strength.<sup>44</sup> The highest compression yield strength and flow stress are achieved when the loading axis is perpendicular to the planes of the TBs.<sup>60</sup> Therefore, the mechanical behavior of such materials strongly depend on the density and orientation of TBs.

Well-aligned and high density of TBs result in a lower density of stacking faults in the columnar grains, which enhances the strength of the metal.<sup>57</sup>

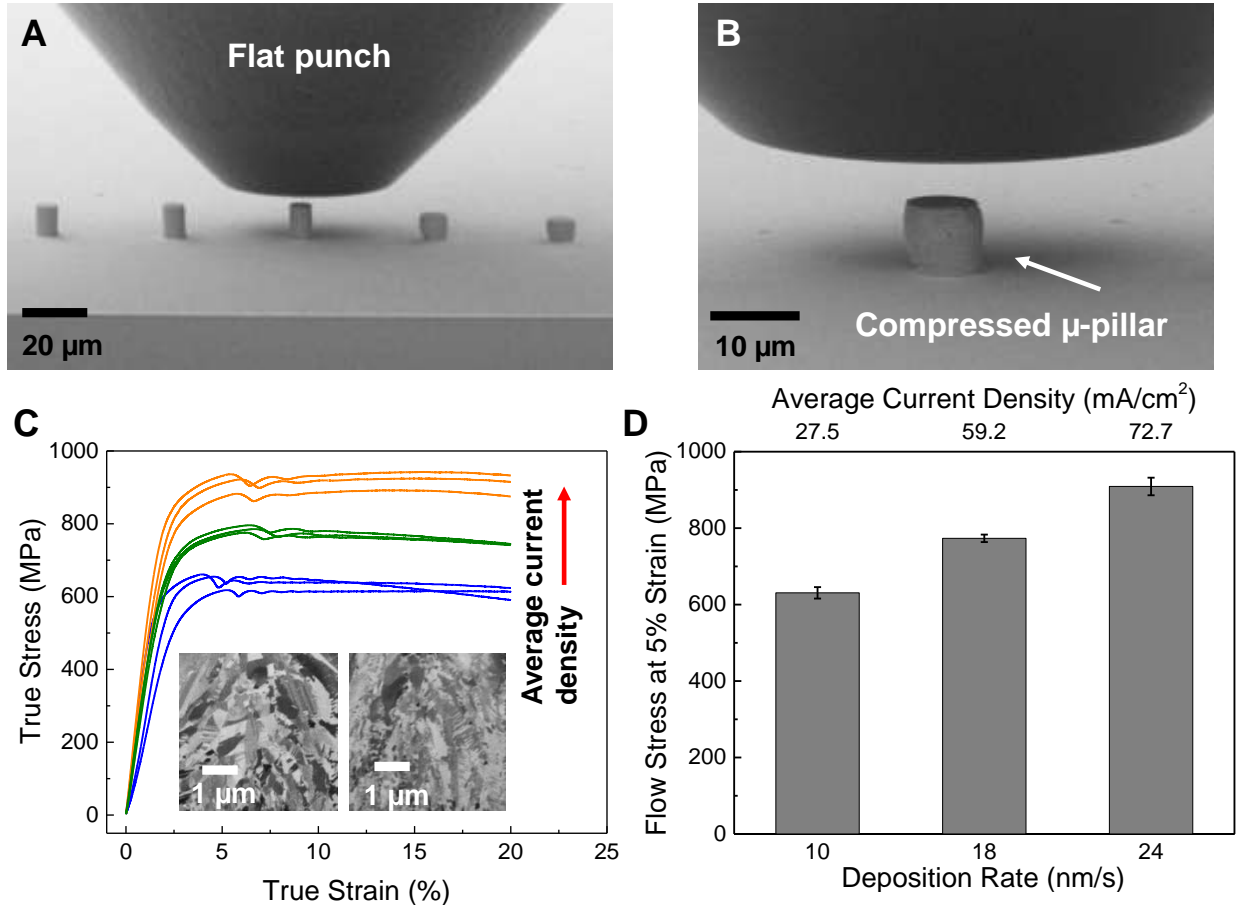


Figure 4.6. (A) In situ SEM micro-compression experiment on  $\mu$ -pillars printed using three different deposition rates (and average current densities). (B) SEM image of a compressed  $\mu$ -pillar. (C) Stress vs. strain responses of the  $\mu$ -pillars printed in three different deposition rates. (D) Comparison of the average flow stress of each microstructure.

Figure 4.7 shows a summary of the process-microstructure-property relationships for microscale printed Cu using the L-PED process. Employing constant current density in DC-ED mode results in nanocrystalline microstructure. Increase in the applied current density in DC-ED mode decreases the size of the grains through increase in the nucleation rates. Interestingly, PED by introduction of the OFF-potential during the process enables printing of nanotwined Cu. Results

revealed that deposition parameters in PED have significant effect on the microstructure of the printed metal. Raising the ON-time increases the density of TBs and their alignment within the grains by increasing the average current density and deposition rate. Boosting up the peak current density increases the twin density while decreasing the grain size significantly. Moreover, increasing the OFF-time period increases the grain size while decreasing the twin density.

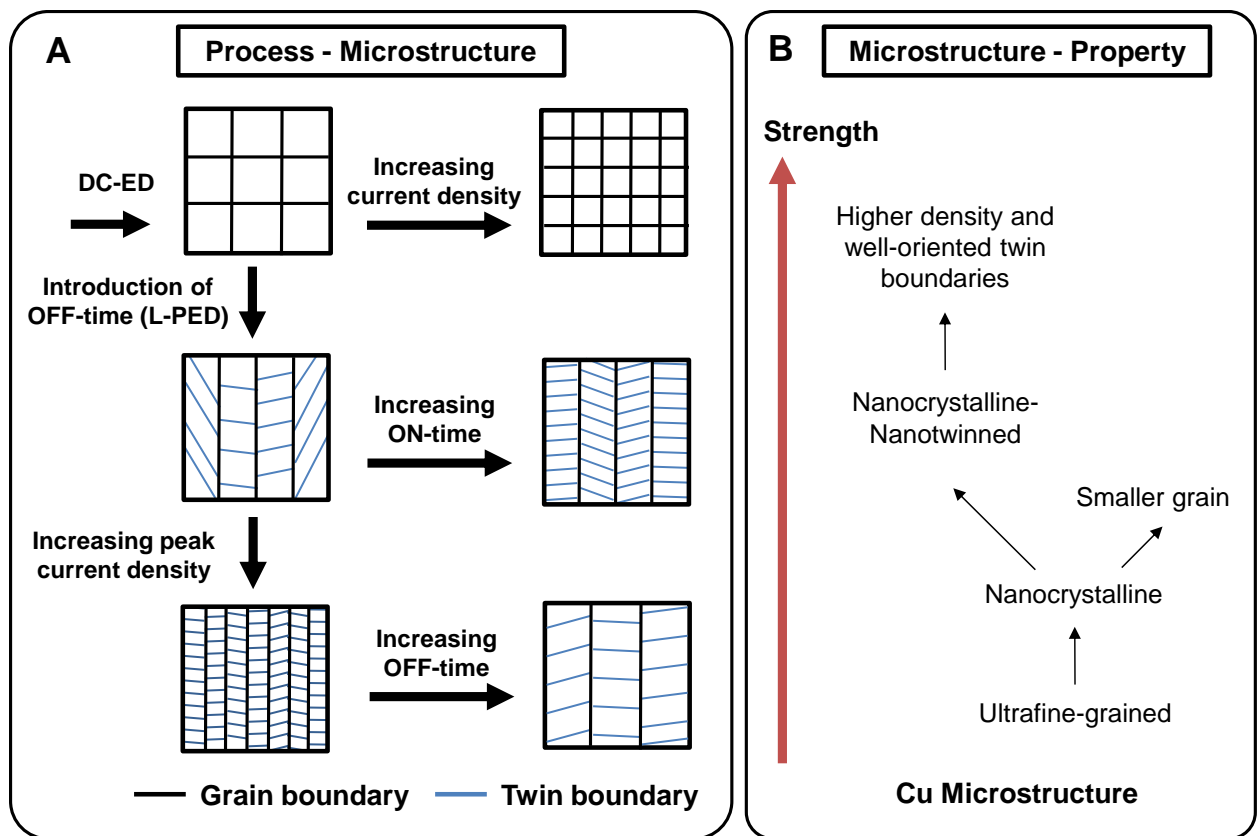


Figure 4.7. Illustration of (A) process – microstructure and (B) microstructure – property relations in microscale 3D printing of Cu by localized pulsed electrodeposition (L-PED) process.

Nanocrystalline Cu is known to be stronger than ultrafine-grained Cu because more grain boundaries can block the partial dislocations within the material. Therefore, based on the Hall-Petch relation,<sup>79, 80</sup> decreasing the grain size results in an increase the strength of the metal. The introduction of TBs within the grains increases the strength, since TBs can block the intersecting

slip planes similar to the GBs.<sup>42</sup> Hence, the strength increases with increasing twin density, following the Hall-Petch relation.<sup>40</sup> Additionally, the orientation of the TBs has significant effect on the strength of nanotwinned Cu; more aligned TBs results in a much lower density of stacking faults within the grains and enhances the strength.<sup>57</sup>

#### **4.4 Conclusions**

The promise of microscale additive manufacturing ( $\mu$ -AM) of metals is that the material is added layer by layer to form a desired geometry for various functional applications such as electronics, sensors, photonic, among others. Since the microstructure of a metal governs its mechanical and electrical properties, in addition to the geometry, the microstructure of the metal needs to be also engineered to achieve desired material properties. Our experimental results show that in the localized pulsed electrodeposition (L-PED)  $\mu$ -AM process, the average current density is the critical electrochemical process parameter for the control of the microstructure of the 3D printed copper. Increase in the average current density enhances the deposition rate of the metal, and in turn, results in the increase in the density of the twin boundaries (TBs), increase in the alignment of the TBs within the grains, and transition to columnar grains from randomly oriented grains. The results of the *in situ* SEM nanomechanical experiments show that such change in the microstructure directly enhances mechanical properties of the 3D-printed metal. Specifically,  $\sim 1.7$ -fold increase in the average current density results in  $\sim 1.4$ -fold increase in the deposition rate of the metal, which results in  $\sim 44\%$  enhancement in the flow stress of the printed metal. Specifically, the results show that the flow stress of the 3D-printed nanotwinned copper can be tuned from  $\sim 630$  MPa to  $\sim 910$  MPa (3-5 times of the bulk copper) by changing the microstructure during the printing.

## CHAPTER 5

### THERMAL STABILITY OF NANOTWINNED COPPER IN INTERCONNECTS ADDITIVELY MANUFACTURED BY LOCALIZED PULSED ELECTRODEPOSITION

#### 5.1 Introduction

The trend in miniaturization of electronic devices requires development of innovative micro/nanoscale metal fabrication techniques. While there is still no established additive manufacturing (AM) method for fabrication of metallic structure at the small scale, various techniques are under development for different applications.<sup>2</sup> These techniques are expected to benefit the integration of electronics and sensors. One of the most important driving factors of this process is fabrication of high quality and thermally stable materials with similar properties to the bulk level.

Among different AM methods recently introduced, the localized pulsed electrodeposition (L-PED) process as a cost-effective technique with high flexibility in preparing high quality metals, can be considered as one of the candidates to complement the conventional microfabrication of interconnects.<sup>54, 68</sup> The L-PED process is based on the localized electrodeposition of metals at the tip of an electrolyte-containing nozzle steered in 3D-axis using precision positioning stages to fabricate omni-direction or layer-by-layer metallic structures (Figure 5.1A). The L-PED process offers significant advantages compared to other processes for patterning and 3D printing of metals, including: (1) direct printing of pure metal without any need for additional post-processing, (2) no significant porosity in the structure after printing, (3) single step and low-cost process in room environment, (4) metal fabrication at wide ranges from nm to

mm using different nozzle diameter, and (5) control over the microstructure of the printed metal, and hence control over its mechanical and electrical properties. For instance, the L-PED enabled fabrication of nanotwinned copper (nt-Cu) with controlled twin density and thickness for the first time.<sup>68</sup> Nt-Cu interconnects with remarkable combination of mechanical and electrical properties are promising candidates for a range of applications in electronics.<sup>39</sup>

While the L-PED process aims to address some of the challenges in different applications in nanotechnology and electronics through fabrication of actual products such as interconnects, it is important to determine their maximum service temperature and thermal stability. The microstructure evolution at elevated temperatures, which usually causes unexpected failure in systems, is one of the most critical challenges in the high-performance applications. To date, there is no comprehensive study on thermal stability of the printed nt-Cu interconnects by the L-PED process. Therefore, understanding grain growth mechanism in 3D-printed interconnects requires further investigations, specifically for applications where the working temperature is higher than room temperature.

Generally, the nanocrystalline (nc) metals without any impurities are thermodynamically unstable, and grain growth may occur at lower temperature compared to nt-metals<sup>81, 82</sup>. Abnormal grain growth is reported for nc pure metals even at ambient environment<sup>83</sup>. The major driving force for the grain growth in metals is the high energy of the grain boundaries (GBs) and grain boundary junctions.<sup>84</sup> In order to improve the stability of pure metals, the driving force can be reduced by incorporation of more low energy boundaries in the microstructure.<sup>84</sup> For instance in copper, the energy stored at high-angle grain boundaries is approximately 20 times higher than the

twin boundary (TB) energy.<sup>81</sup> Therefore, the driving force for growth of grains is more than the force for coarsening TBs thickness.

Low energy coherent twin boundaries (CTBs) reduce the driving force for grain growth in Cu,<sup>85</sup> hence the presence of large number of coherent nanotwin (nt) boundaries within the microstructure results in better thermal stability. The superior thermal stability of nt-Cu may be because CTBs have close-packed atomic arrangement and low energy compared to the GBs, which makes CTBs less mobile at higher temperature. Also, it has been reported that the triple junctions formed in the intersection of a TB and a GB help to pin the grains and make them more stable.<sup>85</sup> However, the presence of high density of coherent twins is not sufficient for thermal stability, and the twin structure, including the defect content and network topology needs to be considered as well.<sup>86</sup> For instance, existence of random columnar GBs and large fraction of incoherent TBs significantly reduce the thermal stability.<sup>86</sup> It is noteworthy that the purity is one of important factors that should be considered in thermal stability of such structures, since impurities can pin GBs and keep them more stable.<sup>85</sup>

There are various processes for fabrication of nt-Cu. Each process results in different microstructures with distinct material properties.<sup>85</sup> Different factors such as GB energy, twin density and structure, and the presence of impurities can contribute to the stability of nt-Cu. Although aspects of thermal stability of nt-Cu are previously investigated at the bulk level, and it has been shown that nt-Cu films are much more stable than nanocrystalline (nc) and ultrafine grained (UFG) counterparts with high angle GBs,<sup>82</sup> a systematic study of grain growth kinetics in additively manufactured microscale nt-Cu interconnects as well as potential impacts on their mechanical and electrical reliability are required. The proposed research in this dissertation is

designed to address this critical gap. In this chapter, a comprehensive study on the thermal stability and reliability of the 3D-printed micro/nano-scale nt-metallic interconnects is presented to demonstrate the feasibility of using L-PED as an innovative AM technique for fabrication of high conductivity nt-metal features in electronics.

## 5.2 Materials and methods

**Description of printing process of nt-Cu interconnects by L-PED:** Nt-Cu micro-pillars were printed using a glass micropipette nozzle pulled to diameter of  $\sim 5 \mu\text{m}$  (P-97 pipette puller, Sutter Instrument). The micropipette was filled with the electrolyte of  $\text{CuSO}_4$  (100 mM) and  $\text{H}_2\text{SO}_4$  (1 M). A copper wire as anode electrode inserted from the back of the micropipette, and a gold-coated silicon substrate served as the cathode electrode. The nozzle tip was moved close to the substrate surface using a coarse motion control system (Newport Inc.) to form a meniscus (liquid bridge) between the tip and the substrate. Once the liquid bridge was formed, a pulsed current was applied between the two electrodes using a potentiostat/galvanostat (VersaSTAT 4, Princeton Applied Research) to deposit the metal at the limited area of the cathode surface. A high resolution (4 nm) three-axis nano-positioning system (Newport Inc.) was employed to control the motion of the substrate during deposition. The synchronized motion of the substrate and deposition resulted in 3D printing of pure nt-Cu interconnects. The relative humidity in the printing environment was controlled at  $\sim 65\%$ . The printing process was monitored in real-time using a high-resolution system including an optical objective lens coupled with a CCD camera (XM-10, Olympus). The schematic of the printing setup is shown in Figure 5.1A.

**Thermal annealing:** Each sample was annealed individually at 150 °C, 300 °C, and 450 °C for 4 hours, under identical conditions using the infrared lamp heater in a sputtering chamber (AJA

Orion Sputter) maintained at a vacuum pressure of  $\sim 5 \times 10^{-6}$  Pa. The heating rate was 10 °C/min, and the samples were cooled down to room temperature after heat treatment at the average rate of  $\sim 3$  °C/min. Large Argon gas flow was used to increase the cooling rate. Initially, the temperature dropped at a faster rate, and the cooling rate became much lower when the temperature in the chamber was below 100 °C.

**Microstructure characterization:** The microstructure of the 3D-printed interconnects were characterized utilizing the scanning electron microscopy (SEM, Zeiss Supra 40) and high-resolution focused ion beam (FIB, FEI Nova Nanolab 200). The surface morphology and size of the micro-pillars were examined under the SEM. The FIB was used to evaluate the grain size, twin boundary presence, and void formation in the cross-section of the micro-pillars, and to characterize the microstructural changes of printed samples after thermal annealing at different temperatures. A final acceleration voltage of 30 keV and current of 10 pA was used to mill and image the cross-section of the micro-pillars.

**Mechanical characterization:** In situ micro-compression experiment was performed in SEM to characterize the mechanical properties of the 3D-printed interconnects before and after thermal annealing. The tests carried out using an in situ SEM nanoindentation system (NanoFlip, Nanomechanics) with a 50  $\mu\text{m}$  diameter flat punch conductive diamond tip. Three samples were tested for each deposition parameter and heat treatment condition. The average diameter of the samples was  $\sim 4.5 \pm 0.1$   $\mu\text{m}$  with the length-to-diameter aspect ratio of  $\sim 2.7:1$  to minimize the buckling effects. The top surface of the micro-pillars were flattened using the FIB. The tests were performed under displacement-control mode at a constant displacement rate and constant strain

rate of  $1 \times 10^{-3} \text{ s}^{-1}$ . The deformation of the micro-pillars were monitored in real-time during experiment.

### 5.3 Results and discussion

Figure 5.1B and C demonstrates the feasibility of direct printing of micro-pillar nanotwinned-Copper (nt-Cu) interconnects using the ambient environment L-PED process. 3D nt-Cu interconnects were additively manufactured using pulsed electrodeposition at the tip of an electrolyte containing nozzle. In L-PED, the microstructure of the 3D printed interconnects, including twin boundary and grain formation, can be engineered by adjusting the deposition parameters. The mechanisms for control of the grain texture and twin densities by changing the peak current density and adjusting  $t_{on}$  and  $t_{off}$  (duty cycle) are reported in chapter 4.

In order to study the thermal stability of 3D-printed nanotwinned metallic interconnects, nt-Cu microbumps/micropillars were directly printed at two different deposition rates by modifying the peak current density. The detailed deposition parameters are presented in Table 5.1. Four sets of samples were printed at each deposition condition and each set was annealed at different temperature. The samples were annealed at 150 °C, 300 °C, and 450 °C for 4 hours.

The representative SEM images of the 3D printed pillars before and after annealing are presented in Figure 5.2. The post-annealing surface morphology of both type of the samples was investigated at different temperatures. It is clear that as the annealing temperature increases, the microstructure of the pillars is evolved. The annealing temperature is the driving force for growth of the grains, and once the temperature exceeds the critical temperature, which can be determined

based-on the microstructure, the grains start growing abnormally and coalesce. The grain growth may results in grain boundary groove deepening, void formation, or agglomeration.

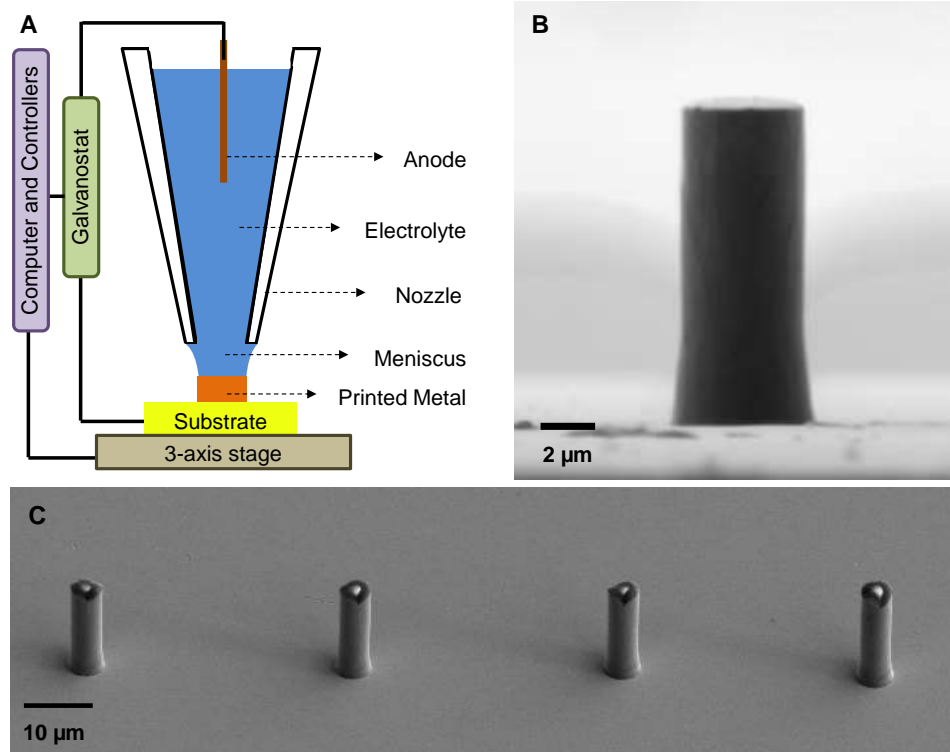


Figure 5.1. (A) Schematic view of the L-PED 3D printer setup. (B) A close-up view of 3D printed micro-pillar. (C) An array of printed micro-pillars interconnects.

The surface of the pillars were smooth and undamaged before annealing process (Figure 5.2A and E) and remained intact at lower annealing temperature. However a severe surface damage was observed in the Cu pillars after annealing at higher annealing temperature (Figure 5.2D and G-H). For the samples with higher deposition rate, the evolution occurs at 450 °C, while for the lower rate ones the evolution happened at lower temperature of 300 °C. Two different types of damage were observed in the samples. In the sample deposited at higher deposition rate, grooves were observed after annealing at 450 °C, whereas in the sample with lower deposition rate, isolated voids were formed after annealing at 300 °C.

The groove type damage is known to be formed along the grain boundaries in materials with a very large grains with high proportion of twin boundaries. On the other hand the voids are usually formed at the grain boundary triple junctions in materials with small grain size without significant amount of twin boundaries.<sup>87</sup> The damage type in Cu samples can be determined by understanding the distribution of mis-orientation angle. Park et al. suggested a microstructural parameter to predict the damage morphology in Cu film consists of grain size, film thickness, and fraction of the high energy grain boundaries.<sup>87</sup> The grooves and voids are formed along random high angle grain boundaries with mis-orientation angle of greater than 15°. In comparison, twin boundaries and low angle grain boundaries have lower grain boundary energy and diffusivity. Therefore, the size of the sample, grain size, and annealing temperatures affects the microstructure evolution of the annealed Cu. These factors control the phenomena by minimizing the energy including: surface energy, interface energy, and strain energy (elastic strain energy and plastic strain energy).<sup>88</sup>

FIB ion channeling contrast imaging was utilized to observe the microstructure of the cross-section of the pillars to investigate the microstructure evolution of the samples after heat treatment, and the location of the voids and their formation correlation with any microstructure components (Figure 5.3). Results exhibited significant difference in microstructure of the samples printed at two different deposition rates prior to annealing process. The sample deposited at higher rate revealed nt-Cu structure with columnar-shaped grains, while the ones deposited at lower rate exhibited nc-Cu microstructure with some grains containing TBs.

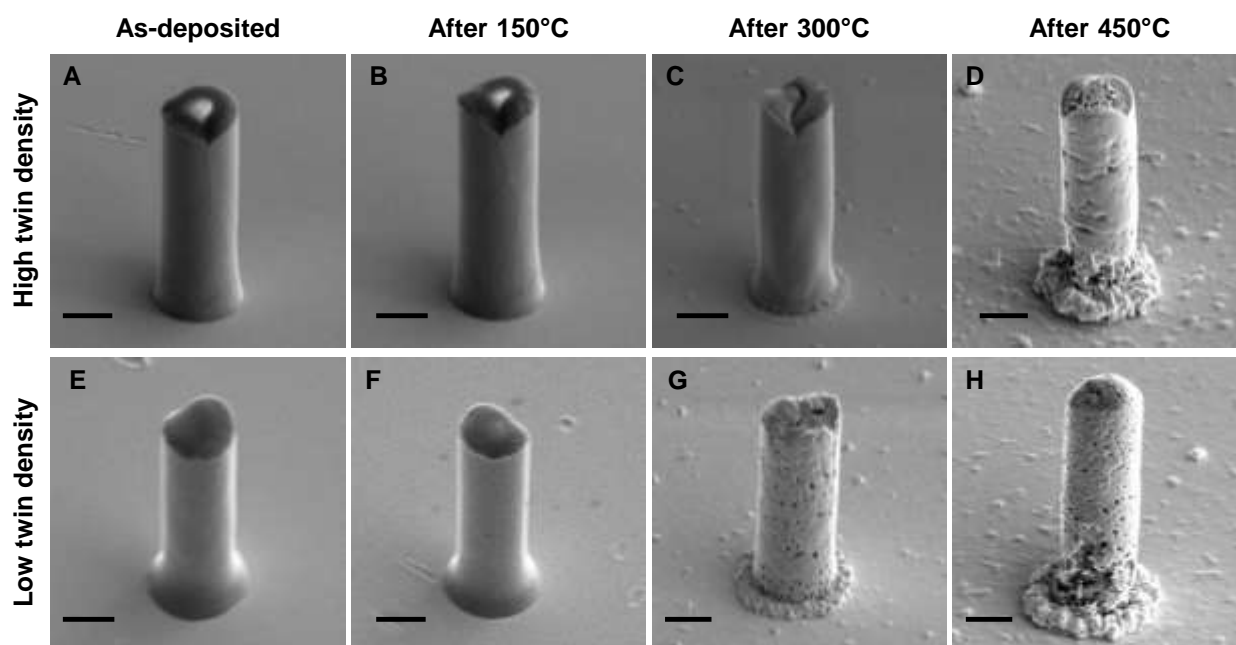


Figure 5.2. SEM surface images of nt-Cu micro-pillars with high density of twins (A) as-deposited and after 4 hours annealing at (B) 150 °C (C) 300 °C (D) 450 °C and nt-Cu micropillars with low density of twins (E) as-deposited and after 4 hours annealing at (F) 150 °C (G) 300 °C (H) 450 °C. All scale bar are 3  $\mu\text{m}$ .

Table 5.1. The process parameters of micro-pillars printed using the L-PED process.

Sample Number	ON Time (s)	OFF Time (s)	Peak Current Density ( $\text{A}/\text{cm}^2$ )	Average Current Density ( $\text{mA}/\text{cm}^2$ )	Deposition Rate ( $\text{nm}/\text{s}$ )	Twin Density
1	0.02	1.98	5.12	51.2	18	Low
2	0.02	1.98	7.27	72.7	23	High

A comparison on grain growth of two samples illustrated the superior thermal stability of nt-Cu. The microstructure of both samples remained intact at 150 °C. In nc-Cu samples, grains grew rapidly at 300 °C where voids were formed in the entire sample (Figure 5.3G), while the twin boundaries in nt-Cu remained stable, and no void is observed (Figure 5.3C). At 450 °C, large grains were formed in both samples. Although an anisotropic crystal growth was reported in reference <sup>89</sup> for nt-Cu annealed at 450 °C, both samples printed using L-PED did not show any

extreme abnormal grain growth. The seed layer, which serves as nuclei at the substrate interface, plays a critical role in the microstructure of the samples. There exist an ultrafine grained transition layer between the seed layer and the preferred (111) orientation nt-Cu, which can result in inconsistent microstructure and properties. Therefore, the stability of the base of the pillars are different from the main body of the sample, and some micro-voids are observed in transition region of nt-Cu pillars. Previous studies show that some voids preexist in as-deposited electroplated nt-Cu structures surrounding columnar grains.<sup>90</sup> Also, some of these voids appear on the interface between the seed layer and deposition where the micro-cracks interrupt the electroplating due to their small size and poor wettability.<sup>91</sup> The desired microstructure can be achieved in this layer by engineering the properties of the seed layer.

The formation of voids is not desirable in in 3D-printed Cu interconnects because it increases the electrical resistance and limits the attainable maximum anneal temperature. Although there were some investigations on formation of voids in Cu after heat treatment, the actual cause of the phenomena is still matter of debate. The results show that the voids are formed mostly along the grain boundaries due to diffusion creep at grain boundary triple junctions and at grain boundaries. However there are few voids in grain interior, too. Formation and growth of void is driven by the stress gradient.<sup>92</sup> Therefore, the understanding of the stress distribution in microstructure helps to realize the stress induced voiding in samples.

During heat treatment, the sample is subjected to thermal strain, but in Cu samples the elastic moduli for a given strain is different for grains with different orientation. This anisotropy results in different thermal stresses, and stress concentration arises at the interfaces to satisfy the boundary conditions.<sup>93</sup> Although decreasing the stress is the thermodynamic driving force for void

formation, the microstructure influences stress voiding resistance significantly. As can be seen in Figure 5.2C and 5.3C, the nt-Cu pillars with more textured microstructure revealed better resistance to void formation. The results indicates that the void formation is noticeably associated with non-perfect local texture. In the voided regions, the grain boundaries allowed more diffusion than the ones within the intact regions. Hence, local variations in microstructure plays an important role in affecting the reliability of printed structures. This difference in orientation of the two grains contributes to the concentration of thermal stress. During annealing process the density of strong texture is decreased, the diffusion is enhanced and therefore voids are formed at a grain boundaries triple junction where there were at least two grains with high biaxial elastic modulus.

The lower stability of non-textured sample is consistent with previous studies showing that the voids were located at the locally weaker [111] texture with higher diffusivity and twist boundaries.<sup>94</sup> The comparison of boundaries in immediate vicinity of voids and the ones from intact regions revealed that the zones associated with more favorable kinetics such as lower strength [111] texture, grain boundaries with higher angle character with twist components are more subjected to formation and growth of voids.<sup>95</sup>

In Figure 5.3F, voids can be observed at the intersections of grain boundaries with twins. The annealing twins were formed in Cu samples during heating process. As these new orientations are developed, the texture strength became weak. The properties of incoherent annealing twin interfaces are analogous to common grain boundaries with large angle.<sup>93</sup> Therefore, the interface energy and the diffusivity is higher in these [322] twins compared to the [111] twins, which make the void formation and growth easier. Sekiguchi et al. found a consistent correlation between the void formation sites and terminating corners of incoherent twins in [322] planes.<sup>92</sup> The correlation

between the void formation tendency and twin formation can be explained as follows. During heating process, annealing twins are formed which has different crystallographic orientations from the parent matrix. When the sample is subjected to the isotropic thermal strain, the large elastic anisotropy of Cu makes different thermal stress in the twin and the parent matrix. This difference results in stress concentration at the twin interfaces, corners, and intersections.<sup>92</sup> This stress concentration can drive diffusion along the interfaces which leads to formation of the voids. The work for nucleation of a void is estimated to be twice the surface energy minus the twin interface energy.<sup>96</sup> The larger twin interface energy in incoherent twins compared to coherent twins makes the void formation in presence of concentrated stress easier. At regions with stress concentration, the voids are formed by interface decohesion failure, and get the round shape by diffusion. Hence, it's unlikely to nucleate decohesion-type voids in strong coherent twin interfaces.

The compression strength of the micro-pillars printed at two different deposition rates of 18 nm/s and 23 nm/s was examined *in situ* SEM using micro-compression for as-deposited and after annealing at 300 °C for 4-hour samples. The SEM images of the micro-compression experiment on the array of printed nt-Cu samples before and after the tests are shown in Figure 5.4A-C. Figure 5.4D presents the true stress-strain responses of the pillars at different conditions obtained from the load-displacement data. It is noteworthy that with low initial porosity of the voided sample, there is no significant volume reduction during compression test and true stress can be estimated by standard procedure.<sup>97</sup> As expected, the stress-strain responses shift downwards with decreasing the deposition rate. The results show slight difference between the strength of the pillars printed at two different deposition rates prior to annealing. In nt-Cu, the TBs block the

motion of intersecting dislocations, which increases the strength of the material, and accommodates parallel dislocation motion to elevate the ductility of the material.

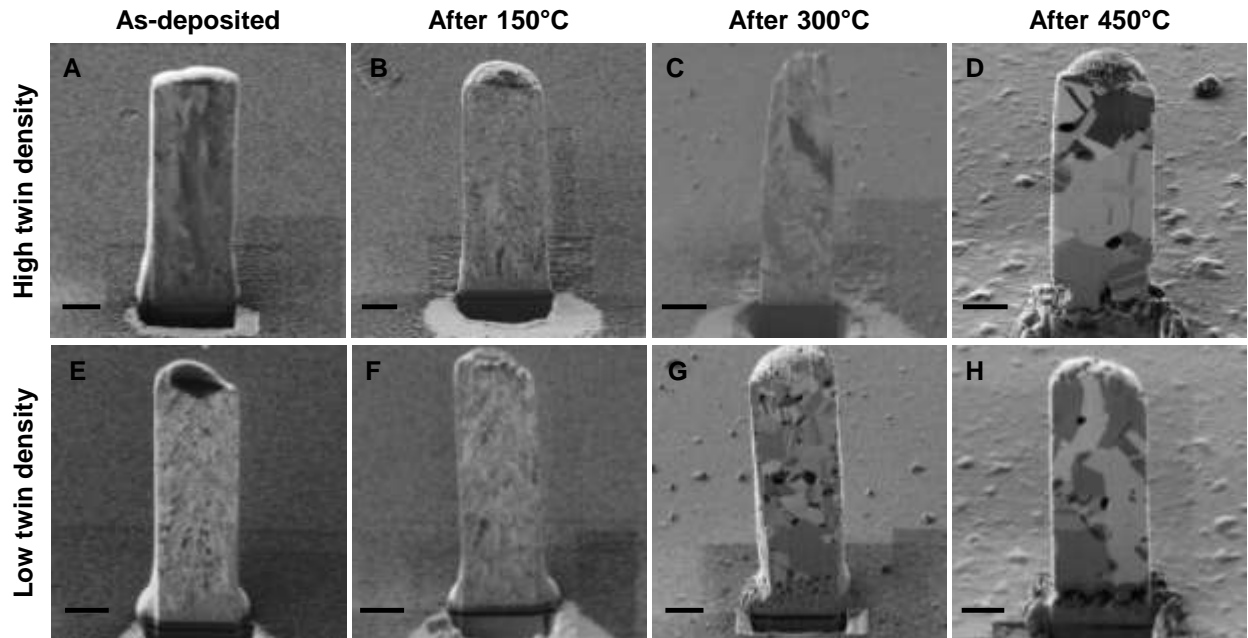


Figure 5.3. Cross-sectional FIB ion contrast images reveal the microstructure of nt-Cu micropillars with high density of twins (A) as-deposited and after 4-hour annealing at (B) 150 °C (C) 300 °C (D) 450 °C; and nt-Cu micropillars with low density of twins (E) as-deposited and after 4-hour annealing at (F) 150 °C (G) 300 °C (H) 450 °C. Scale bars are 2  $\mu\text{m}$ .

Moreover, it is evident that the strength of samples decreases after annealing process at both deposition rates. Near-perfect elasto-plastic behavior without hardening is perceived in stress-strain responses for the printed pillars before annealing and annealed ones deposited at 23 nm/s. The slight drop in the flow stress in the plastic region is attributed to the initiation of the plastic deformation and dislocations pile-up against the TBs. However, substantial strain hardening occurred for annealed pillars printed at 18 nm/s. The strain hardening can be related to the strain hardening of the Cu structure and the void closure during compression.<sup>97</sup>

Figure 5.4E reveals the comparison of the flow stress at 5% strain of the pillars before and after annealing for the printed metal at different deposition rates. The flow stress of the pillars deposited at 18 nm/s ranged from 760 MPa to 854 MPa with an average of  $811 \pm 47$  MPa, while the flow stress of the samples printed at 23 nm/s ranged from 860 MPa to 875 MPa with an average of  $868 \pm 8$  MPa. Increasing the peak current density and accordingly the deposition rate resulted in columnar structured nt-Cu with higher density of TBs, which led to ~7% higher flow stress compared to the nt-Cu with lower TBs density. The flow stress of nt-Cu with high density of TBs decreased to approximately  $522 \pm 25$  MPa after 4 hours annealing at 300 °C. With increasing the grain size and twin thickness, the strength of nt-Cu decreased gradually.

In comparison, the strength of the low density nt-Cu pillars with random oriented grains after annealing in the same condition dropped significantly to  $229 \pm 5$  MPa. Hence, the strength of pillars deposited at 23 nm/s decreased 39%, while it decreased 72% for the samples printed at 18 nm/s. The results confirm the microstructure evolution observation and can be interpreted as higher thermal stability of the nt-Cu pillars with high density of TBs with columnar grains.

The strong textured microstructure with lower surface energy plays an important role in higher thermal stability of columnar-grained nt-Cu in comparison to the ones with randomly oriented grains. The energy of columnar grain boundaries is less than that stored in equiaxed grains. Also, the faceted columnar GBs, which originated from the propagation of twin boundaries in lateral direction, employ a pinning effect on the grain growth.<sup>82</sup> It has been reported that the optimal microstructure for maximum thermal stability can be achieved by incorporation of high density of CTBs within columnar grains with three-120° configuration.<sup>84</sup>

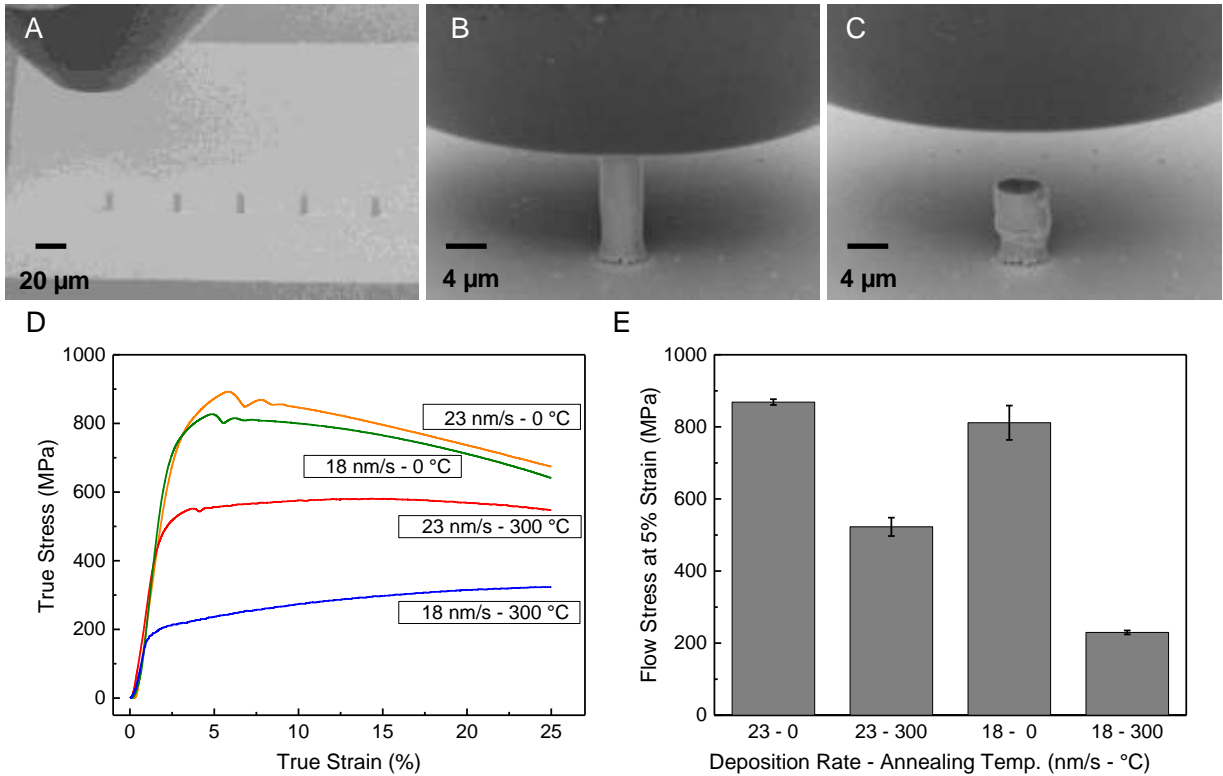


Figure 5.4. (A) In situ micro-compression experiments on an array of nt-Cu micro-pillars printed using the L-PED process. (B) The close-up SEM view of micro-pillar at beginning of the test. (C) SEM image of compressed micro-pillar. (D) True stress-Strain responses of the micro-pillars printed in two different deposition rates of 23 nm/s and 18 nm/s and annealed for 4 hours at 300 °C. (E) Comparison of the average flow stress of each micro-pillar at 5% strain.

## 5.4 Conclusion

An investigation was carried out on thermal stability and mechanical properties of 3D-printed micro-scale nt-Cu interconnects at different temperatures. The results show that L-PED enables microstructure engineering to enhance the material's performance at elevated temperature and avoid the void formation. Nt-Cu with low and high density of TBs were printed at two different deposition rates and annealed at different temperatures. Surface damage was detected in the nt-Cu pillars after annealing for 4 hours at 450 °C and 300 °C for the material printed at deposition rates of 23 nm/s and 18 nm/s, respectively. TBs in nt-Cu pillars with columnar shaped grains printed at

23 nm/s remained stable at temperature of 300 °C. The pillars exhibited high compression strength of 522 MPa after annealing, decreased from 868 MPa in as-deposited state, which indicates the high thermal stability of such 3D-printed interconnects. In general, the strength and stability of the printed metal was remarkable, and was not inferior compared to their counterparts fabricated with other processing methods. Understanding of the effects of temperature on the grain growth combined with microstructure engineering can enhance the material's performance in wide range of industrial applications. This research can yield important advancement in 3D printing of electronics, and be of considerable value for use in nanotechnological applications.

**CHAPTER 6**  
**A MICROSCALE ADDITIVE MANUFACTURING APPROACH FOR IN SITU**  
**NANOMECHANICS**

**6.1 Introduction**

There is a constant demand for the development of high performance metals and alloys with enhanced strength at a lower weight. Development of metals and alloys with new microstructure and/or composition often requires knowledge on the process – microstructure – property relationship. In particular, to understand the effect of the microstructure on mechanical properties, various experimental methods such as simple tension, three-point bending, and fracture toughness tests are used. Often times, knowledge on the deformation mechanism at the micro and nanoscale is required to complement the bulk mechanical properties.<sup>98</sup> *In situ* scanning electron microscope (SEM) and transmission electron microscope (TEM) experiments have provided powerful characterization methods for the direct observation of deformation mechanisms.<sup>58, 99-105</sup> In particular, *in situ* SEM micro-pillar compression has been the hallmark of nanomechanical characterization techniques.<sup>3, 5, 59, 106-113</sup> In this experiment, pillars with diameters of several microns or sub-micron are compressed using a flat microscale tip, meanwhile the deformation of the pillar is captured in a series of SEM images. The obtained SEM micro-graphs are analyzed combined with the acquired force-deformation responses to construct the deformation mechanism of the material.

To obtain the micro-pillars for *in situ* SEM micro-compression experiments, often thin films or bulk of the material of interest are milled using the focused ion beam (FIB) in consecutive

steps in a top-down approach. A typical micro-pillar may require FIB time of few hours to more than 24 hours,<sup>106, 108</sup> which can mount to hundreds to a few thousands of dollars for sample preparations, considering high cost of FIB. The long duration exposure to heavy ions in FIB can also introduce damage into the material.<sup>4, 6, 7, 108</sup> Ions from the beam may also get embedded into the material of the micro-pillar in this process. It has been shown that the composition and microstructure of the surface layer of the material can be compromised in FIB milling process. This in turn, may alter the true deformation mechanism in the material and lead to compromised conclusions. Moreover, there are practical difficulties with fabricating accurate pillars with diameter of less than 0.5  $\mu\text{m}$ .<sup>106, 108</sup>

An alternate nanofabrication method has been also reported based on electroplating into a PMMA (Poly(methyl methacrylate)) template that is patterned by electron beam lithography.<sup>10</sup> The developed technique is a non-damaging method for fabrication of isolated metal nanopillars with diameter of less than 100 nm for mechanical characterization. While this method is efficient for rapid fabrication of arrays of nanopillars, it requires additional processes for fabrication and removal of the template.

In this chapter, a bottom-up process, termed localized pulsed electrodeposition (L-PED) is introduced, which is based on microscale AM to enable a more convenient method for *in situ* SEM studies of mechanical properties and deformation mechanisms of metals and alloys. This process enables direct deposition of nano-pillars and micro-pillars of metals and alloys in room environment. In addition to the size, this process enables control over the microstructure of the deposited material to facilitate investigation of microstructure – property relationship. Depending on the size and type of the desired microstructure, a typical micro-pillar can be fabricated in a

single step in few minutes to tens of minutes at a low-cost and without any beam-induced damage. When combined with *in situ* instrumentation, this approach may enable high-throughput investigation of the process – microstructure – property relationship in particular for nanocrystalline and nano-twinned metals and alloys. In Figure 6.1, this microscale AM process is schematically compared to the FIB milling and template-based electrodeposition approaches for fabrication of micro-pillars for *in situ* SEM studies.

## 6.2 Materials and methods

Direct printing of Cu micro-pillars were carried out using glass micropipettes that were pulled to the desired pillar diameter. Solution of CuSO<sub>4</sub> (100 mM) and H<sub>2</sub>SO<sub>4</sub> (1 M) was utilized as the plating electrolyte. A substrate of gold-coated silicon and a copper wire inserted from the back of the nozzle functioned as the working electrode and the counter electrode, respectively. The RH of the printing environment was controlled at 65% during the process. The morphology and geometry of the micro-pillars were investigated using a SEM (Supra 40 Zeiss). High-resolution FIB imaging (FEI Nova Nanolab 200) was utilized to study the microstructure of the printed Cu. The cross-section of the micro-pillar was milled at a final acceleration voltage of 30 keV and a current of 10 pA, and observed with the same parameters.

Micro-compression experiments were carried out on the printed micro-pillars using an *in situ* SEM nanoindentation system (NanoFlip, Nanomechanics). A 50 μm diameter flat punch tip was used as the compression anvil. The tests were run at displacement-control mode at a constant displacement rate (constant strain rate of  $1 \times 10^{-3} \text{ s}^{-1}$ ). The true stress-strain response was calculated based on the obtained load – displacement data, and the geometry of each specimen. The electrical characterization of individual pillars were performed *in situ* SEM using a nanomanipulator

(Kleindiek Nanotechnik), a power supply, and a picoammeter (Keithley). Three samples were tested for each characterization type.

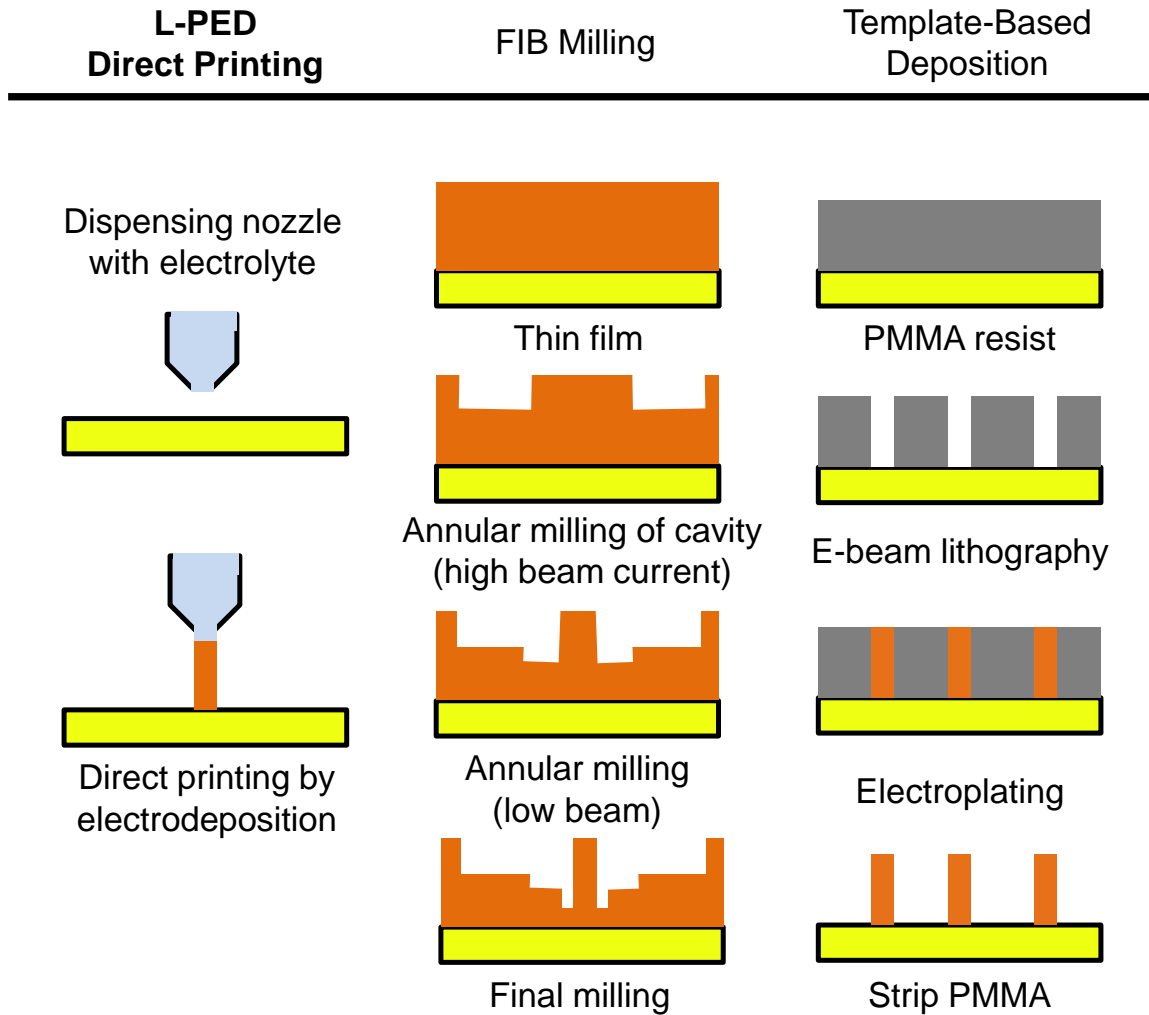


Figure 6.1. Comparison of the L-PED AM process with the FIB milling and template-based electroplating approaches for fabrication of micro-scale pillars. AM enables fabrication of specimens in a single step at low-cost in room environment.

### 6.3 Process description

The new approach for AM of metallic micro-pillars for *in situ* SEM micro-compression experiments is based on 3D printing via localized electrodeposition (Figure 6.2A).<sup>54, 68</sup> This

process is described in details in Chapter 2. The input to the program is a CAD model of the desired geometry to be fabricated, which in this case will be a straight micro-pillar. When the nozzle approaches to a conductive substrate, a meniscus (or also known as liquid bridge) forms between the tip of the nozzle and the substrate. This liquid bridge between the tip of the nozzle and the substrate forms the electrolyte bath for the localized electrodeposition process, and it moves with the nozzle in 3D-XYZ as the material is being deposited. A potentiostat/galvanostat applies the desired potential between the anode inserted in the nozzle and the cathode (substrate). Metal ions from the electrolyte reduce at the growth front within the electrolyte meniscus, and through controlled relative motion of the nozzle and the substrate, metal is printed in any desired 3D geometry (Figure 6.2B).

The initial distance between the nozzle tip and the substrate to form the liquid bridge depends on different factors including the surface condition, which comes from the nature of the solution and the nozzle, and the diameter of the tip. In this study, the formation of the meniscus is perceived by real-time monitoring of the current profile in the circuit during the process. In approaching step, an appropriate low potential (-0.02 V) is applied between the electrodes. A sharp rise in the current indicates the formation of the liquid bridge between the nozzle tip and the substrate. The approaching potential is chosen low to not deposit any metal in this stage.

### **6.3.1 Process parameters for micro-pillar manufacturing**

*Size of the printed pillars:* The size of the printed pillars depends on the size of the electrolyte meniscus between the tip of the nozzle and the growth front (initially the substrate). Based on the theoretical models of the liquid capillary, the diameter and height of the meniscus is

on the order of the magnitude of the nozzle tip, which can vary from sub-100 nm to several millimeters, based on the size of the desired pillar to be fabricated. Often, a glass pipette puller is used for fabrication of nozzles with the desired diameters.

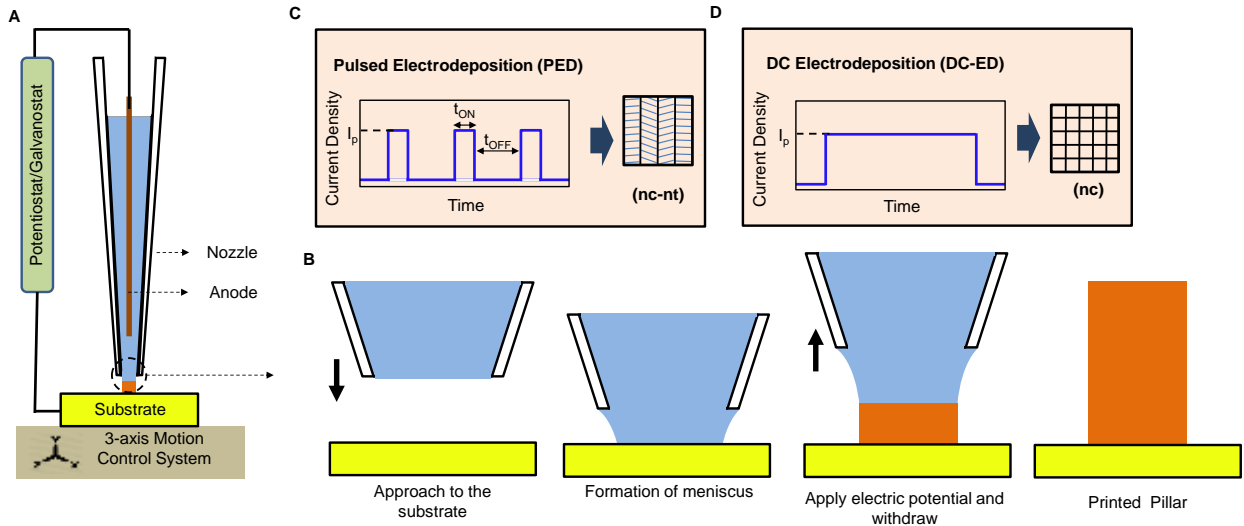


Figure 6.2. (A) Schematic view of the L-PED 3D-printing setup. (B) The printing process of a micro-pillar using the L-PED process includes approach of the nozzle-tip to the substrate, formation of the meniscus (liquid bridge) between the tip and the conductive substrate as the confined electrodeposition bath, application of an electric potential between two electrodes and deposition of the metal ions at the growth front followed by controlled withdrawal motion of the nozzle. (C)-(D) Process parameters of the L-PED process can be adjusted, which enables control over the microstructure of the printed structures: (B) Pulsed electrodeposition (PED) results in nanocrystalline nanotwinned microstructure, while (C) DC electrodeposition (DC-ED) produces nanocrystalline microstructure.

The multi-physics models and experimental results have shown that for a given nozzle diameter, pillars in the range of 0.5- to 0.9-time of the diameter of the nozzle can be 3D-printed (Figure 6.3A)<sup>31</sup>. This is because increasing the withdrawal speed of the nozzle stretches the electrolyte liquid bridge within its stable range and results in a finer diameter pillar for a given tip diameter of the nozzle. Therefore, the size of the printed pillars can be controlled by adjusting the withdrawal speed of the nozzle. On the other hand, the withdrawal speed of the nozzle depends on

the deposition rate of the pillars, which depends on the deposition parameters such as concentration of the electrolyte, the RH of the environment, and the applied potential. Figure 6.3B and C show two different Cu micro-pillars with diameter of 0.73  $\mu\text{m}$  and 5.25  $\mu\text{m}$  printed using the L-PED process by two different nozzles. The height of the pillars that can be fabricated is only limited by the travel range of the piezo actuator. For *in situ* SEM micro-compression experiments, micro-pillars are preferred to have specific aspect ratio (generally 2:1 to 3:1 height-to-diameter) to ensure that they are not too short to be affected by the top and bottom constraints, and not too tall to buckle during the micro-compression experiment.

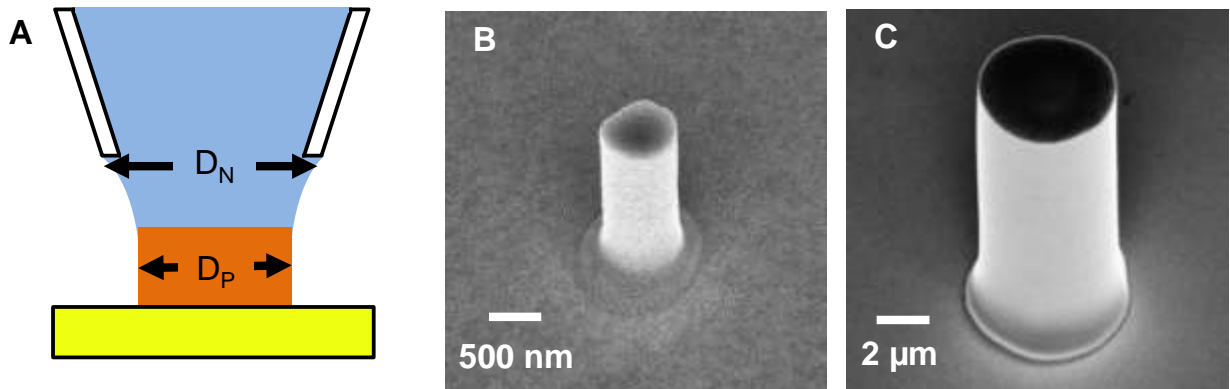


Figure 6.3. (A) Dependence of the diameter of the printed pillar ( $D_P$ ) on the diameter of the nozzle tip ( $D_N$ ). Micro-pillars with diameter in the range of 0.5- to 0.9-time of the diameter of the nozzle can be printed. (B) – (C) Cu micro-pillars printed using the L-PED process with different diameters of 0.73  $\mu\text{m}$  and 5.25  $\mu\text{m}$  by different nozzles.

**Microstructure control:** The L-PED process is capable of control over the microstructure of the printed pillars, similar to the extent of microstructure control in the bulk electrodeposition process. Specifically in electrodeposition, the grain size, grain orientation, nanotwin density and orientation can be controlled through process parameters. This capability may enable investigation of process – microstructure – property relationship of different materials. The deposition parameters can be controlled during the printing process at different modes of direct current

electrodeposition (DC-ED) or pulsed current electrodeposition (PED) with arbitrary current densities and duty cycles. As demonstrated schematically in Figure 6.2C and D, the DC-ED process results in nanocrystalline (nc) microstructure, while introduction of the OFF-time during the PED changes the microstructure of the printed metal to nanocrystalline nanotwinned (nc-nt) microstructure with columnar-shaped grains<sup>68</sup>. The process can be extended to control over the grain size and orientation, density of twins and orientation by adjusting the deposition parameters.

For instance in electrodeposition of nt-Cu, increasing the average current density and accordingly the deposition rate of nt-Cu, increases the twin density.<sup>40</sup> In particular, increasing the peak current density increases the twin density significantly while decreasing the grain size. Raising the pulse ON-time period during printing process increases the density of TBs and their alignment within the grains by increasing the average current density. Additionally, increasing the OFF-time period increases the grain size while decreasing the twin density.<sup>52,76</sup> The FIB and TEM imaging are often employed to investigate the microstructure of the pillars. The FIB ion-contrast image of the cross-section of the pillar provides a primary qualitative knowledge on the microstructure, and TEM can deliver the details in higher resolution.

**Deposition rate:** One advantage of the L-PED process is high throughput fabrication of the micro-pillars compared to the FIB-based milling process. The printing speed of the micro-pillars depends on the deposition mode and the process parameters for specific microstructure. Generally higher average deposition rate is achieved in DC-ED mode where there is no interruption in growth during printing ( $T_{OFF} = 0$ ). However, in order to obtain various microstructures, in particular twin boundaries (TBs) within the grains, the OFF-time is introduced periodically to interrupt the growth, which significantly lowers the printing speed. For instance, introducing OFF-time with

duty cycle of  $1/100$  ( $\frac{T_{ON}}{T_{ON} + T_{OFF}}$ ) while keeping the ON-current density constant, results in 100 times reduction in the printing rate.

Based on the experiments, using different deposition modes and parameters including the applied current density and duty cycle, Cu micro-pillars with the printing rate in the range of 2 nm/s to 250 nm/s depending on the desired microstructure can be fabricated. For example, fabrication of a typical nc-Cu micro-pillar with 5  $\mu\text{m}$  diameter and 15  $\mu\text{m}$  height at an average deposition rate of 100 nm/s takes about 2.5 minutes. As a comparison, fabrication of the same pillar with the FIB milling would take more than 4 hours of ion milling, which, in addition to the prohibitive cost, may leave the sample with damaged microstructure. FIB milling approach has certain advantages for preparation of micro-pillars for *in situ* SEM micro-compression experiments. FIB can operate on almost all types of metals and alloys. While the AM method discussed here can be applied to a sub-set of metals and alloys that can be electrodeposited. Additionally, the deposition rate of the pillars is highly dependent on the electrolyte concentration. Increasing the concentration of Cu ions in the electrolyte increases the current density during the ON-time and accordingly increases the deposition rate. Due to the fast evaporation of water in the L-PED process, the concentration of metal ions in the meniscus varies from the bulk concentration and increases during the OFF-time. Therefore, there is a limitation for increasing the concentration because in the nozzles with smaller diameter, which the volumetric evaporation rate is higher, this will cause clogging of the tip. It should be noted that during the ON-time period, the concentration of ions decreases due to the ion consumption. The detailed history of the electrolyte concentration during the process is discussed in multi-physics simulation studies presented in our recent publications.<sup>54</sup>

## 6.4 Results and discussion

Figure 6.4A shows a SEM image of an array of directly printed Cu micro-pillars using the L-PED process with a diameter distribution of  $4.60 \pm 0.08 \mu\text{m}$  and height of  $11.80 \pm 0.11 \mu\text{m}$ . The micro-pillars were printed with  $T_{on}$  of 20 ms,  $T_{off}$  of 2 s. The peak current density during deposition was  $\sim 3.7 \text{ A/cm}^2$  at a deposition rate of 12 nm/s. The printing of each micro-pillar took about  $\sim 16$  minutes, at this deposition rate, which is much faster compared to the FIB milling process. The pillar was sectioned using the FIB to reveal its internal structure. It can be observed that the pillar is fully dense with no apparent porosity.

Figure 6.4B presents the FIB ion channel contrast image of the cross-section of a micro-pillar printed using the L-PED process. The result exhibited ultrafine-grained microstructure, and the channeling contrast revealed the existence of TBs within most of the grains. The introduction of the OFF-time in the L-PED process changes the microstructure of the printed metal similar to the bulk PE process. The L-PED deposited pillars demonstrated nanotwinned microstructure with columnar-shape grains with an average diameter of  $\sim 300 \text{ nm}$ , separated into twin/matrix lamellar structures by TBs. The average grain size was measured using the FIB cross-section image and intercept procedure.

Fig. 6.4C shows the dark-field TEM image of the cross-section of a micro-pillar. The inset diffraction pattern reveals the polycrystalline structure of the micro-pillar. A grain with TBs is highlighted in the image. The high resolution TEM image of a TB is presented in Fig. 6.4D. The TB is shown by the dashed line. The two sides of the TB exhibit mirror symmetry. Fig. 6.4E shows the histogram of twin thickness distribution in the printed nt-Cu pillar. A peak twin thickness of  $\sim 17 \text{ nm}$  was obtained for the selected grains, and the average twin thickness was  $27.0 \pm 17.9 \text{ nm}$ .

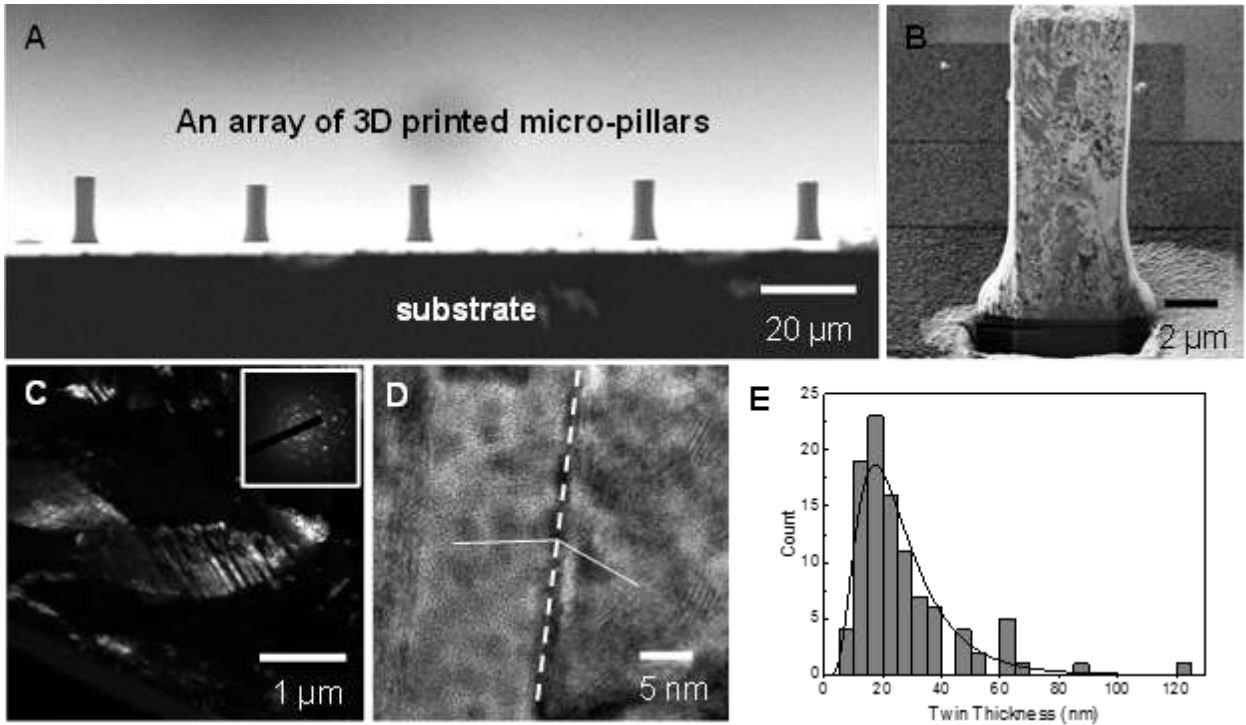


Figure 6.4. (A) An SEM image of an array of directly printed Cu micro-pillars using the L-PED process with a diameter distribution of  $4.6 \pm 0.08 \mu\text{m}$ . The micro-pillars were printed with  $T_{on}$  of 20 ms,  $T_{off}$  of 2 s and the peak current density of  $3.74 \pm 0.17 \text{ A/cm}^2$  at a deposition rate of 12 nm/s. The printing of each micro-pillar took about  $\sim 16$  minutes. (B) The micro-pillar was sectioned using FIB to reveal its internal structure. The deposited material is fully dense with no apparent porosity. The ion-channeling contrast image reveals the microstructure of the printed metal including the grain size and shape and existence of the twin boundaries. One of the columnar-shaped grains is delineated by dashed line. (C) Dark-field TEM image of the pillar printed by the L-PED process shows a typical grain with the corresponding diffraction pattern (inset), which reveals the nanocrystalline nanotwinned (nc-nt) structure. (D) HRTEM (high resolution TEM) image of a typical twin boundary shown by the dashed line. (E) Histogram of twin thickness distribution in the grains with peak at  $\sim 17$  nm.

#### 6.4.1 *In situ* Characterization

Mechanical properties of the micro-pillars printed by the L-PED process were characterized using *in situ* SEM micro-compression experiments using a nanoindenter with a specialized punch. Figure 6.5A and B show photographs of the nanoindenter and the substrate containing the 3D-printed micro-pillars *in situ* SEM. A conductive flat punch tip was employed as

the compression anvil. The conductive tip is required for *in situ* SEM experiments to avoid charging of the indenter tip by the electron beam. Experiments can be carried out under both load-control and displacement-control modes. The nanoindenter is intrinsically a load-controlled system, however a constant displacement rate can be achieved by a feedback control loop. Figure 6.5C shows micro-compression experiment *in situ* SEM on individual micro-pillars from an array of 3D-printed pillars using a conductive diamond flat punch tip with diameter of 50  $\mu\text{m}$ . In practice, such experiment can be automated for a large array of micro-pillars precisely 3D printed using the described AM process in regular distances.

A representative stress-strain response from one of the micro-pillars is shown in Figure 6.5D. The stress-strain response of each micro-pillar was calculated from the obtained load and displacement data, and the geometry of the micro-pillar. The true stress-strain was calculated based on the assumption of constant volume for the pillars during the experiments. The pillars exhibited near-perfect elasto-plastic behavior with no clear hardening and smooth flow stress. TBs act as barriers to dislocation, prevent rapid deformation process in nc-nt samples.

Figure 6.5D illustrates the average flow stress at 5% strain for the printed pillars. The flow stress is reported at 5% strain due to the fact that the yield point was not clear in such small-scale testing of the samples. The result indicates an average flow stress of  $701 \pm 45$  MPa for the nc-nt Cu pillars, which agrees with the previously reported strength for such microstructure<sup>39</sup>. In nc-nt Cu micro-pillars, the twin boundaries block the motion of dislocations, giving rise to such remarkable flow stress. This is noteworthy given that such micro-pillar was fabricated with an AM process.

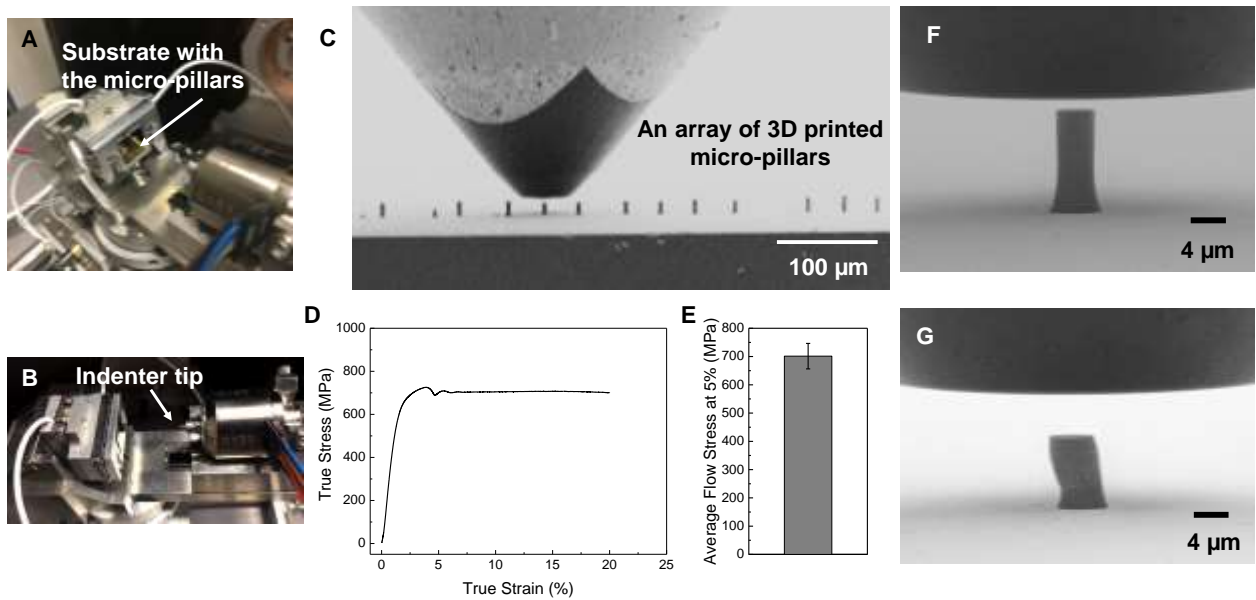


Figure 6.5. (A)-(B) Photographs of the nanoindenter and the substrate containing the 3D printed micro-pillars *in situ* SEM. (C) Micro-compression experiment *in situ* SEM on individual micro-pillars from an array of 3D-printed pillars using a flat punch tip. (D) A typical stress-strain response of nc-nt Cu (nanocrystalline-nanotwinned copper) micro-pillar printed using the L-PED process. (E) The average flow stress of the pillars at strain of 5%. (F)-(G) SEM images of the micro-pillar pre- and post-compression, respectively.

*In situ* SEM experiments enable real-time monitoring of the deformation of the material and its correlation with the stress-strain behavior. SEM images of the micro-pillar pre- and post-compression, respectively, are shown in Figs. 6.4F and G. The post-compression SEM image reveals localized plasticity in micro-pillar after deformation, supporting that the failure is of a ductile nature. Additionally, it can be observed that the pillar after compression still holds a strong adhesion with the substrate. This is very important, since a weak adhesion with the substrate can compromise obtained mechanical properties. The choice of proper substrate is important to ensure such strong adhesion in the AM process.

There have been several experimental reports on the tension and compression properties of nt-Cu metals fabricated with different methods.<sup>39, 40, 42, 55, 60, 65, 114-117</sup> The strength of L-PED nc-nt

Cu micro-pillars and other nt samples in the form of bulk solids, films, nanopillars or nanowires, is presented in Figure 6.6A. All reported nt structures exhibit high strength ranging from 230 to 2400 GPa. The obtained range of strength for the printed structures by the L-PED process is consistent with the recent reports. L-PED pillars with diameter of 4.6  $\mu\text{m}$  and 0.7  $\mu\text{m}$  exhibited an average flow stress of  $701 \pm 45$  MPa and  $962 \pm 26$  MPa, respectively. The difference in the strength of various samples can be attributed to their specific deformation mechanism caused by their microstructure and dislocations behavior. It is known that different synthesis techniques and different parameters produce different kinds of microstructure<sup>44</sup>, and the mechanical properties of nt materials are strongly influenced by the interaction of dislocations and TBs.

Previous studies revealed that the TBs block the propagation of slip bands similar to that of the grain boundaries in acting as obstacles to strain propagation<sup>44</sup>. For instance, the strength of the nt-Cu increases with decreasing the twin thickness following the Hall-Petch relationship, similar to that of grain refinement strengthening in nc metals. While samples with twin thickness of lower than 15 nm follow the inverse Hall-Petch relationship<sup>40</sup>. Also studies showed that the perpendicular orientation of TBs with respect to the loading direction results in more strengthening, and samples with orthogonal TB require additional applied stress to fail<sup>60,66</sup>. Other microstructural parameters such as grain size and texture affect the properties as well<sup>44</sup>.

Figure 6.6B presents more focused comparison of compression strength in L-PED nc-nt Cu micro-pillars and selected similar pillars fabricated with template-based electrodeposition and FIB milling. Interestingly, the strengths of L-PED samples are higher than those of their counterparts. In the template-based electrodeposited nanotwinned sample<sup>55</sup>, grains are equiaxed with the TBs inclined to the grain boundaries, while in the L-PED fabricated pillars, most grains

have the form of columns where the TBs are approximately perpendicular to the columnar axis. Therefore, the L-PED nanotwinned specimens, possessing a pronounced texture with  $\langle 111 \rangle$  planes located preferentially parallel to the substrate, exhibit higher strength. The FIB-milled pillars<sup>60</sup> with near equivalent nanocrystalline microstructure and twin orientations, exhibit slightly lower strength compared to the L-PED specimen. While this difference can be due to the slight dissimilarity in the microstructure of samples, it can also be attributed to the introduced damage into the material during the process. The results show that L-PED have capability of fabricating pristine controlled microstructure with no initial dislocation, with comparable mechanical properties to the bulk sample.<sup>54, 68</sup>

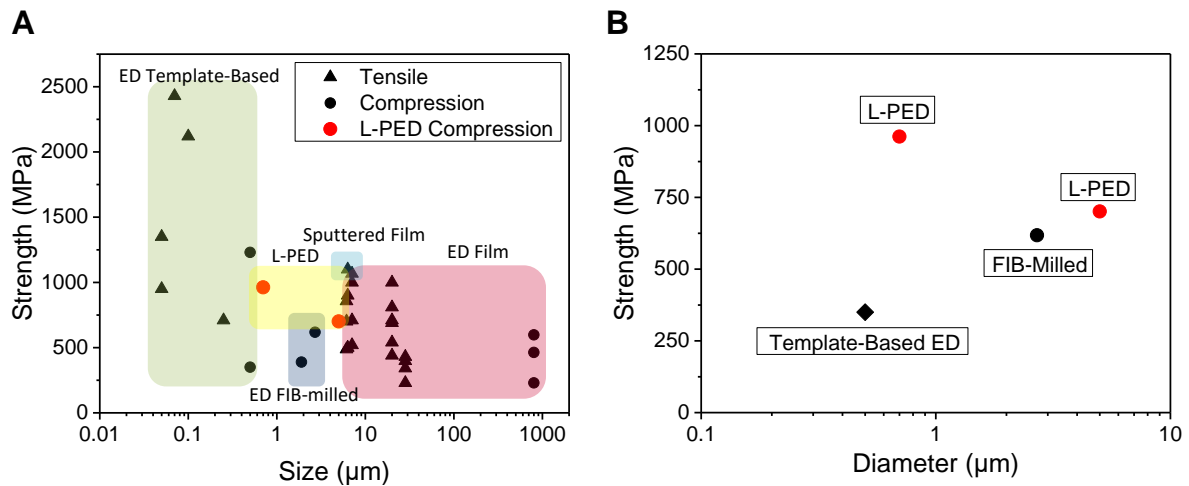


Figure 6.6. (A) Comparison of the strength of nanotwinned copper L-PED micro-pillars (red symbols) and other reported nanotwinned materials in the form of electrodeposited or sputtered bulk solids and films, or nanopillars fabricated using FIB milling or template patterning<sup>39, 40, 42, 55, 60, 65, 114-117</sup>. (B) Comparison of compression strength in L-PED nc-nt Cu micro-pillars and similar pillars fabricated by the template-based electrodeposition and FIB milling with near equivalent nanocrystalline microstructure and twin orientations.<sup>55, 60</sup>

The free-standing micro-pillar geometry is also attractive for characterization of electrical conductivity of the 3D-printed material. Electrical conductivity of the 3D-printed metal can be also

used as an indirect method for probing the microstructure of the metal. The electrical resistivity of the 3D printed micro-pillars was measured in situ SEM by a nanomanipulator. The image of the experimental setup is shown in Figure 6.7A. The conductive substrate on which the micro-pillars were deposited was used as the electric ground, while the tungsten probe was manipulated to measure the resistance of the pillar. The probing procedure is presented in Fig. 6.7B and C. First, the probe was tightly pressed on the top of the pillar to measure the total resistance ( $R_T$ ). The total resistance is consisted of the intrinsic resistance of the pillar ( $R_P$ ), the contact resistance, resistance of the circuitry, and resistance of the substrate ( $R_S$ ).

The acquired total resistance is shown in Figure 6.7D with the black line. Subsequently, the probe was placed on the bottom of the pillar to determine the sum of the contact resistance, circuitry resistance, and substrate resistance ( $R_S$ ), which is shown as the red line in Figure 6.7D. Assuming the resistances are in series, the resistance of the pillar ( $R_P$ ) was calculated by subtraction of  $R_S$  from  $R_T$ . Using the geometry of the micro-pillar obtained from the SEM images, the resistivity of the pillar can be calculated.  $\rho = R \cdot A / L$ , where  $R$  is the intrinsic resistance,  $A$  is the cross-sectional area, and  $L$  is the height of the micro-pillar. The results on the electrical characterization of nc-Cu pillars with an average diameter of  $\sim 700$  nm is presented in Fig. 6.7E. The pillars exhibit an average resistivity of  $16.14 \pm 3.90 \mu\Omega \cdot \text{cm}$ , which is close to the value for the bulk nc-Cu at room temperature <sup>39</sup>.

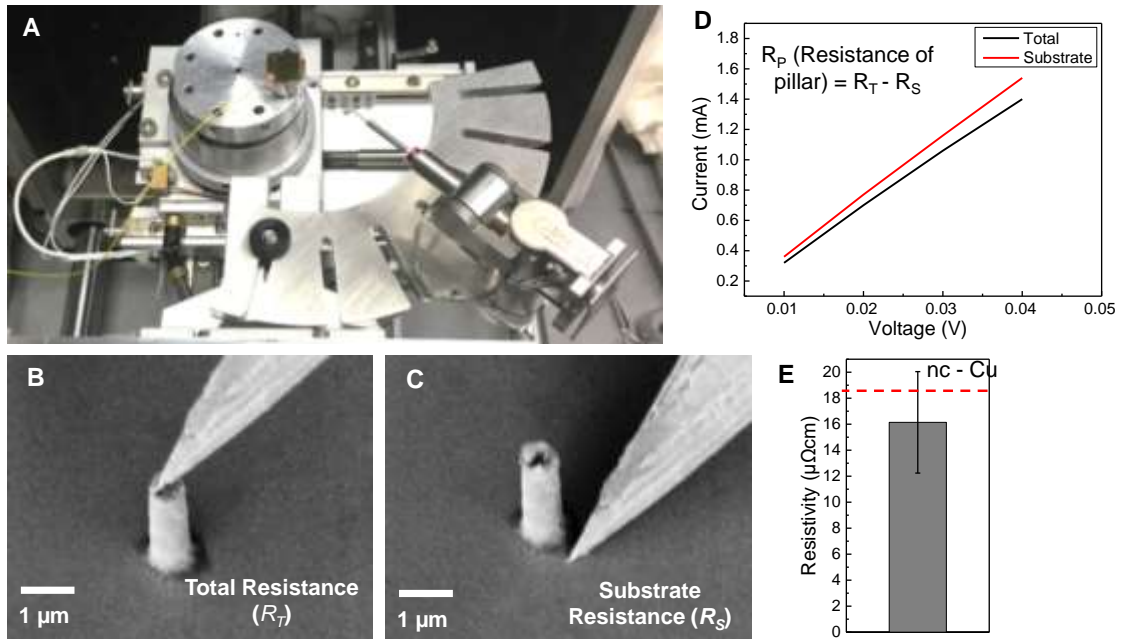


Figure 6.7. (A) The in situ SEM setup for characterization of electrical properties of the 3D-printed micro-pillars. (B)-(C) SEM images of the procedure for measurement of the electrical resistivity of a pillar with diameter of  $\sim 700$  nm. (D) A typical I-V response on the top and bottom of a single 3D-printed Cu micro-pillar. (E) The average calculated resistivity of the Cu micro-pillar.

## 6.5 Conclusions

An AM process based-on electrochemical plating, called localized pulsed electrodeposition (L-PED), was introduced that enables direct printing of nano/micro-pillars of metals and alloys micro-compression test specimens in room environment. The key contribution of the L-PED process is low-cost and high throughput fabrication of small scale test specimens with pristine microstructure and no initial dislocation in one single step in room environment. The L-PED process not only offers precise control over the size of the sample, but also allows control over the spatial microstructure of the deposited metal. The proposed method was demonstrated through fabrication and mechanical and electrical testing of nc-nt copper micro-pillars. The microstructure of a

selected representative pillar was investigated using high resolution FIB imaging system. Mechanical properties of the 3D-printed micro-pillars were characterized using *in situ* SEM micro-compression experiment. The printed nc-nt Cu pillars exhibited an average flow stress of  $701 \pm 45$  MPa at 5% strain. Additionally, electrical properties of the printed nc Cu pillars were investigated in situ SEM. The results showed an average resistivity of  $16.14 \pm 3.90$   $\mu\Omega$ .cm. While the L-PED as a unique microscale metal AM process can be attractive for various applications where fabrication of complex geometries are desirable, its combination with in situ characterization methods can provide high-throughput investigation of process – microstructure – property relationship for full understanding of mechanical behavior of metals and metal alloys at the small-scale.

## CHAPTER 7

### LARGE SCALE METAL 3D PRINTING USING LOCALIZED ELECTRODEPOSITION

#### 7.1 Introduction

Additive manufacturing (AM) is revolutionizing the way industry can design and fabricate components. The size of global market for 3D printing was about 6 billion dollars in 2015, and this value is likely to grow to nearly 50 billion dollars by 2025.<sup>118</sup> The 3D printing technologies continue to make inroads into various applications, including construction, aerospace, automotive, and the medical industries.

AM has been defined by the ASTM as a process of layer-by-layer assembly of materials to fabricate objects from a 3D model.<sup>119</sup> Whereas AM of polymeric and plastic materials is in a well-developed stage, there has been extensive research to advance AM techniques for metals. Among these methods, the techniques based on local fusion of metal powders, selective laser melting (SLM), and electron beam melting (EBM) are the most common methods which are commercially available.<sup>2</sup>

According to material feed stock and energy source, the existing commercial metal AM techniques can be classified into three main groups: (i) powder bed systems, (ii) powder feed systems, and (iii) wire feed systems.<sup>120</sup> In the powder bed systems, the powder is grouped across the work area. The electron beam or laser beam, as the source, delivers the energy to the surface of the bed and melts or sinters the powder. By adding new powder to the work area, and repeating the process a solid three dimensional geometry is created. This technique is capable of fabricating high resolution features while maintaining great dimensional control.<sup>120</sup>

In the powder feed systems, powders are transferred by a nozzle into the surface of interest, and a laser source melts one or multiple layers of the powder into the desired shape. Repeating the process results in a solid three dimensional object. This method is advantageous compared to other ones because of the fabrication of larger build volume and its ability to be used on actual components to refurbish the worn or damaged parts.<sup>120</sup> The energy source for wire feed systems can be electron and laser beam, and plasma arc. In this process, line of desired material is deposited layer by layer to form the solid geometry. This technique can be employed at higher deposition rate for large build volumes, but the final product requires more post-processing compared to the powder bed or powder fed systems.<sup>120</sup>

While metal AM enables manufacturing of the components that cannot be made with standard machining tools, currently the application of the existing methods is limited due to the high cost, structural defects, and inferior material properties. Therefore, there is need to develop a new low-cost 3D printing technique for metals at macroscale to improve the material performance. As demonstrated, the LED process is designed to fabricate high quality layer-by-layer micro/nanoscale metallic structures at room environment. Herein, the extension of the LED process to enable 3D printing of metals at larger scale is reported. This chapter provides a systematic overview of the process for fabrication of precise patterns on different conductive and nonconductive substrates with superior material properties which can compete with the conventional AM techniques.

## **7.2 Material and methods**

The large scale LED 3D printer system is shown schematically in Figure 7.1A. The system includes different components and subsystems including vibration isolation, motion control,

current measurement, flow control, and printing tool. The system is mounted on a tabletop mechanical vibration isolation platform (VIP100, Newport, Inc.). A mid-travel range three-axis linear translation stage with stepper motors (UTS150PP, Newport, Inc.) and a universal controller (Model XPS-Q6, Newport, Inc.) drives the printing process. The stages provide smooth and accurate positioning with minimum incremental motion of less than  $0.3\ \mu\text{m}$  and a travel range of 150 mm. The controller is connected to a computer, either running manually using a LABVIEW program or automatically through a G-Code program.

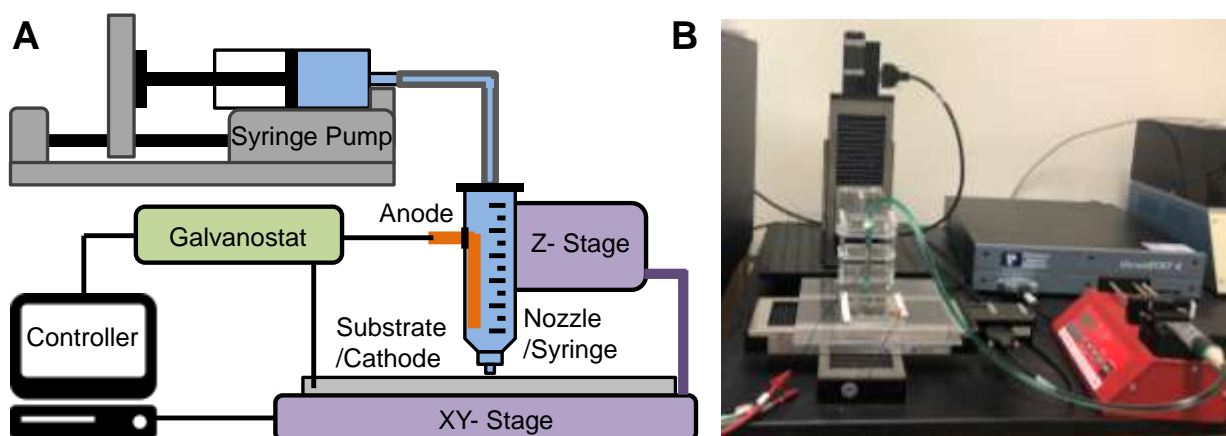


Figure 7.1. (A) The schematic of the LED setup for large scale printing. (B) Large scale LED metal 3D printer setup.

Commercially available plastic syringes with millimeter to sub-millimeter diameter dispensing nozzles were used as the working tool. The plastic syringe nozzles are cheap and reusable compared to conventional glass pipettes used in micro-scale LED process. Additionally, their flexibility in contact with the substrate in lateral movement prevents the tip breakage, and facilitate use of the LED process on non-flat surfaces. The syringe is filled with a solution of the metal of interest, which is connected to a syringe pump to provide sufficient back pressure to form a stable meniscus. It is noteworthy that due to the large diameter of the nozzle, the electrolyte flows

out without the control system, since the surface tension of the electrolyte cannot maintain the meniscus. The system pumps the electrolyte to the nozzle tip at a constant rate. At higher flow rate, the liquid bridge becomes unstable and the electrolyte flows out. At lower flow rate, the system cannot provide enough electrolyte and the meniscus breaks.

For printing Cu structures using this setup, commercially available acid copper plating electrolyte solution (Transene) was used. The substrates used in this study were glass slides and polyimide (PI) films coated with a thin layer of gold or copper (less than 30 nm), or 3D-printed electrically conductive polylactide (PLA). The substrate served as the working electrode. A copper wire was inserted and sealed in the syringe functioned as the counter electrode in the cell. A potentiostat/galvanostat (VersaSTAT 4, Princeton Applied Research) was employed to apply the electrical potential between the two electrodes and to control the electrodeposition process. The printer setup is presented in Figure 7.1B.

### **7.3 Results and discussion**

Several of the printed Cu patterns on different substrates are shown in Figure 7.2. The large scale LED process follows the same principle of microscale LED described in previous chapters. The electrodeposition is localized in a small liquid bridge formed between the nozzle tip and the substrate. The appropriate potential is applied between the electrodes, while the nozzle moves along the pre-defined path on the substrate surface and pulls the meniscus at a constant rate of 0.1 mm/s. Metal ions are deposited on the substrate during the process, and if the pattern is repeated, layer-by-layer structures can be fabricated.

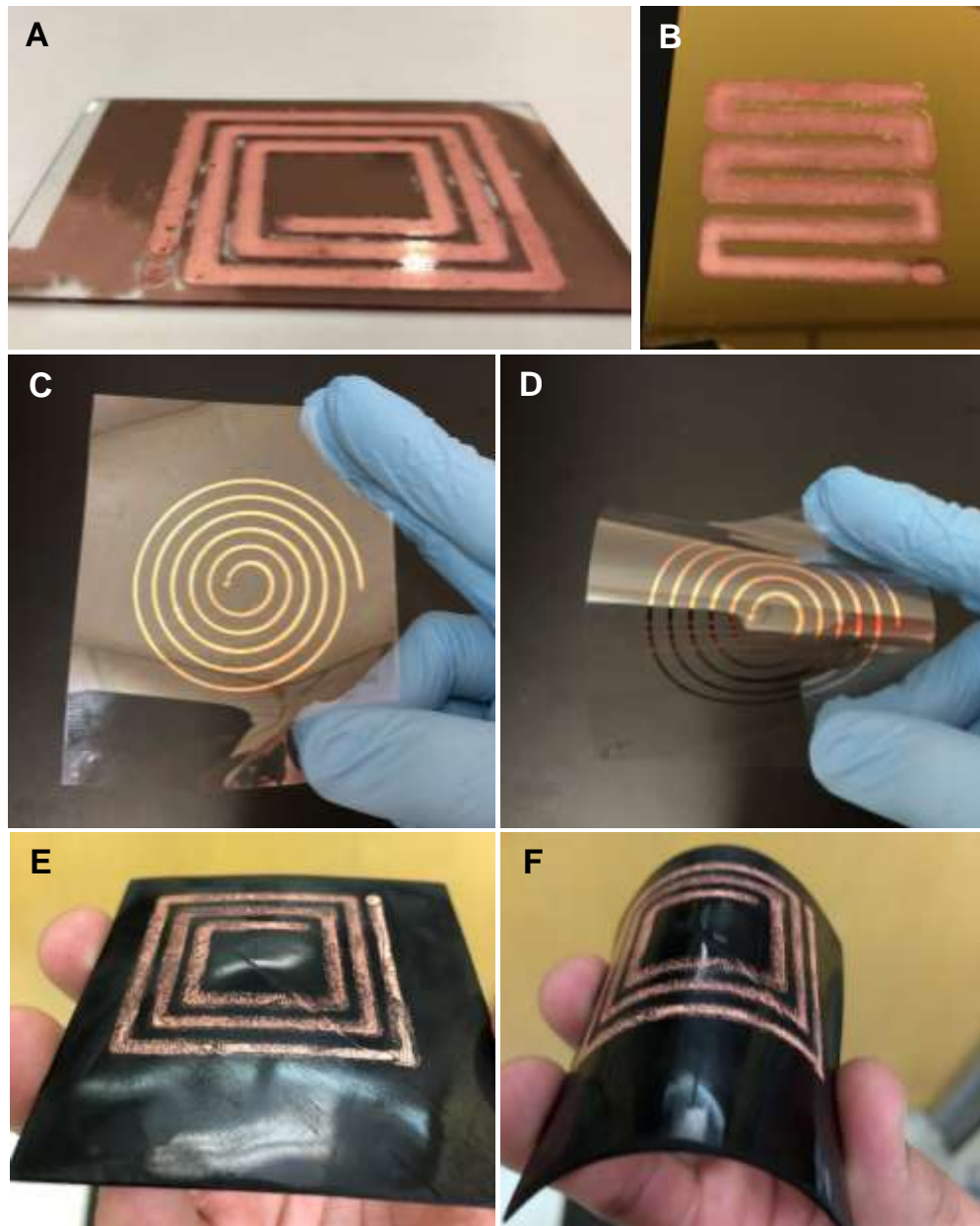


Figure 7.2. Images of several Cu patterns printed on (A) and (B) gold-coated glass slides, (C) (D) conductive PLA, and (E) and (F) PET film using large scale LED printing process.

Considering the differences in the size of the nozzles in large scale LED process and conventional LED process, the physics of electrodeposition is different between the two methods. As mentioned earlier, microscale LED is an evaporation driven process, and the evaporation of the

electrolyte from the meniscus is significant due to the high ratio of surface to volume of the meniscus. Therefore, high evaporation rate affects the ion transportation from the electrolyte to the cathode surface. However, in nozzles with larger diameter the surface to volume ratio of the liquid bridge is not high, and the evaporation rate is lower and does not assist the process. Hence, the large scale LED is comparable to the bulk level deposition in this matter.

The deposition rate of the process can be controlled by process parameters including the deposition mode, applied current density, and concentration of the electrolyte. In order to obtain the actual volumetric deposition rate of the process, a 20 mm single line was printed on gold-coated glass slide using a 4-mm diameter nozzle (Figure 7.3A). The printing was performed in galvanostatic mode with DC current density of  $\sim 32 \text{ mA/cm}^2$  and a nozzle speed of 0.1 mm/s. The syringe pump fed the electrolyte at a constant rate of 0.1  $\mu\text{L/s}$ . 200 layers were printed in  $\sim 11$  hours. The profile of the deposited line is obtained using a profilometer (Figure 7.3B and C). The volume of the deposited line is  $\sim 6.14 \text{ mm}^3$ . Therefore, the obtained volumetric deposition rate with such parameters is  $\sim 0.55 \text{ mm}^3/\text{hr}$ . The LED process parameters of the presented patterns were chosen after a set of experiments to obtain the optimal parameters in this scale. For instance, higher nozzle speed results in non-continuous deposition, and lower nozzle speed makes the printing process and volumetric deposition rate slower.

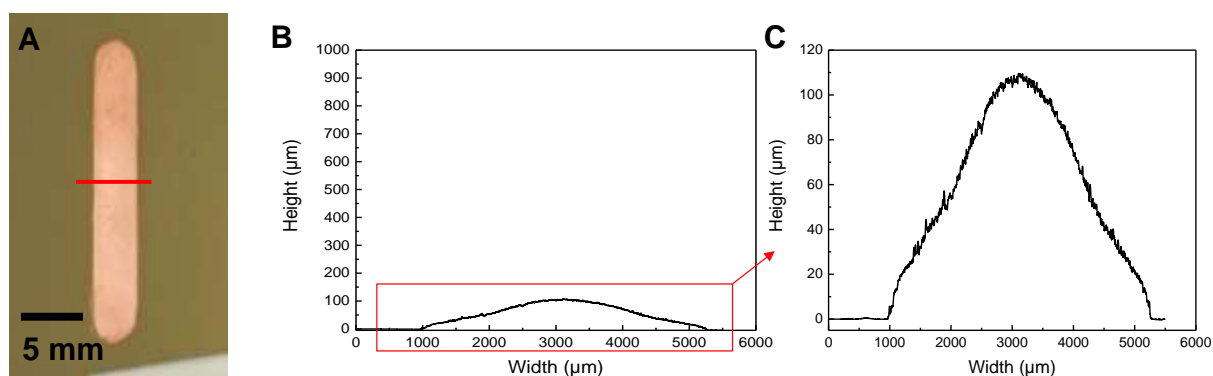


Figure 7.3. (A) A 200-layer copper line printed on a gold-coated glass slide using the LED process. (B) Profile of the printed structure (red line) obtained using the profilometer, and (C) the zoomed-in profile.

Figure 7.4 A-C presents SEM images of the printed line at different magnifications. The results show that high-quality Cu can be printed in 3D geometries with a smooth surface. The energy-dispersive X-ray spectroscopy (EDS) analysis of the printed pattern is presented in Figure 7.4D. The acquired spectra from Figure 7.4C exhibited pure Cu without significant amount of any impurities. The EDS results are presented in Table 7.1. Considering the room environment LED process, and the tendency of copper to oxidize, small amount of oxygen (0.3 Wt %) was present on the surface of both printed Cu pattern.

Table 7.1. Elemental analysis of the printed Cu obtained from EDS spectra.

Element	Wt %	At %
Cu	99.59	98.58
O	0.31	1.22
S	0.10	0.21

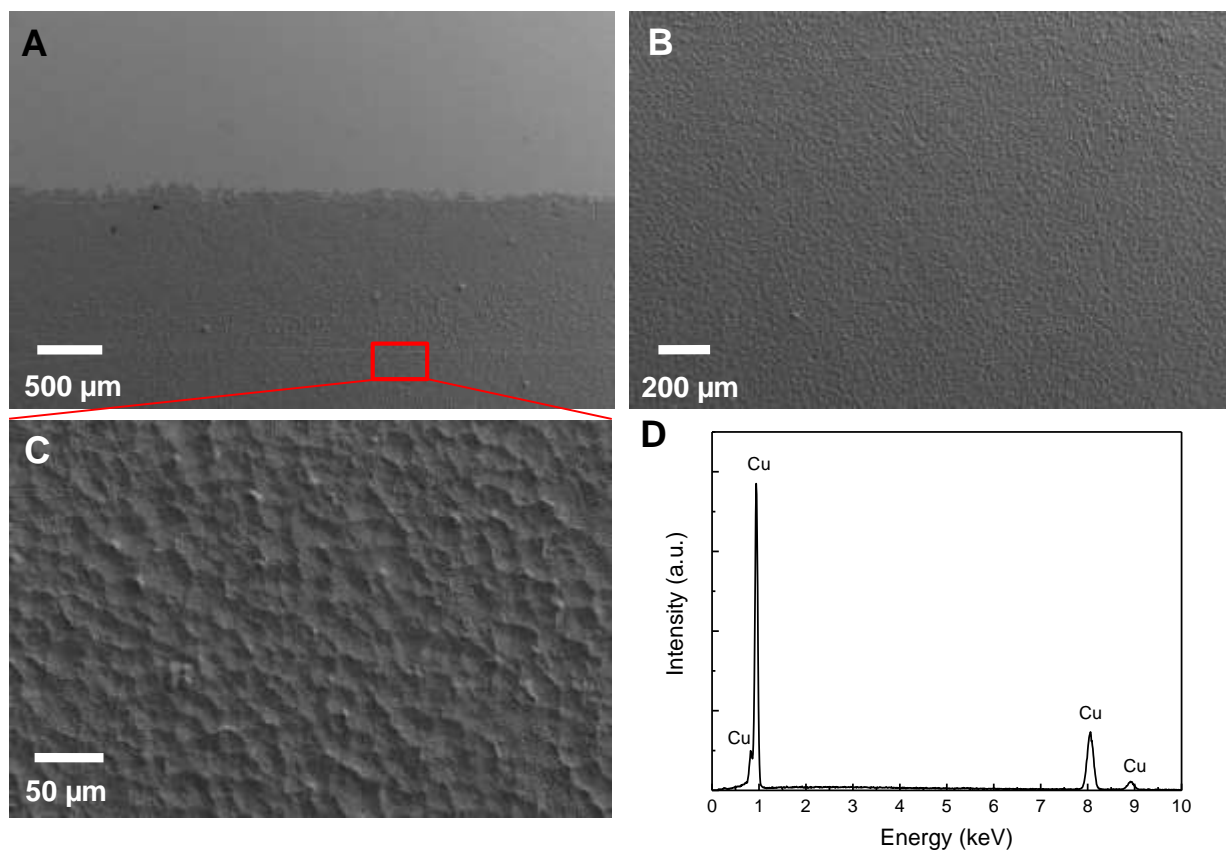


Figure 7.4. (A)–(C) SEM images of the printed Cu pattern and different magnifications. (D) Energy-dispersive X-ray spectroscopy (EDS) analysis of the deposited Cu. The spectra shows pure Cu deposition free of impurities.

It is known that the LED process is only achievable on conductive substrates.<sup>68</sup> However, in this work, an innovative process was implemented to achieve 3D printed metallic structures on non-conductive substrates. The process of printing on a non-conductive substrate is shown schematically in Figure 7.5A. Prior to printing, the substrate was coated with a thin layer of Cu (10-40 nm) as the working electrode. After printing the patterns with desired thickness on the substrate, the entire substrate was immersed into Cu etchant solution to etch the deposited thin layer. The etching time was set long enough to remove the thin deposited layer, however it was too short to etch the printed pattern. The Cu patterns on non-conductive glass slide after removal

of the conductive layer are presented in Figure 7.5 B and C. The adhesion of the printed layer to the substrate (PET film or glass) were good, and the patterns were stable under bending of the film.

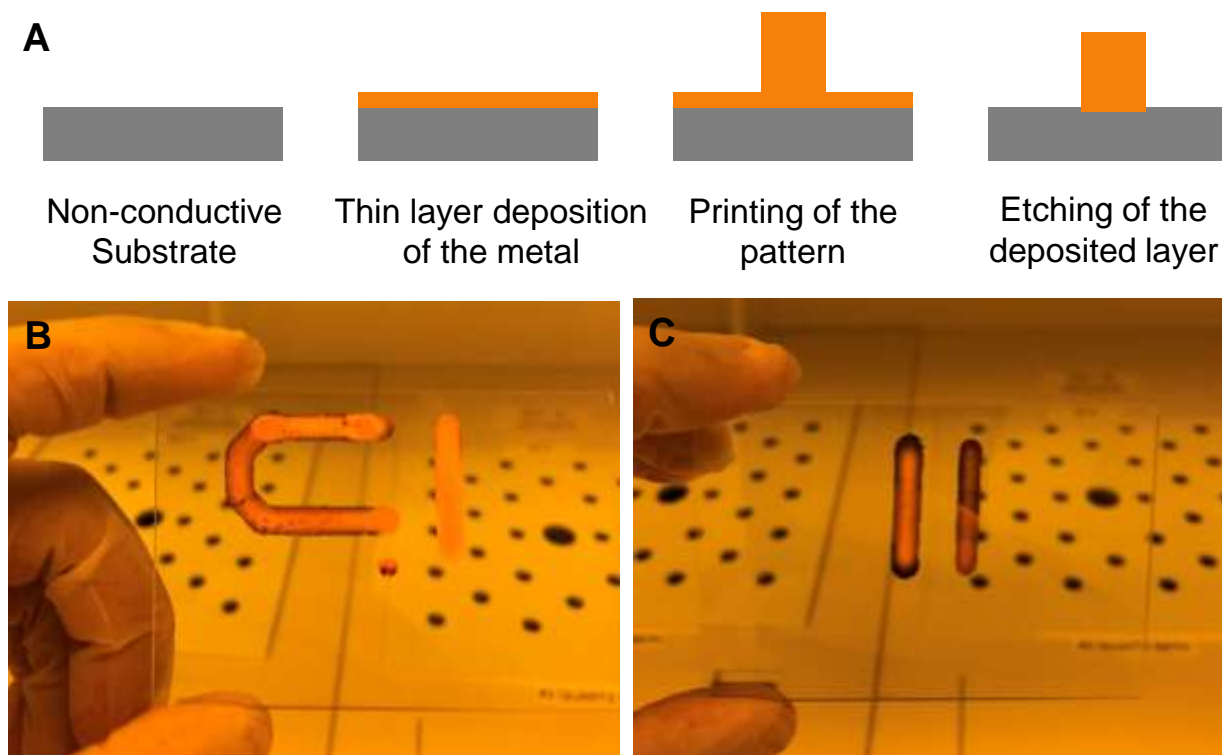


Figure 7.5. (A) The schematic of the process for printing patterns on a non-conductive substrate including thin layer deposition of the metal of interest as the cathode, printing the pattern, and etching of the thin layer. (B) and (C) The Cu patterns on a non-conductive glass slide after etching the conductive thin layer from the substrate.

The 3D printing of metallic structures, in particular on flexible substrates, are attractive for electrical applications. Electrical resistivity of the LED printed Cu was measured using an electrometer. Single lines were printed on non-conductive glass slide as described earlier. The resistance of the printed patterns were measured. The total resistant includes the resistance of the printed pattern and the thin film deposited under the printed layer. Assuming the resistances are in parallel, the electrical resistivity of samples were calculated considering the geometry of the printed pattern after deduction of electrical resistivity of the conductive coating. The resistivity of

the printed Cu structure was  $11 \mu\Omega\cdot\text{cm}$ . The resistivity of the line was calculated using  $\rho = R \cdot A/L$ , where  $R$  is the intrinsic resistance,  $A$  is the cross-sectional area, and  $L$  is the length of the line. It is noteworthy that the resistivity value for the bulk nano-crystalline Cu at room temperature is  $18 \mu\Omega\cdot\text{cm}$ .

Application of the LED process is demonstrated by fabrication of rectangular planar coiled RFID antenna. Figure 7.6 b shows the patterned antenna on a glass slide with a  $100 \text{ pF}$  capacitor and a low current LED connected in parallel. This is a three-turn  $45 \text{ mm}$  by  $40 \text{ mm}$  antenna with turn width of  $3 \text{ mm}$  and path separation width of  $2 \text{ mm}$ . The inductance of the antenna was  $\sim 400 \text{ nH}$ . The tag resistance was  $2 \Omega$ , and the voltage harvested at a distance of  $1 \text{ cm}$  was  $\sim 5 \text{ mV}$ . By bringing the RFID reader (SM132, SONMICRO) close to the tag, the connected LED lights up (Figure 7.6c).

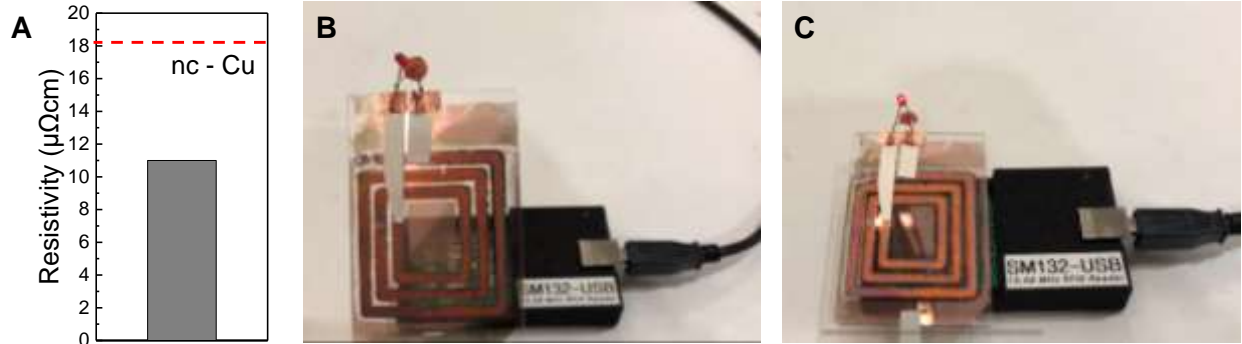


Figure 7.6. (A) Resistivity of the printed Cu line. (B) A RFID tag printed on a glass slide connected to a capacitance and a LED light. (C) By approaching the RFID reader, the LED connected to the printed tag lights up.

#### 7.4 Conclusion

In summary, large scale printing of Cu patterns on different substrates was demonstrated using an additive manufacturing process termed as the LED process. The fabricated patterns

exhibited high quality, with great adhesion to the substrate. An innovative technique was introduced for printing of metallic structures on non-conductive substrates. The electrical resistivity of the printed Cu structures was comparable with bulk nano-crystalline Cu. The LED process can be extended to more complex geometries with in situ control over the microstructure. Further studies are needed to enable tuning of material properties of the printed patterns, and extension of the process to other metals and alloys.

## CHAPTER 8

### CONCLUSIONS AND FUTURE WORK

In this dissertation, a novel microscale metal additive manufacturing process based on localized electrodeposition process in ambient environment was introduced and investigated. This capability will be attractive for various applications in nanotechnology, in particular for 3D electronics and sensors. The following conclusions were made based on this research:

- The localized pulsed electrodeposition (L-PED) enables printing of high quality Cu in 3D geometries with nanocrystalline-nanotwinned (nc-nt) microstructure with remarkable average yield strength of 960 MPa. Additionally, nc-Cu was printed using the same process, under DC electrodepositing with an average yield strength of 656 MPa.
- The size of the printed structures is controlled by the size and the withdrawal speed of the nozzle. By increasing the withdrawal speed of the nozzle within a stable range, the meniscus stretches which results in finer features. Also, the deposition rate of the wire depends on many factors including: the applied potential, electrolyte concentration, and environmental humidity.
- The process offers control over the grain and twin densities and orientations by controlling the process parameters in both DC-ED and PED methods. The average current density is the most critical input parameter for the control of the microstructure. Increase in the average current density and accordingly the deposition rate results in the increase in the density of the twin boundaries and their alignment within the grains, and transition to columnar grains from randomly oriented grains. The results of the *in situ* SEM nanomechanical experiments show that such change in the microstructure directly affects the mechanical properties of the 3D-printed metal.

- The investigation on thermal stability and mechanical properties of 3D printed micro-scale nt-Cu interconnects showed the capability of L-PED to enhance the materials performance and avoid the void formation at elevated temperatures. The nt-Cu interconnects exhibited high compression strength at high temperature of 450 °C, which indicates the high thermal stability of such 3D printed structures. This research can yield important advancement in 3D printing of electronics, and may provide considerable value for use in Nano technological applications.
- The L-PED process in combination with *in situ* characterization methods enables low-cost and high-throughput investigation of process – microstructure – property relationship by direct printing of small scale test specimens with pristine microstructure and no initial dislocation in one single step in room environment.
- Large scale LED is developed for printing of high quality metallic patterns on different substrates with good adhesion to the substrate. An innovative technique is introduced for LED printing on non-conductive substrates.

## 8.1 Outlook

There are some remarkable topics beyond the work in this dissertation that could be considered as future research. This work was focused on feasibility of using the localized electrodeposition as an advanced microscale AM method for fabrication of metals in electronics by printing Cu as a representative metal. However, this technique can be extended to other type of materials and alloys that can be electrodeposited. Two example of preliminary works is presented as following:

### 8.1.1 Electrodeposition of Nickel and Nickel Alloys

Nickel and Nickel alloys are one of the most attractive metals for a wide variety of structural and electrical applications due to their high corrosion resistant, heat resistance, and electrical conductivity. In spite of extensive research on bulk electrodeposition of Ni, AM of this metal at both small scale and large scale is very limited. Therefore, I started additive manufacturing of Ni using the LED method. Figure 8.1 presents some of the preliminary works on 3D printing of Ni and Cu/Ni. A pure Ni micro-pillar with 8.8  $\mu\text{m}$  diameter and a 40-layer circular pattern were printed using a glass micropipette nozzle with 10  $\mu\text{m}$  diameter (Figure 8.1A and B). In this study, commercial Watts solution (Trancene) was used as the electrolyte, and a copper wire inserted into the nozzle served as the anode. The EDS results show high purity of Ni with only negligible amount (0.5 Wt %) of Oxygen.

1 M of  $\text{CuSO}_4$  was added to the Ni solution in order to print alloy of Cu/Ni. Figure 8.1C presents lines of 80  $\mu\text{m}$  printed at two different conditions. The first one printed applying -0.2 V and the second one printed at voltage of -0.8 V. The EDS results show significant difference in the lines composition. The first line deposited at lower voltage exhibited 0.13 ratio of Ni-to-Cu, while the line deposited at higher voltage revealed the ratio of 1.83. It is in agreement with the fact that reduction of Cu occurs at lower potential compared to Ni, and increasing the potential results in more deposition of Ni during printing. Continuous deposition of lines printed at different applied potentials exhibited similar results (Figure 8.1D). Increasing the applied potential lead to inclusion of more Ni into printed patterns.

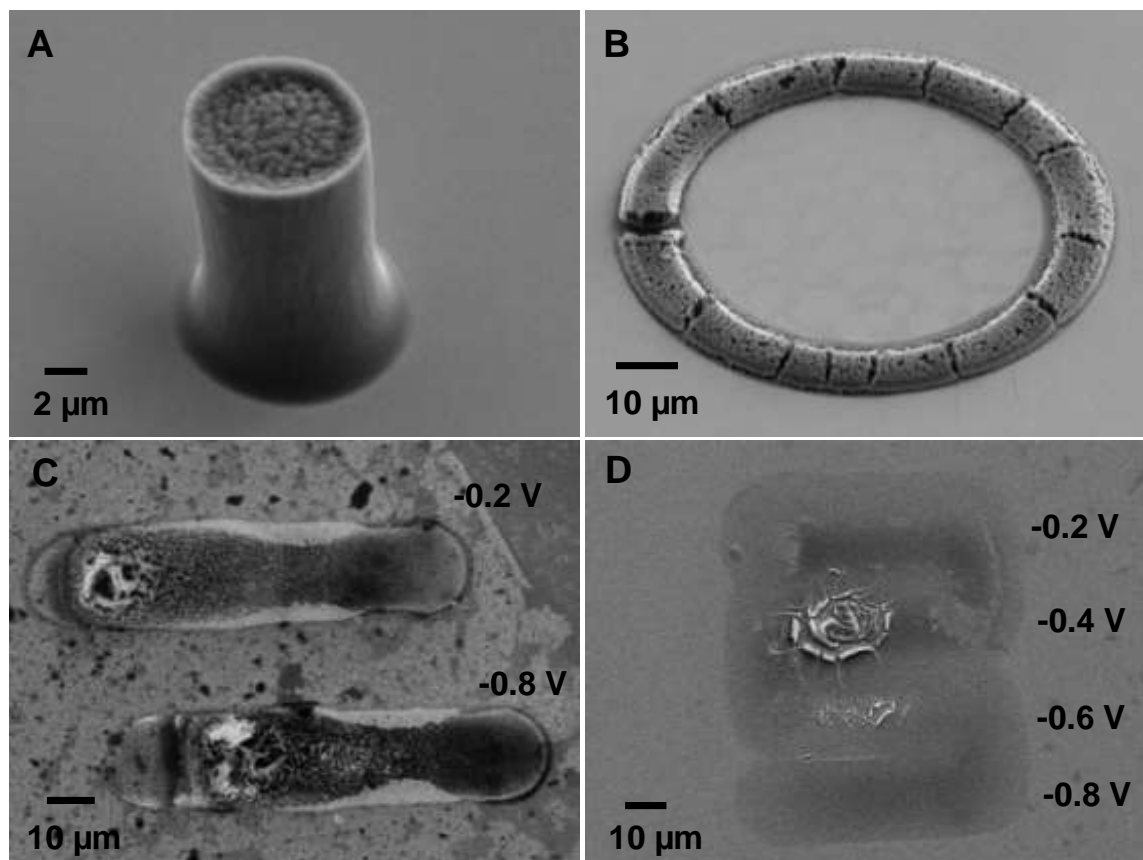


Figure 8.1. Printed pure Ni (A) micro-pillar with diameter of 8.8 μm and (B) 40-layer circular pattern using the LED process. (C) and (D) Printing Cu/Ni alloy lines using different potentials. Higher potential results in increased volume deposition and inclusion of more Ni in the printed structures.

### 8.1.2 Metal matrix composites

There is a major effort for tailoring material properties in composites in order to meet desired specifications in manufacturing. Metal-matrix composites (MMC) made by electrochemical codeposition of particles with metal enable reliable cost-effective enhancement of tribological and mechanical properties.<sup>121, 122</sup> Particles with wide range of size, from tens of nanometers to hundreds of microns, and different shapes can be incorporated during metal deposition. First the charged particles are formed due to absorption of ions and surfactant on their

surface, and transported towards the cathode surface by convection. Then, the particles are physically entrapped into the growing metal matrix.<sup>121</sup> The desired composite structure can be achieved depending on various factors, including the particles' concentration, type, size, etc., electrolyte's concentration, additives, temperature, pH, current density, the flow during electroplating, and type and size of the electrode.<sup>121</sup>

Figure 8.2 shows the preliminary results on 3D printing of MMC using the LED process. In this study, the electrolyte was composed of 100 mM CuSO<sub>4</sub> and 1M H<sub>2</sub>SO<sub>4</sub> with addition of 2 g/L  $\gamma$ -Al<sub>2</sub>O<sub>3</sub> having an average particle diameter of 20 nm or Silicon Carbide (SiC) with an average particle diameter of 40 nm (Skyspring Nanomaterials). Figure 8.2A presents layer-by-layer printing of Cu with inclusion of Alumina particles, and Figure 8.2B exhibits a Cu micro-pillar with inclusion of SiC. However, the EDS results revealed that the percentage of particle inclusion in the 3D printed structure is very low (<1%). A new solution with the same characteristics but higher molarity of 1 M CuSO<sub>4</sub> was used for large scale LED printing and bulk electroplating with and without agitation. The results for large scale LED printing was similar to the small scale, however the percentage of inclusion was significantly higher in the case of regular bulk plating with agitation (>7.5%). The result shows the importance of flow and agitation during printing process for inclusion of the particles. Therefore, more particles can be incorporated in metal matrix composites with enhancing the convection in the LED process. Increasing the flow in large scale LED and increasing the evaporation rate by decreasing the humidity in small scale may play an important role as an alternative to the agitation in bulk process.

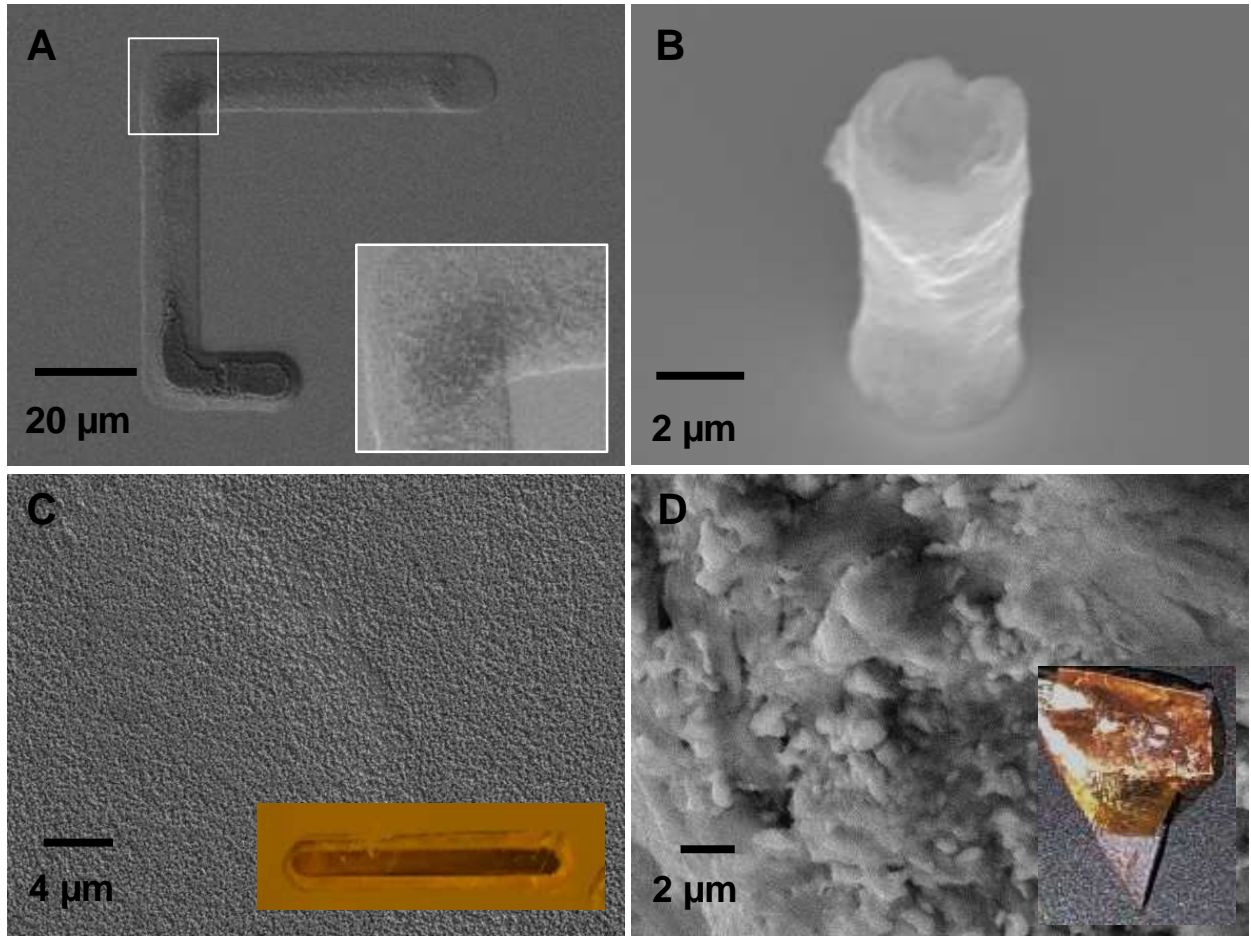


Figure 8.2. SEM images of (A) 3D printed layer-by-layer Alumina-Cu composite and (B) micro-pillar SiC-Cu composite using micro-scale LED process. SEM micrographs of (C) Alumina-Cu composite line (inset) printed by the large scale LED and (D) Alumina-Cu composite electroplated in bulk with agitation. The result show better inclusion of particles at the bulk level with agitation.

## REFERENCES

1. Hu, J.; Yu, M.-F. *Science* **2010**, 329, (5989), 313-316.
2. Hirt, L.; Reiser, A.; Spolenak, R.; Zambelli, T. *Adv. Mater.* **2017**.
3. Uchic, M. D.; Shade, P. A.; Dimiduk, D. M. *Annual Review of Materials Research* **2009**, 39, (1), 361-386.
4. Kiener, D.; Motz, C.; Rester, M.; Jenko, M.; Dehm, G. *Materials Science and Engineering: A* **2007**, 459, (1-2), 262-272.
5. Greer, J. R.; Oliver, W. C.; Nix, W. D. *Acta Materialia* **2005**, 53, (6), 1821-1830.
6. El-Awady, J. A.; Woodward, C.; Dimiduk, D. M.; Ghoniem, N. M. *Physical Review B* **2009**, 80, (10).
7. Shim, S.; Bei, H.; Miller, M. K.; Pharr, G. M.; George, E. P. *Acta Materialia* **2009**, 57, (2), 503-510.
8. Melchels, F. P.; Feijen, J.; Grijpma, D. W. *Biomaterials* **2010**, 31, (24), 6121-30.
9. Zeeshan, M. A.; Grisch, R.; Pellicer, E.; Sivaraman, K. M.; Peyer, K. E.; Sort, J.; Özkale, B.; Sakar, M. S.; Nelson, B. J.; Pané, S. *Small* **2014**, 10, (7), 1284-1288.
10. Burek, M. J.; Greer, J. R. *Nano Lett* **2010**, 10, (1), 69-76.
11. Geissler, M.; Xia, Y. *Adv. Mater.* **2004**, 16, (15), 1249-1269.
12. Seol, S. K.; Kim, D.; Lee, S.; Kim, J. H.; Chang, W. S.; Kim, J. T. *Small* **2015**, 11, (32), 3896-902.
13. An, B. W.; Kim, K.; Lee, H.; Kim, S. Y.; Shim, Y.; Lee, D. Y.; Song, J. Y.; Park, J. U. *Adv. Mater.* **2015**, 27, (29), 4322-8.
14. Suryavanshi, A. P.; Yu, M.-F. *Applied Physics Letters* **2006**, 88, (8), 083103.
15. Hirt, L.; Ihle, S.; Pan, Z.; Dorwling-Carter, L.; Reiser, A.; Wheeler, J. M.; Spolenak, R.; Voros, J.; Zambelli, T. *Adv. Mater.* **2016**, 28, (12), 2311-5.
16. Momotenko, D.; Page, A.; Adobes-Vidal, M.; Unwin, P. R. *ACS Nano* **2016**, 10, (9), 8871-8.
17. Ahn, B. Y.; Duoss, E. B.; Motala, M. J.; Guo, X.; Park, S.-I.; Xiong, Y.; Yoon, J.; Nuzzo, R. G.; Rogers, J. A.; Lewis, J. A. *Science* **2009**, 323, (5921), 1590-1593.
18. Onses, M. S.; Sutanto, E.; Ferreira, P. M.; Alleyne, A. G.; Rogers, J. A. *Small* **2015**, 11, (34), 4237-66.
19. Galliker, P.; Schneider, J.; Eghlidi, H.; Kress, S.; Sandoghdar, V.; Poulikakos, D. *Nature communications* **2012**, 3, 890.
20. Takai, T.; Nakao, H.; Iwata, F. *Optics Express* **2014**, 22, (23), 28109-28117.

21. Wang, J.; Auyeung, R. C.; Kim, H.; Charipar, N. A.; Pique, A. *Adv. Mater.* **2010**, 22, (40), 4462-6.
22. Zenou, M.; Sa'ar, A.; Kotler, Z. *Scientific reports* **2015**, 5, 17265.
23. Blasco, E.; Muller, J.; Muller, P.; Trouillet, V.; Schon, M.; Scherer, T.; Barner-Kowollik, C.; Wegener, M. *Adv. Mater.* **2016**, 28, (18), 3592-5.
24. Cao, Y. Y.; Takeyasu, N.; Tanaka, T.; Duan, X. M.; Kawata, S. *Small* **2009**, 5, (10), 1144-8.
25. Utke, I.; Hoffmann, P.; Melngailis, J. *Journal of Vacuum Science & Technology B: Microelectronics and Nanometer Structures Processing, Measurement, and Phenomena* **2008**, 26, (4), 1197-1276.
26. Lewis, J. A. *Advanced Functional Materials* **2006**, 16, (17), 2193-2204.
27. Skylar-Scott, M. A.; Gunasekaran, S.; Lewis, J. A. *Proc Natl Acad Sci U S A* **2016**, 113, (22), 6137-42.
28. Suryavanshi, A. P.; Yu, M.-F. *Nanotechnology* **2007**, 18, (10), 105305.
29. McKelvey, K.; O'Connell, M. A.; Unwin, P. R. *Chem Commun (Camb)* **2013**, 49, (29), 2986-8.
30. Morsali, S.; Daryadel, S.; Zhou, Z.; Behroozfar, A.; Qian, D.; Minary-Jolandan, M. *J. Appl. Phys.* **2017**, 121, (2), 024903.
31. Morsali, S.; Daryadel, S.; Zhou, Z.; Behroozfar, A.; Baniasadi, M.; Moreno, S.; Qian, D.; Minary-Jolandan, M. *J. Appl. Phys.* **2017**, 121, (21), 214305.
32. Paunovic, M.; Schlesinger, M., Overview. In *Fundamentals of Electrochemical Deposition*, John Wiley & Sons, Inc.: 2006; pp 1-6.
33. Tatarchenko, V. A.; Uspenski, V. S.; Tatarchenko, E. V.; Nabot, J. P.; Duffar, T.; Roux, B. *Journal of Crystal Growth* **1997**, 180, (3), 615-626.
34. Gennes, P.-G. d.; Brochard-Wyart, F.; Quere, D., *Capillarity and Wetting Phenomena*. Springer-Verlag New York: 2004.
35. Tatarchenko, V. A., *Shaped Crystal Growth*. Springer Netherlands: 2013.
36. Ghasemi, H.; Ward, C. A. *The Journal of Physical Chemistry C* **2010**, 114, (11), 5088-5100.
37. Fisher, J. S.; Kottke, P. A.; Kim, S.; Fedorov, A. G. *Nano Lett* **2015**, 15, (12), 8385-8391.
38. Bard, A. J.; Faulkner, L. R.; John, W.; Sons, *Electrochemical methods : fundamentals and applications*. John Wiley & Sons: Hoboken, 2007.
39. Lu, L.; Shen, Y.; Chen, X.; Qian, L.; Lu, K. *Science* **2004**, 304, (5669), 422-426.
40. Lu, L.; Chen, X.; Huang, X.; Lu, K. *Science* **2009**, 323, (5914), 607-610.
41. Lu, K. *Nat. Rev. Mater.* **2016**, 1, (5), 16019.

42. Jang, D.; Li, X.; Gao, H.; Greer, J. R. *Nature nanotechnology* **2012**, 7, (9), 594-601.
43. Li, X.; Wei, Y.; Lu, L.; Lu, K.; Gao, H. *Nature* **2010**, 464, (7290), 877-880.
44. Ovid'ko, I. A.; Sheinerman, A. G. *Rev. Adv. Mater. Sci.* **2016**, 44, 1-25.
45. Sansoz, F.; Lu, K.; Zhu, T.; Misra, A. *MRS Bulletin* **2016**, 41, (04), 292-297.
46. Bufford, D. C.; Wang, Y. M.; Liu, Y.; Lu, L. *MRS Bulletin* **2016**, 41, (04), 286-291.
47. Hirt, L.; Reiser, A.; Spolenak, R.; Zambelli, T. *Advanced materials* **2017**.
48. Hasegawa, M.; Mieszala, M.; Zhang, Y.; Erni, R.; Michler, J.; Philippe, L. *Electrochimica Acta* **2015**, 178, 458-467.
49. Xu, D.; Kwan, W. L.; Chen, K.; Zhang, X.; Ozoliņš, V.; Tu, K. N. *Applied Physics Letters* **2007**, 91, (25), 254105.
50. Xu, D.; Sriram, V.; Ozolins, V.; Yang, J.-M.; Tu, K. N.; Stafford, G. R.; Beauchamp, C. *Journal of Applied Physics* **2009**, 105, (2), 023521.
51. Cheng, G.; Li, H.; Xu, G.; Gai, W.; Luo, L. *Scientific reports* **2017**, 7, (1), 12393.
52. Pearson, T.; Dennis J, K. *Transactions of the Institute of Metal Finishing* **1991**, 69, 75-79.
53. Chandrasekar, M. S.; Pushpavanam, M. *Electrochimica Acta* **2008**, 53, (8), 3313-3322.
54. Behroozfar, A.; Daryadel, S.; Morsali, S. R.; Moreno, S.; Baniyasi, M.; Bernal Rodrigo, A.; Minary-Jolandan, M. *Advanced materials* **2017**, 30, (4), 1705107.
55. Jang, D.; Cai, C.; Greer, J. R. *Nano Lett* **2011**, 11, (4), 1743-6.
56. Champion, Y.; Langlois, C.; Guérin-Mailly, S.; Langlois, P.; Bonnentien, J.-L.; Hÿtch, M. *J. Science* **2003**, 300, (5617), 310-311.
57. Wu, Z. X.; Zhang, Y. W.; Jhon, M. H.; Greer, J. R.; Srolovitz, D. J. *Acta Materialia* **2013**, 61, (6), 1831-1842.
58. Kiener, D.; Motz, C.; Schöberl, T.; Jenko, M.; Dehm, G. *Advanced Engineering Materials* **2006**, 8, (11), 1119-1125.
59. Jennings, A. T.; Li, J.; Greer, J. R. *Acta Materialia* **2011**, 59, (14), 5627-5637.
60. Mieszala, M.; Guillonneau, G.; Hasegawa, M.; Raghavan, R.; Wheeler, J. M.; Mischler, S.; Michler, J.; Philippe, L. *Nanoscale* **2016**, 8, (35), 15999-6004.
61. Oliver, W. C.; Pharr, G. M. *Journal of Materials Research* **2004**, 19, (1), 3-20.
62. Oliver, W. C.; Pharr, G. M. *Journal of Materials Research* **1992**, 7, (6), 1564-1583.
63. Choi, I.-C.; Kim, Y.-J.; Wang, Y. M.; Ramamurty, U.; Jang, J.-i. *Acta Materialia* **2013**, 61, (19), 7313-7323.
64. Bezares, J.; Jiao, S.; Liu, Y.; Bufford, D.; Lu, L.; Zhang, X.; Kulkarni, Y.; Asaro, R. J. *Acta Materialia* **2012**, 60, (11), 4623-4635.

65. Lu, L.; Schwaiger, R.; Shan, Z. W.; Dao, M.; Lu, K.; Suresh, S. *Acta Materialia* **2005**, 53, (7), 2169-2179.
66. Ye, J. C.; Wang, Y. M.; Barbee, T. W.; Hamza, A. V. *Applied Physics Letters* **2012**, 100, (26), 261912.
67. Luca, H.; Stephan, I.; Zhijian, P.; Livie, D.-C.; Alain, R.; M., W. J.; Ralph, S.; János, V.; Tomaso, Z. *Advanced Materials* **2016**, 28, (12), 2311-2315.
68. Daryadel, S.; Behroozfar, A.; Morsali, S. R.; Moreno, S.; Baniasadi, M.; Bykova, J.; Bernal, R. A.; Minary-Jolandan, M. *Nano Letters* **2018**, 18, (1), 208-214.
69. Morsali, S.; Daryadel, S.; Zhou, Z.; Behroozfar, A.; Baniasadi, M.; Moreno, S.; Qian, D.; Minary-Jolandan, M. *Journal of Applied Physics* **2017**, 121, (21), 214305.
70. Morsali, S.; Daryadel, S.; Zhou, Z.; Behroozfar, A.; Qian, D.; Minary-Jolandan, M. *Journal of Applied Physics* **2017**, 121, (2), 024903.
71. Marro, J. B.; Darroudi, T.; Okoro, C. A.; Obeng, Y. S.; Richardson, K. C. *Thin solid films* **2017**, 621, 91-97.
72. Cui, B. Z.; Han, K.; Xin, Y.; Waryoba, D. R.; Mbaruku, A. L. *Acta Materialia* **2007**, 55, (13), 4429-4438.
73. Lui, G.-T.; Chen, D.; Kuo, J.-C. *Journal of Physics D: Applied Physics* **2009**, 42, (21), 215410.
74. Lin, Y. W.; Kuo, J. C.; Lui, K. T.; Chen, D. *Materials Science Forum* **2010**, 638-642, 2841-2845.
75. Natter, H.; Hempelmann, R. *The Journal of Physical Chemistry* **1996**, 100, (50), 19525-19532.
76. Puipe, J. C.; Leaman, F.; American, E.; Surface Finishers Society, U. h. b. g. c. b. i. j., *Theory and Practice of Pulse Plating*. American Electroplaters and Surface Finishers Society: 1986.
77. Dini Jack, W.; Snyder Dexter, D. *Modern Electroplating* **2011**.
78. Wang, H.; Cheng, P.; Wang, H.; Liu, R.; Sun, L.; Rao, Q.; Wang, Z.; Gu, T.; Ding, G. *Materials Characterization* **2015**, 109, 164-172.
79. Petch, N. J. *The Journal of the Iron and Steel Institute* **1953**, 173, 25.
80. Hall, E. O. *Proceedings of the Physical Society. Section B* **1951**, 64, (9), 742.
81. Zhang, X.; Misra, A. *Scripta Materialia* **2012**, 66, (11), 860-865.
82. Anderoglu, O.; Misra, A.; Wang, H.; Zhang, X. *Journal of Applied Physics* **2008**, 103, (9), 094322.
83. Gertsman, V. Y.; Birringer, R. *Scripta Metallurgica et Materialia* **1994**, 30, (5), 577-581.
84. Alimadadi, H.; Fanta, A. B.; Akiyoshi, R.; Kasama, T.; Rollett, A. D.; Somers, M. A. J.; Pantleon, K. *Materials & Design* **2018**, 151, 60-73.

85. Zhao, Y.; Furnish, T. A.; Kassner, M. E.; Hodge, A. M. *Journal of Materials Research* **2012**, *27*, (24), 3049-3057.
86. LaGrange, T.; Reed, B. W.; Wall, M.; Mason, J.; Barbee, T.; Kumar, M. *Applied Physics Letters* **2013**, *102*, (1), 011905.
87. Park, H.; Hwang, S.-J.; Joo, Y.-C. *Acta Materialia* **2004**, *52*, (8), 2435-2440.
88. Du, S.; Li, Y. *Advances in Materials Science and Engineering* **2015**, 2015, 1-8.
89. Lu, C.-L.; Lin, H.-W.; Liu, C.-M.; Huang, Y.-S.; Lu, T.-L.; Liu, T.-C.; Hsiao, H.-Y.; Chen, C.; Kuo, J.-C.; Tu, K.-N. *NPG Asia Materials* **2014**, *6*, (10), e135-e135.
90. Chen, Y.; Yu, K. Y.; Liu, Y.; Shao, S.; Wang, H.; Kirk, M. A.; Wang, J.; Zhang, X. *Nature communications* **2015**, *6*, 7036.
91. Zhu, C.; Ning, W.; Li, H.; Zheng, T.; Xu, G.; Luo, L. *Microelectronics Reliability* **2014**, *54*, (4), 773-777.
92. Sekiguchi, A.; Koike, J.; Kamiya, S.; Saka, M.; Maruyama, K. *Applied Physics Letters* **2001**, *79*, (9), 1264-1266.
93. Koike, J.; Sekiguchi, A.; Wada, M.; Maruyama, K. *AIP Conference Proceedings* **2002**, *612*, (1), 169-176.
94. Nucci, J. A.; Keller, R. R.; Sanchez, J. E.; Shacham-Diamand, Y. *Applied Physics Letters* **1996**, *69*, (26), 4017-4019.
95. Keller, R. R.; Nucci, J. A.; Field, D. P. *Journal of Electronic Materials* **1997**, *26*, (9), 996-1001.
96. Sekiguchi, A.; Koike, J.; Maruyama, K. *Applied Physics Letters* **2003**, *83*, (10), 1962-1964.
97. Bodapati, B. R.; P, S. P.; Bhattacharjee, P. P.; G, S. *Materials Today Communications* **2018**, *16*, 320-329.
98. Pantano, M. F.; Espinosa, H. D.; Pagnotta, L. *Journal of Mechanical Science and Technology* **2012**, *26*, (2), 545-561.
99. Haque, M. A.; Saif, M. T. A. *Experimental Mechanics* **2002**, *42*, (1), 123-128.
100. Haque, M. A.; Saif, M. T. A. *Experimental Mechanics* **2003**, *43*, (3), 248-255.
101. Zhu, Y.; Moldovan, N.; Espinosa, H. D. *Applied Physics Letters* **2004**, *86*, (1), 013506.
102. Zhu, Y.; Corigliano, A.; Espinosa, H. D. *Journal of Micromechanics and Microengineering* **2006**, *16*, (2), 242.
103. Shan, Z. W.; Mishra, R. K.; Syed Asif, S. A.; Warren, O. L.; Minor, A. M. *Nat Mater* **2008**, *7*, (2), 115-9.
104. Gianola, D. S.; Sedlmayr, A.; Monig, R.; Volkert, C. A.; Major, R. C.; Cyrankowski, E.; Asif, S. A.; Warren, O. L.; Kraft, O. *Rev Sci Instrum* **2011**, *82*, (6), 063901.
105. Imrich, P. J.; Kirchlechner, C.; Kiener, D.; Dehm, G. *Scripta Materialia* **2015**, *100*, 94-97.

106. Uchic, M. D.; Dimiduk, D. M. *Materials Science and Engineering: A* **2005**, 400-401, 268-278.
107. Zhang, H.; Schuster, B. E.; Wei, Q.; Ramesh, K. T. *Scripta Materialia* **2006**, 54, (2), 181-186.
108. Greer, J. R.; Kim, J.-Y.; Burek, M. J. *JOM* **2009**, 61, (12), 19.
109. Hirouchi, T.; Shibutani, Y. *Materials Transactions* **2014**, 55, (1), 52-57.
110. Byer, C. M.; Li, B.; Cao, B.; Ramesh, K. T. *Scripta Materialia* **2010**, 62, (8), 536-539.
111. Maaß, R.; Uchic, M. D. *Acta Materialia* **2012**, 60, (3), 1027-1037.
112. Gu, X. W.; Loynachan, C. N.; Wu, Z.; Zhang, Y. W.; Srolovitz, D. J.; Greer, J. R. *Nano Lett* **2012**, 12, (12), 6385-92.
113. Fei, H.; Abraham, A.; Chawla, N.; Jiang, H. *Journal of Applied Mechanics* **2012**, 79, (6), 061011.
114. Zhang, X.; Wang, H.; Chen, X. H.; Lu, L.; Lu, K.; Hoagland, R. G.; Misra, A. *Applied Physics Letters* **2006**, 88, (17), 173116.
115. Dao, M.; Lu, L.; Shen, Y. F.; Suresh, S. *Acta Materialia* **2006**, 54, (20), 5421-5432.
116. Shen, Y. F.; Lu, L.; Lu, Q. H.; Jin, Z. H.; Lu, K. *Scripta Materialia* **2005**, 52, (10), 989-994.
117. You, Z. S.; Lu, L.; Lu, K. *Acta Materialia* **2011**, 59, (18), 6927-6937.
118. Projected size of the global market for 3D printing, materials & associated services in 2015 and 2025 (in billion U.S. dollars). <https://www.statista.com/statistics/315363/global-market-for-3d-printing-and-services/>
119. ASTM F3055-14a Standard Specification for Additive Manufacturing Nickel Alloy (UNS N07718) with Powder Bed Fusion. In ASTM International: West Conshohocken, PA, 2014.
120. Frazier, W. E. *Journal of Materials Engineering and Performance* **2014**, 23, (6), 1917-1928.
121. Walsh, F. C.; Ponce de Leon, C. *Transactions of the IMF* **2014**, 92, (2), 83-98.
122. Low, C. T. J.; Wills, R. G. A.; Walsh, F. C. *Surface and Coatings Technology* **2006**, 201, (1-2), 371-383.

## **BIOGRAPHICAL SKETCH**

Soheil Daryadel was born in 1989 in Tehran, Iran. He received his Bachelor of Science degree in Mechanical Engineering from the University of Guilan, Rasht, Iran in 2013, and his Master of Science degree in Mechanical Engineering from the University of Mississippi, University, MS, in 2015. Soheil started his doctoral study at The University of Texas at Dallas in fall 2015 under the supervision of Dr. Majid Minary. His research focuses on additive manufacturing and characterization of micro/nanoscale metallic nanostructures. Through his research, he has developed an innovative technique for fabrication of 3D metallic nanostructures with great control over the microstructure and material properties. He has authored and co-authored 16 peer reviewed journal publications. His research has been published in leading journals such as *Advanced Materials* and *Nano Letters*.

# CURRICULUM VITAE

## SOHEIL DARYADEL

<https://www.linkedin.com/in/soheildaryadel>

### EDUCATION:

**Ph.D. in Mechanical Engineering**, University of Texas at Dallas, Richardson, TX 2018  
Thesis: “Additive Manufacturing of Metallic Structures at Micro/Nanoscale”  
Advisor: Dr. Majid Minary

**Master of Science in Mechanical Engineering**, University of Mississippi, University, MS 2015  
Thesis: “Dynamic Response of Glass under Low-Velocity Impact and High Strain-Rate SHPB Compression Loading”

**Bachelor of Science in Mechanical Engineering**, University of Guilan, Rasht, Iran 2013  
Thesis: “Experimental and Numerical Investigations on Quail Eggshells Composite Structure”

### RESEARCH EXPERIENCE:

**Research Assistant in NanoBio Laboratory**, University of Texas at Dallas, Richardson, TX 2015-2018

- Designed and developed a metal 3D printing method termed as localized pulsed electrodeposition (L-PED) for the first time to fabricate micro-scale metallic structures with control over the microstructure and material properties
- Performed material characterization on the fabricated micro-scale structures (nanotwinned and nanocrystalline copper)
- Performed in-situ nanoindentation and micro-compression test in SEM on micro-scale structures
- Designed and developed a metal 3D printing process for flexible electronics and printed circuit boards (PCB)
- Characterized bio-inspired lamellar ceramic-polymer/metal composite, piezoelectric electrospun nanofibers
- Performed in-situ micro-fracture tests on the FIB-milled microscale bone samples

**Research Assistant in Blast and Impact Dynamics Laboratory**, U of Mississippi, University, MS 2013-2015

- Investigated dynamic response of different types of glass subjected to impact loading (Split Hopkinson Pressure Bar and Dynatup)
- Characterized composites enhanced with vertically aligned carbon nanotube, and pultruded hybrid glass/graphite epoxy composites for application in energy absorption under dynamic loading
- Utilized high-speed digital stereo imaging in dynamic deformation study

**Undergraduate Research Assistant in Biomimetic Engineering Group**, U of Guilan, Rasht, Iran 2011-2013

- Performed material characterization on biomaterials (egg shell and membrane)

### PUBLICATIONS:

16 peer-reviewed journal articles; 10 conference presentations (For more details visit [Google Scholar Profile](#)):

#### **Peer-reviewed Journals:**

- Soheil Daryadel, Ali Behroozfar, Seyedreza Morsali, Salvador Moreno, Mahmoud Baniasadi, Julia Bykova, Rodrigo A Bernal, Majid Minary-Jolandan, “Localized Pulsed Electrodeposition Process for Three-Dimensional Printing of Nanotwinned Metallic Nanostructures”, **Nano Letters**, 18 (1), pp 208-214, 2018. (IF: 12.7)
- Ali Behroozfar, Soheil Daryadel, Seyedreza Morsali, Salvador Moreno, Mahmoud Baniasadi, Rodrigo A Bernal, Majid Minary-Jolandan, “Microscale 3D Printing of Nanotwinned Copper”, **Advanced Materials**, Volume 30, Issue 4, 2018. (IF: 19.8)
- Malakooti, Sadeq, Rostami, Saman, Churu, Habel, Luo, Huiyang; Clark, Jenna; Casarez, Fabiola; Rettenmaier, Owen, Daryadel, Soheil, Minary, Majid, Sotiriou-Leventis, Chariklia, Leventis, Nicholas, Lu, Hongbing, “Scalable, Hydrophobic and Highly-Stretchable Poly(isocyanurate-urethane) Aerogels”, RSC Advances, issue 38, 2018.
- Zhe Xu, Jiacheng Huang, Cheng Zhang, Soheil Daryadel, Ali Behroozfar, Brandon McWilliams, Benjamin Boesl, Arvind Agarwal, Majid Minary-Jolandan, “Bioinspired Nacre-Like Ceramic with Nickel Inclusions Fabricated by Electroless Plating and Spark Plasma Sintering”, *Advanced Engineering Materials*, 20: 1700782, 2018.
- Mahmoud Baniasadi, Zhe Xu, Jizhe Cai, Soheil Daryadel, Manuel Quevedo-Lopez, Mohammad Naraghi, Majid Minary-Jolandan, “Correlation of annealing temperature, morphology, and electro-mechanical properties of electrospun piezoelectric nanofibers”, *Polymer*, Volume 127, Pages 192-202, , 2017.
- Seyedreza Morsali, Soheil Daryadel, Zhong Zhou, Ali Behroozfar, Mahmoud baniasadi , Salvador Moreno , Dong Qian , Majid Minary-Jolandan, “Multi-physics simulation of metal printing at micro/nanoscale using meniscus-confined electrodeposition: effect of nozzle speed”, *Journal of Applied Physics* 121, 21, 214305, 2017.
- Mahmoud Baniasadi, Zhe Xu, Salvador Moreno, Soheil Daryadel, Jizhe Cai, Mohammad Naraghi, Majid Minary-Jolandan, “Effect of thermomechanical post-processing on chain orientation and crystallinity of electrospun P (VDF-TrFE) nanofibers”, *Polymer*, Vol 118, Pages 223–235, 2017.
- Jiacheng Huang, Zhe Xu, Salvador Moreno, Seyedreza Morsali, Zhong Zhou, Soheil Daryadel, Mahmoud Baniasadi, Dong Qian, Majid Minary-Jolandan, “Lamellar Ceramic Semicrystalline-Polymer Composite Fabricated by Freeze Casting”, *Advanced Engineering Materials*, 1526-2648, 2017.
- Seyedreza Morsali, Soheil Daryadel, Zhong Zhou, Ali Behroozfar, Dong Qian, and Majid Minary-Jolandan, “Multi-physics simulation of metal printing at micro/nanoscale using meniscus-confined electrodeposition: Effect of environmental humidity”, *Journal of Applied Physics* 121, 024903, 2017.
- Seyed Soheil Daryadel, P Raju Mantena, Kiyun Kim, Damian Stoddard, AM Rajendran, “Dynamic response of glass under low-velocity impact and high strain-rate SHPB compression loading,” *Journal of Non-Crystalline Solids*, Volume 432, Part B, Pages 432–439, 2016.
- Kiyun Kim, P. Raju Mantena, Seyed Soheil Daryadel, Veera M. Boddu, Matthew W. Brenner, and Jignesh S. Patel, “Dynamic Mechanical Analysis and High Strain-Rate Energy Absorption Characteristics of Vertically Aligned Carbon Nanotube Reinforced Woven Fiber-Glass Composites,” *Journal of Nanomaterials*, vol. 2015, Article ID 480549, 7 pages, 2015.
- Afrough, M., Pandya, T., Daryadel, S., and Mantena, P. (2015) Dynamic Response of Pultruded Glass-Graphite/Epoxy Hybrid Composites Subjected to Transverse High Strain-Rate Compression Loading. *Materials Sciences and Applications*, 6, 953-962, 2015.
- Daryadel, S., Ray, C., Pandya, T. and Mantena, P. (2015) Energy Absorption of Pultruded Hybrid Glass/Graphite Epoxy Composites under High Strain-Rate SHPB Compression Loading. *Materials Sciences and Applications*, 6, 511-518, 2015.

#### **In preparation/Submitted:**

- Soheil Daryadel, Ali Behroozfar, Majid Minary-Jolandan, “A Microscale Additive Manufacturing Approach for In Situ Nanomechanics”, *Experimental Mechanics*, 2018, In revision.
- Soheil Daryadel, Ali Behroozfar, Majid Minary-Jolandan, “Toward Control of Microstructure in Microscale Additive Manufacturing of Copper Using Localized Electrodeposition”, *Advanced Engineering Materials*, 2018, In revision.
- Ali Behroozfar, Soheil Daryadel, Majid Minary-Jolandan, “Large Scale 3D Printing of Nickel for Flexible Electronics”, In preparation.

- Soheil Daryadel and Majid Minary-Jolandan, “Thermal Stability of Nanotwinned Copper in Interconnects Additively Manufactured by Localized Pulsed Electrodeposition”, In preparation.

**Conference Presentations (P) – Soheil Daryadel Presented:**

- (P) Soheil Daryadel, Ali Behroozfar, Rodrigo A Bernal, Majid Minary-Jolandan, “Additive Manufacturing of Metals at Micro/Nanoscale by Localized Pulsed Electrodeposition: Nanotwinned Copper Nanowires”, ASME MSEC2018, College station, Texas, June 2018.
- Ali Behroozfar, Soheil Daryadel, Seyedreza Morsali, Rodrigo A Bernal, Majid Minary-Jolandan, “PRINTING OF MICROSCALE NANOTWINNED COPPER INTERCONNECTIONS USING LOCALIZED PULSED ELECTRODEPOSITION (L-PED)”, ASME MSEC2018, College station, Texas, June 2018.
- Soheil Daryadel, Ali Behroozfar, Rodrigo A Bernal, Majid Minary-Jolandan, “Additive Manufacturing of Nanotwinned Copper by Localized Pulsed Electrodeposition”, SEM Annual Conference & Exposition on Experimental & Applied Mechanics, Greenville, South Carolina USA, June 2018. (accepted)
- (P) Soheil Daryadel, Ali Behroozfar, Rodrigo A Bernal, Majid Minary-Jolandan, “3D Printing of Nanotwinned Metallic Nanostructures by Localized Pulsed Electrodeposition”, MRS Spring 2018, Phoenix, Arizona USA, April 2018.
- Ali Behroozfar, Soheil Daryadel, Rodrigo A Bernal, Majid Minary-Jolandan, “Microscale Additive Manufacturing of Nanotwinned Copper Using Pulsed Localized Electrodeposition (P-LED)”, MRS Spring 2018, Phoenix, Arizona USA, April 2018.
- Soheil Daryadel, Majid Minary, Ali Behroozfar, Seyedreza Morsali, “Additive Manufacturing of Metals at Micro/Nanoscale by Localized Electrodeposition: Microstructure and Mechanical Properties”, SEM Annual Conference & Exposition on Experimental & Applied Mechanics, Indianapolis, Indiana USA, June 2017.
- Soheil Daryadel, Majid Minary, Ali Behroozfar, Seyedreza Morsali, “Additive Manufacturing of Metals at Micro/Nanoscale by Localized Electrodeposition: Microstructure and Mechanical Properties”, SEM Annual Conference & Exposition on Experimental & Applied Mechanics, Indianapolis, Indiana USA, June 2017.
- Amin Abbasalipour, Mohammad Mahdavi, Varun Kumar, Siavash Pourkamali, Soheil Daryadel, Majid Minary, “Nano-precision micromachined frequency output profilometer”, SENSORS, 2016 IEEE Conference, 1-3, 2016.
- (P) Soheil Daryadel, Damian Stoddard, Arunachalam Rajendran, “Dynamic response of glass under high-strain rate compression loading”, A.S.M.E Early Career Technical Conference, Birmingham, Alabama, November 2014.
- (P) S. Daryadel, H. Rajabi, A. Darvizeh, “Experimental and numerical investigations on quail eggshells composite structure”, The 3rd International Conference on Composites: Characterization, Fabrication and Application (CCFA-3), pp 99-101, Tehran-Iran, December 2012.

**TEACHING AND MENTORING EXPERIENCE:**

**Graduate Teaching Assistance**, University of Texas at Dallas, Richardson, TX 2015-2018

Graded homework assignments and quizzes. Lectured selected sessions. Held office hours and review sessions before exams.

- Mechanical Vibration (1 Semester) Under Supervision of: Dr. Park
- Mechanics of Material (1 semester) Under Supervision of: Dr. Baughn
- Intro to Nanostructured Materials (1 Semester) Under Supervision: Dr. Voit

**Graduate Teaching Assistance**, University of Mississippi, University, MS 2013-2015

Drafted and graded homework assignments and quizzes. Lead, supervised, and planned undergraduate laboratory classes. Held office hours and review sessions before exams.

- Structures and Dynamics Laboratory (2 Semesters) Under Supervision of: Dr. Mantena

- Kinematics: Analysis and Synthesis (1 Semester) Under Supervision of: Dr. Mantena
- Intro to Mechanical Engineering (2 Semesters) Under Supervision of: Dr. Rajendaran

**Graduate Teaching Assistance**, University of Guilan, Rasht, Iran 2011-2012

Graded homework assignments and quizzes. Responsible for preparing and leading weekly problem sessions (~40 students)

- Physic I (2 Semesters) Under Supervision of: Dr. Abdollahi

#### **Mentoring**

- Undergraduate student volunteers, University of Texas at Dallas 2015-2018
- High school students, NanoExplorers Program, NanoTech Institute, University of Texas at Dallas 2017-2018
- Advised an undergraduate honors college student for thesis preparation, University of Mississippi 2014-2015

#### **INDUSTRY EXPERIENCE:**

**Mechanical Engineer in Geo technical projects**, Baspar Pey Iranian Co., Tehran, Iran 2011-2013

- Role: Supervisor, responsible for the overall daily activities including: planning, collecting and analyzing data

#### **AWARDS AND FELLOWSHIPS:**

- NSF Student Travel Award for ASME MSEC2018, College Station, TX 2018
- PhD Research Small Grant, University of Texas at Dallas, Richardson, TX 2017
- STEM Graduate Research Assistant Scholarship, University of Texas at Dallas, Richardson, TX 2015-2018
- STEM Graduate Research Assistant Scholarship, University of Mississippi, University, MS 2013-2015
- Full scholarship, BSc in Mechanical Engineering at the University of Guilan, Rasht, Iran 2008-2013

#### **PROFESSIONAL ACTIVITIES AND LEADERSHIP:**

- Member of American Society of Mechanical Engineers (ASME), Society for Experimental Mechanics (SEM), Materials Research Society (MRS).
- Referee for the journals of MRS Communication, Strain, Part L: Journal of Materials: Design and Applications, Structural Engineering and Mechanics
- Session Co-Chair for the MSEC2018 conference, College Station, TX, 2018.
- Senator of Graduate School Council, University of Mississippi, University, MS, 2014-2015.

#### **TECHNICAL SKILLS AND SOFTWARE:**

- Microscale Metal Additive Manufacturing (3D Printing): >3 years of experience in research and development (R&D), and design of experiments (DOE)
- Nanomanipulation and testing of micro/nano-scale materials in-situ SEM and TEM: Preparation and mechanical and electrical characterization of samples
- Mechanical Characterization: ASTM-based tension, compression, bending, and shear tests, Nanoindentation, MTI microstage test, Split Hopkinson pressure bar (SHPB), Dynamic mechanical analysis (DMA)
- Microscopy and Metrology (>1000 Hr. of experience): Focused ion beam (FIB), Scanning electron microscope (SEM), Optical microscopy, Contact angle measurement (CAM), Profilometer
- Electronics: Four probe measurements in nanowires, Precision electrical measurements (e.g., source-meter, probe station)

- Thin film deposition: Electrodeposition, Electroless deposition, Electron-beam evaporator, Sputter deposition system
- Analytical chemistry techniques: X-ray diffraction (XRD), Energy Dispersive Spectroscopy (EDS), Fourier-transform infrared spectrometer (FTIR), Cyclic voltammetry (CV)
- Software: Computer aided design (CAD): Solidworks, Digital image correlation (DIC): GOM, ProAnalyst  
Motion Analysis Programming Languages: MATLAB, General: Microsoft Office (Word, PowerPoint, Excel), ImageJ, OriginLab